



Efficient low-frequency room acoustic modelling.

Mondet, Boris Jean-Francois

Publication date:
2020

Document Version
Publisher's PDF, also known as Version of record

[Link back to DTU Orbit](#)

Citation (APA):
Mondet, B. J-F. (2020). *Efficient low-frequency room acoustic modelling*. Technical University of Denmark.

General rights

Copyright and moral rights for the publications made accessible in the public portal are retained by the authors and/or other copyright owners and it is a condition of accessing publications that users recognise and abide by the legal requirements associated with these rights.

- Users may download and print one copy of any publication from the public portal for the purpose of private study or research.
- You may not further distribute the material or use it for any profit-making activity or commercial gain
- You may freely distribute the URL identifying the publication in the public portal

If you believe that this document breaches copyright please contact us providing details, and we will remove access to the work immediately and investigate your claim.

Efficient low-frequency room acoustic modelling

Boris Mondet
Doctor of Philosophy
2020

**Efficient low-frequency
room acoustic modelling**

Report written by:

Boris Mondet

Advisor(s):

Jonas Brunskog, Associate Professor at the Electrical Engineering Department of DTU
Cheol-Ho Jeong, Associate Professor at the Electrical Engineering Department of DTU
Claus Lynge Christensen, Managing Director at Odeon A/S

DTU Electrical Engineering

Technical University of Denmark
2800 Kgs. Lyngby
Denmark

elektro@elektro.dtu.dk

Project period: 15. December 2016- 14. February 2020

Education: Ph.D.

Field: Acoustic Technology

Class: Public

Remarks: This report is submitted as partial fulfillment of the requirements for graduation in the above education at the Technical University of Denmark. The project was funded by Innovationsfonden and Odeon A/S.

Copyrights: ©Boris Mondet, 2020

Abstract

Room acoustic simulations are widely used in the design and renovation of various spaces, ranging from offices to theatres or even churches. Nevertheless, small volumes remain a challenge with currently available techniques. These include spaces such as meeting rooms and classrooms, where acoustic conditions are critical. This limitation is due to two main factors. Firstly, surface materials are commonly characterized with simplified parameters which neglect valuable information for low frequencies. It thus leads to an approximate modelling of reflections that is not valid in small rooms. Secondly, research on room acoustic simulations has not been able to find a method that offers accurate results in a timely manner. Indeed, the methods available either favor efficiency by means of approximations or inversely are accurate at the expense of a large computational load. The present PhD thesis thus pursues accurate and efficient acoustic simulations in small rooms by tackling these two limiting factors.

The boundary conditions representing surfaces in a room are generally expressed in terms of absorption and scattering coefficients, two energy parameters lacking phase information. The latter is most often estimated from the roughness of a surface, while the former is the only parameter with widely available measured data for the materials found in room acoustics. On the contrary, surface impedance is a complex-valued parameter from which all the information needed to describe a boundary can be derived. Consequently, a method to calculate surface impedances from measured absorption coefficients is introduced in this study. The method is based on a novel impedance model making use of fractional calculus. The information missing in absorption coefficients is then retrieved by solving an inverse problem through constrained optimization.

The vast majority of commercial solutions for room acoustic simulations are based on geometrical acoustics. They therefore rely on high frequency assumptions that do not account accurately for interference and diffraction effects. On the other hand, the numerical methods for differential equations, often called wave-based methods in room acoustics, are too heavy computationally for practical application. A compromise method that combines accuracy and efficiency thus has to be found. To this end, the Equivalent Source Method in the time domain is investigated. This method draws its efficiency from assuming a solution to the wave equation and approximately solving the boundary condition equation. A combination of image and equivalent sources is then introduced in order to improve the accuracy of the method at a low computational cost.

Accurate acoustic simulations of small rooms are brought closer to practical reality thanks to the contributions of this project. The impedance retrieval method introduced

is a tool that can benefit all simulation methods, and hence improve the overall accuracy of room acoustic modelling. The study of the Equivalent Source Method also provides valuable insight on its application to room acoustics. Moreover, the combination of image and equivalent sources presented shows an interesting potential and could lead to further research on the topic.

Resumé

Rumakustiske simuleringer bliver ofte brugt i forbindelse med design og istandsættelse af forskellige rum. Anvendelsen af sådanne simuleringer kan findes i alt fra kontorer til teatre såvel som kirker. Men ikke desto mindre er simulering af små rum stadig en udfordring med de nuværende metoder, dette inkluderer møderum og klasselokaler hvor de akustiske betingelser er kritiske. To faktorer er hovedsageligt skyld i disse begrænsninger. For det første er overfladematerialer ofte karakteriseret med forsimplet parametre der negligerer værdifuld lavfrekvent information, hvilket kan føre til forkert modellering af refleksioner i små rum. For det andet har den nuværende forskning i akustiske simuleringer ikke ført til metoder der både er nøjagtige men også beregningslette. De tilgængelige beregningsmetoder er enten beregningslette men unøjagtige, eller nøjagtige og beregningstunge. Denne PhD afhandling vil derfor udforske muligheden for nøjagtige og beregningslette akustiske simuleringsmetoder der kan benyttes til beregning af små rum og samtidig håndtere disse to begrænsende faktorer.

Randbetingelserne der repræsenterer overfladerne i et rum er normalt beskrevet ved en absorptions- og spredningskoefficient, to energiparametre der ikke inkluderer faseinformation. Spredningskoefficienten er oftest estimeret på baggrund af grovheden af overfladen, hvorimod absorptionskoefficienten er den eneste materialeparameter i rumakustik der er almindeligt tilgængelig som målt data. På den anden side kan overflader beskrives fuldstændig ved hjælp af den komplekse overfladeimpedans. I dette studie vil derfor blive introduceret en metode til at beregne impedanser fra målte absorptionskoefficienter. Denne metode er baseret på en ny impedansmodel der benytter såkaldt fractional calculus. Den information som ikke er repræsenteret i absorptionskoefficienterne findes ved at løse et inverst problem ved brug af constrained optimization.

Størstedelen af de kommercielle løsningsmetoder der bliver anvendt til simulering af rumakustik, er baseret på geometriskakustik. Geometriskakustik er baseret på antagelsen af høje frekvenser, dette gør modellering af effekter som interferens og diffraktion unøjagtig. På den anden side, numeriske metoder der benytter partielle differentiaalligninger, ofte kaldet wave-based metoder i rumakustik, kan betragtes som alt for beregningstunge til praktisk brug. Det er derfor nødvendigt at finde en metode der er et kompromis mellem beregningseffektivitet og nøjagtighed. Som en mulighed undersøger dette projekt beregningsmetoden Equivalent Source metoden. Denne metode for sin beregningseffektivitet ved at antage en løsning til bølgeligningen og approksimerer randbetingelsesligningen. Derudover introduceres en kombination af billede- og ækvivalentkilder der forbedrer metodens nøjagtighed og beregningseffektivitet.

Takket være det videnskabelige bidrag i dette projekt bliver nøjagtige akustiske simuleringer af små rum bragt tættere på praktisk brug. Impedansmetoden, forslået i dette projekt, er et værktøj der kan være en hjælp i alle former for simuleringsmetoder og medvirke til generelt øget modelleringsnøjagtighed af rumakustik. Det her i præsenterede studie af Equivalent Source metoden bibrager med værdifuld indsigt i hvordan metoden kan benyttes i forbindelse med rumakustik. Derudover bliver det vist at kombinationen af billede- og ækvivalentkilder har et interessant potentiale der kan føre til fremtidig forskning i netop dette emne.

Acknowledgements

I would like to thank Jonas Brunskog for his role as main supervisor in this project. His insight and guidance have been highly helpful to face the challenges and other dead ends encountered during the course of this research.

Gratitude also goes to Cheol-Ho Jeong, Claus Lynge Christensen and Jens Holger Rindel for following closely on the project and giving valuable feedback.

During the project I had the chance to visit NTNU in Trondheim as a guest PhD. I want to thank Peter Svensson for his warm welcome in a cold land, our regular discussions have been a great source of progress for the work to be carried out.

As an industrial PhD, my time at the workplace was shared between the company office and the university department. I am grateful to my co-workers in Odeon A/S, who showed their interest and provided a different perspective on the study. Thanks also to my colleagues in the Acoustic Technology group in DTU for their scientific help and the occasional discussions on the inherent struggles of life as a PhD student.

Finally, I would like to thank my family and friends for their continuous and ultimate support over the years.

Contents

Abstract	i
Resumé	iii
Acknowledgements	v
Contents	vii
1 Introduction	1
1.1 Motivation	1
1.2 Background	1
1.3 Scope of the thesis	3
1.4 Structure	3
2 Boundary conditions	5
2.1 Characterization of boundaries	5
2.2 Modelling of boundary conditions	6
3 Simulation methods	11
3.1 Geometrical acoustics	11
3.2 Numerical methods for differential equations	17
3.3 The Equivalent Source Method	24
4 Discussion	33
5 Conclusion	35
Bibliography	37
Appendices	43
A Retrieving complex surface impedances from statistical absorption coefficients	45
B From absorption to impedance: Enhancing boundary conditions in room acoustic conditions	57

C Parametric study of the Equivalent Source Method and interior domain calculations	71
D A combination of image and equivalent sources: Developments on "Parametric study of the Equivalent Source Method and interior domain calculations"	95

List of Figures

2.1	Contour maps of α_s in equation (2.5) at 2000 Hz for a sample of 11 m ² , from paper B.	8
2.2	Original impedance from theoretical model and retrieved impedance in 1/3-octave bands, from paper B. Solid blue line: original resistance; Dashed blue line: original reactance; Dash-dotted red line: retrieved resistance; Dotted red line: retrieved reactance.	9
3.1	Diffuse reflection as per Lambert's law.	12
3.2	Geometry of the acoustical radiosity. Black dot: sound source; Orange dot: receiver point.	12
3.3	Example of ray-tracing up to the second reflection order, from [48].	14
3.4	Example of beam reflections.	15
3.5	Image source positions for a rectangular room. Black disc: original source; Blue triangles: 1 st order image sources; Orange diamonds: 2 nd order image sources; Green crosses: 3 rd order image sources.	16
3.6	Staggered grids for the Finite Difference in the Time Domain, with space on the horizontal axis and time on the vertical axis. Red discs: sound pressure nodes; Blue diamonds: particle velocity nodes.	18
3.7	Local shape functions in the Finite Element Method.	19
3.8	Positions of equivalent sources (red crosses) in a 2D room model.	25
3.9	Close-up front view of the discretization of a surface, from paper D. Blue dots: control points; Red crosses: equivalent sources.	27
3.10	Close-up illustration of the discretization of a surface in the Equivalent Source Method, from paper C. Blue dots: control points; Red crosses: equivalent sources.	28
3.11	Sound pressure at a receiver point in front of a finite plate for $h_p = 143$ mm and $\kappa = 4$, from paper C. Solid blue line: reference sound pressure; Dotted red line: ESM with $d/L = 0.022$; Dash-dotted yellow line: ESM with $d/L = 0.066$	29
3.12	Sound pressure at a receiver point in a rectangular box for $h_p = 143$ mm, $\kappa = 4$ and $d/L = 0.094$, from paper C. Solid blue line: reference sound pressure; Dotted red line: Equivalent Source Method.	30

CHAPTER 1

Introduction

1.1 Motivation

Room acoustics consists of the study and prediction of sound fields in closed spaces. The aim is to predict how sound will be experienced by the users of a room. This is done by simulating the room impulse response, from which auralization and acoustic parameters can be derived. Auralization consists in convoluting an anechoic recording, e.g. music or speech, with the impulse response of a room [57]. The signal created renders how that sound would be heard in that room. Acoustic parameters also give important insight on the properties of a room. The most common one is the reverberation time, which describes how fast sound is attenuated in a room. The intelligibility of speech for listeners can also be assessed with the speech transmission index, or the perception of music with the clarity index [28]. Many other acoustic parameters exist, most of which can be derived from the impulse response. It is therefore central to determine how sound propagates in a room in the time domain.

The spaces investigated in room acoustics can range from small rooms such as car cabins or offices to the large volumes of concert halls and the like. It is therefore a wide range in terms of dimensions. The present work is concerned with small to moderately sized rooms, such as classrooms and offices where clear transmission of speech is essential. Acoustic conditions can have a significant impact on students' and workers' performances [2]. Noisy environment have an adverse effect on cognitive tasks, especially reading, focusing, problem solving and memorizing [52, 36]. On the contrary, quiet environments where speech is easily understandable foster learning and working efficiency. Being able to design and predict the acoustics of small to moderately sized rooms would therefore be highly beneficial to children and office workers, two groups of people who spend most of their everyday lives in such spaces.

1.2 Background

The propagation of sound in time domain in any space is described by the wave equation [19]

$$\nabla^2 p - \frac{1}{c^2} \frac{\partial^2 p}{\partial t^2} = 0, \quad (1.1)$$

where $p(t)$ is the sound pressure and c is the speed of sound in air. It is derived from three linearized fundamental equations: the conservation of momentum, the conservation of mass, and adiabatic compression. The Green's function $g(t)$ is the solution to the inhomogeneous wave equation [11]

$$\nabla^2 g - \frac{1}{c^2} \frac{\partial^2 g}{\partial t^2} = -\delta(\mathbf{r}_0)\delta(t), \quad (1.2)$$

with δ the Dirac delta function and \mathbf{r}_0 the position of a point source. Like any differential equation, the wave equation comes with its associated boundary conditions. In an unlimited domain, the Sommerfeld radiation condition must be respected. Noting r the distance between a point in space and the point source, it leads to the free-field Green's function in the time domain

$$g(t) = \frac{\delta(t - r/c)}{4\pi r}. \quad (1.3)$$

In room acoustics the boundary conditions are prescribed by the shapes and materials of the different surfaces, making it impossible to find an analytical Green's function.

Interferences between incident and reflected waves can have an important influence when sound propagates in an enclosure [12]. When wavelengths are larger or of same order as the room dimensions, modes appear at the natural frequencies of the room and lead to strong responses. Moreover, when wavelengths are of same order as the dimensions of surfaces in the room, diffraction from edges can be observed. These wavelengths define the low frequency range in room acoustics. As wavelengths decrease with increasing frequency, the reflected waves become incoherent and interferences become random. As a result, individual modes have less influence due to high modal overlap and edge diffraction effects vanish in the sound field.

Since the wave equation with its associated boundary conditions cannot be solved analytically in room acoustics, numerical simulations are performed to calculate the impulse responses of rooms. Simulation methods can be separated into two categories: geometrical acoustics and numerical methods for differential equations, also called wave-based methods in the field of room acoustics. Techniques belonging to geometrical acoustics are traditionally employed [51]. They make use of high-frequency assumptions, such as propagation of sound in straight lines and specular reflections, in order to simplify calculations and reduce computation time. Although energy-based simulations are more common, geometrical acoustics can include phase information to account for interferences. Nevertheless, diffraction effects remain challenging to model. Numerical methods for differential equations work by discretizing the equation under study in the domain considered or on its boundary [50]. In room acoustics, it can either be the wave equation that is discretized in the volume of the room or the boundary condition equation that is treated on the different surfaces. These numerical methods can account for all wave phenomena as they do not assume a certain behaviour of the sound field, but they generally come with a large computational load that prohibits their practical use in room acoustics. Whatever method is employed, determining the individual modes resulting from interferences require a fine frequency resolution. In frequency-domain

calculations, simulations can only be performed one frequency at a time. It would thus imply a large number of simulations to obtain an accurate room impulse response. On the contrary, time-domain simulations are able to provide results for a chosen predefined frequency range at once. Consequently, only time-domain simulation methods are viable options in terms of computation efficiency for low-frequency room acoustics.

1.3 Scope of the thesis

No matter the method employed, an acoustic simulation is always made of three elements: a geometrical model defining the domain, a set of boundary conditions, and a calculation algorithm. In order to obtain correct results, all three elements need to be suited to the problem studied. Geometrical models can be created to any level of details needed with the help of a CAD program. Thus, they are usually not a source of significant error and will not be discussed in the present work.

All the information needed to characterize boundaries in common simulation methods is comprised in the surface impedance. The specific parameter needed to express the boundary conditions for any algorithm can then be derived from this quantity. However, surface impedance data is not available for common building materials. Instead, the absorption coefficient is measured according to ISO 354 [18]. This parameter unfortunately leaves out phase and angle-dependence information. Phased simulations then have to resort to rough approximations and estimates as boundary conditions, leading to inaccurate results. Thus, the first objective of the present work is to design a method to determine surface impedances from measured absorption coefficients, hence allowing to generate any boundary condition parameter a simulation algorithm could need.

Current simulation methods in room acoustics are not suited for small volumes. Techniques from geometrical acoustics lack accuracy to model interference and diffraction effects, while traditional numerical methods for differential equations are too heavy computationally for practical applications. Therefore, the second objective of this project consists in finding a method that exhibits both computation efficiency and accuracy at low frequencies. To do so, the Equivalent Source Method in the time domain is investigated. This method was originally designed for radiation and scattering problems, with notable efficiency arguments. Its potential application to room acoustics is thus studied, as well as its combination with image sources in order to improve its accuracy.

1.4 Structure

The articles published or to be submitted for publication are showcased in the appendix to provide the research conducted over the course of the project. The thesis is then organised so as to introduce fundamental concepts, explain background theory, and present the main findings of the articles. Chapter 2 touches upon the representation of boundary conditions in room acoustics, with current practices and the impedance retrieval method

proposed as a solution. Chapter 3 treats the different simulation methods encountered in acoustics. It includes further investigation on the Equivalent Source Method in the time domain and its combination with image sources.

CHAPTER 2

Boundary conditions

Boundary conditions in room acoustics are widely described in the frequency domain, and are then transformed to the time domain when necessary. The present study on boundary conditions has thus been carried out in the frequency domain accordingly.

2.1 Characterization of boundaries

The wave equation in the frequency domain is called the Helmholtz equation [19]. In room acoustics, it is associated with the Robin boundary condition [8]

$$\mathcal{Z}u = p, \quad (2.1)$$

where \mathcal{Z} is the wall impedance operator, u is the particle velocity, and p is the sound pressure. This equation describes the excitation of the boundary induced by the pressure field. If the sound field at the boundary is considered to be composed of an incoming plane wave, the boundary condition is reduced to the algebraic expression

$$Z_a = \frac{p}{u_n}, \quad (2.2)$$

with $Z_a \in \mathbb{C}$ the surface impedance and u_n the particle velocity in the normal direction to the boundary. This form is generally used in room acoustics rather than the impedance operator. The value of Z_a depends on the material constituting the boundary, the position on the surface, and the incidence angle θ of the incoming plane wave. A common approximation is to assume a locally reacting surface, meaning that the excitation at one point of the boundary is independent of sound pressure at neighbouring points. This simplification makes Z_a constant over the whole surface and removes its angle-dependency. Nevertheless, building materials are rarely locally reacting and this approximation sacrifices accuracy. In the time domain, Eq. (2.2) is equivalent to

$$u_n(t) = p(t) * y_a(t), \quad (2.3)$$

where the surface admittance $y_a(t)$ is the inverse of the surface impedance.

In practice, the sound field in front of a boundary is more complex than a single incoming plane wave. The absorption coefficient α is then defined as the ratio between the power absorbed by a surface Π_{abs} and the incident power on said surface Π_{inc}

$$\alpha = \frac{\Pi_{abs}}{\Pi_{inc}}. \quad (2.4)$$

As it is an energy parameter, $\alpha \in \mathbb{R}$, it does not include any phase information. The absorption coefficient depends on the incident power and can thus take different forms according to the incident sound field. It is commonly measured in reverberation chambers according to ISO 354 [18], resulting in the Sabine absorption coefficient. In such a case, the sound field can be decomposed as a sum of incoming plane waves, and the corresponding statistical absorption coefficient is defined as [54, 55]

$$\alpha_s = 8 \int_0^{\pi/2} \frac{\operatorname{Re}\{Z_a(\theta)\} \sin \theta}{|Z_a(\theta) + Z_r(\theta)|^2} d\theta, \quad (2.5)$$

where $Z_r \in \mathbb{C}$ is the radiation impedance. This quantity is equal to the ratio between the radiated sound pressure and the transverse velocity of the surface [22]. Z_r depends on the shape and size of the surface as well as the incidence angle θ , and it is averaged over the positions on the surface and over radiation angles. Given a rectangular surface with a known area, the value of $Z_r(\theta)$ can be estimated for all frequencies [10].

2.2 Modelling of boundary conditions

2.2.1 Current practices

Historically, and still to this day, unphased geometrical acoustics has been the favored option for room acoustic simulations. These algorithms require absorption and scattering coefficients as boundary conditions to perform the calculations. In parallel, international standards [16, 17, 18] have been set for the measurement of surface impedance at normal incidence and absorption coefficient at both normal and diffuse incidences. In practice, and despite important reproducibility issues [56], only the absorption coefficient at diffuse incidence is widely available for building materials. This measurement data is thus combined with an estimate of the scattering coefficient to perform unphased geometrical acoustics simulations. Accuracy could be improved in this case by using an angle-dependent absorption coefficient rather than applying the diffuse incidence coefficient for all angles.

Phased simulations, either by geometrical acoustics or numerical schemes, cannot be performed with the absorption coefficient to describe boundary conditions. The solution currently in use to model boundaries in these simulations is to estimate surface impedances or pressure reflection coefficients based on absorption data. However, the estimates often lack precision by being real-valued or frequency-independent. The results obtained from simulations using such boundary conditions are therefore unreliable. Accurate boundary parameters would then enable the practical use of phased simulations.

2.2.2 Proposed solution

A robust method to inversely determine the surface impedance from measured absorption coefficients of room acoustic materials is introduced. The detailed theory and validation

can be found in paper B, as well as a preliminary study in paper A.

The description of boundaries in room acoustic simulations must respect physical feasibility. Firstly, a boundary must be a passive system, it does not provide energy to the sound field. Secondly, a boundary must be a causal system, meaning that causes should always precede the consequences they produce. Lastly, time-domain signals must be real-valued; this applies to sound pressure and particle velocity but also to surface impedance and other boundary parameters. These three requirements can be written as the following mathematical expressions involving the surface impedance in the frequency domain [46]

$$\operatorname{Re} \{Z_a(\omega)\} \geq 0 \text{ for all } \omega \in \mathbb{R}, \quad (2.6)$$

$$Z_a(\omega) \text{ analytic for } \operatorname{Im}\{\omega\} < 0, \quad (2.7)$$

$$Z_a^*(\omega) = Z_a(-\omega). \quad (2.8)$$

The complex angular frequency ω in the equations is due to the mathematical transformation leading to these expressions. In order to guarantee that these requirements are respected, a general impedance model called RMK+1 and based on fractional calculus is introduced

$$Z_a(\omega) = K \cdot (j\omega)^{-1} + R + M \cdot (j\omega)^1 + G \cdot (j\omega)^\gamma, \quad (2.9)$$

with $R, M, K, G \geq 0$ and $-1 \leq \gamma \leq 1$. The first three terms correspond to a classic damped oscillator model, sometimes called RMK model, while the fourth term corresponds to a fractional integral or derivative depending on the sign of γ [9]. The values of the parameters in the RMK+1 model can then be determined from absorption coefficient data to fit the different types of materials found in room acoustics.

Surface impedances and statistical absorption coefficients are related with Eq. (2.5). However, the inverse problem to convert absorption coefficients into surface impedances is ill-posed. There is indeed an infinite number of complex surface impedances that correspond to a given real-valued absorption coefficient, as seen in Fig. 2.1. The parameters of the RMK+1 model are thus determined by solving a constrained optimization problem. The input data α_{in} is the measured Sabine absorption coefficient in octave bands, and the cost function F at an evaluation point Z_a is defined from the statistical absorption coefficient $\alpha_s(Z_a)$

$$F(Z_a) = \| \alpha_{in} - \alpha_s(Z_a) \|_2^2. \quad (2.10)$$

The optimization problem is solved with a gradient-based method returning the first local minimum found. Validity conditions based on the value of the cost function have therefore been implemented to verify that the minimum found is an appropriate solution. In addition, prior information about the type of material under study is used to constrain the problem and guide the solver towards physically meaningful solutions. The distinction between hard and soft materials is notably made [47], leading to the constraints

$$\text{Hard materials: } \operatorname{Re} \{Z_a(\omega)\} > 1 \text{ for all } \omega \in \mathbb{R}, \quad (2.11)$$

$$\text{Soft materials: } \operatorname{Re} \{Z_a(\omega)\} < 2 \text{ for all } \omega \in \mathbb{R}, \quad (2.12)$$

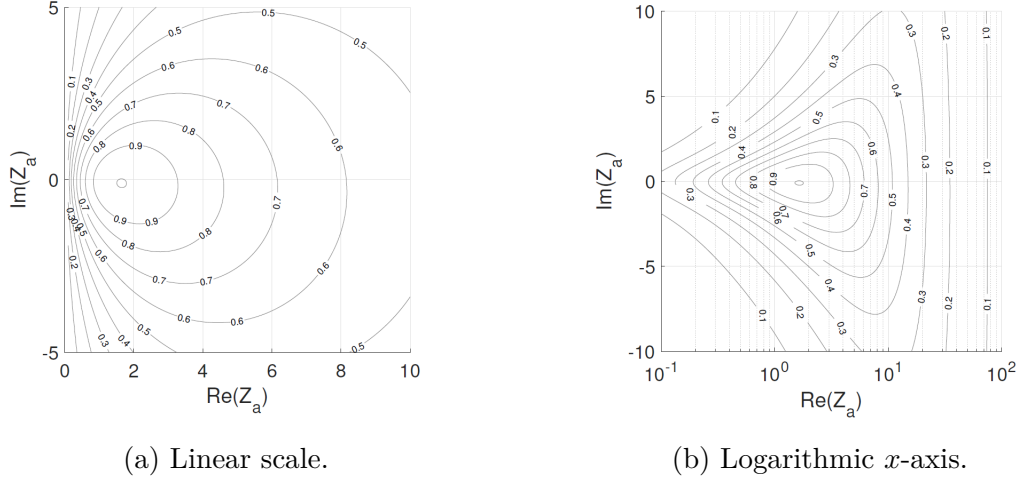


Figure 2.1: Contour maps of α_s in equation (2.5) at 2000 Hz for a sample of 11 m², from paper B.

Additional specific constraints have been established for porous materials and membrane absorbers based on their theoretical surface impedance models. The detailed validity conditions and specific constraints can be found in paper B.

The RMK+1 model and the retrieval method with constrained optimization have first been tested on input data created from theoretical impedance models of room acoustic materials. The materials investigated were a soft and a hard porous absorber with rigid backing, a porous absorber backed by an air cavity, a membrane absorber, a perforated panel, and a microperforated panel. The theoretical models were used to create original surface impedances and their corresponding statistical absorption coefficients, from which the surface impedances were retrieved. The match between original and retrieved impedances is shown in Fig. 2.2 for the porous absorber with cavity and the membrane absorber. Apart from the microperforated panel case, a good to excellent agreement was found between original and retrieved impedances. Only a few discrepancies appeared, as seen in Fig. 2.2a, due to the general form of the RMK+1 model. A single model indeed cannot represent in details all materials, but the agreements obtained from the use of the RMK+1 model coupled with the retrieval method are satisfactory.

The robustness of the method proposed has also been investigated. For each of the theoretical material case, the optimization problem has been solved repeatedly with random starting points. It was found that all the iterations lead to the same solution to the problem. This is an indication that the constraints applied to the optimization effectively narrow down the space of variables. Besides, the retrieval method has been applied to measurement data from different laboratories of the same four absorber samples [56]. The samples included two porous materials, one membrane absorber, and one hybrid combination of porous and membrane absorbers. The comparison of the deviations within measured and retrieved absorption coefficients showed that the retrieval

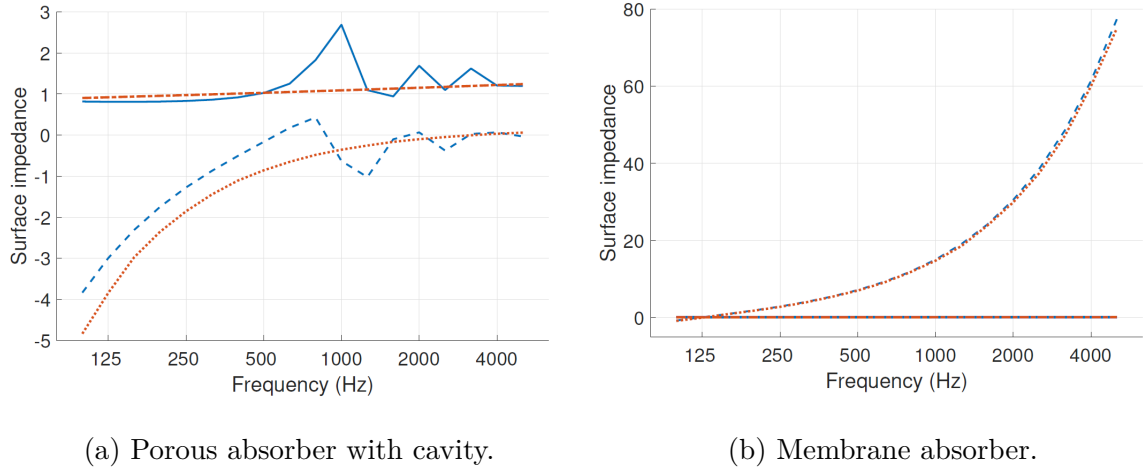


Figure 2.2: Original impedance from theoretical model and retrieved impedance in 1/3-octave bands, from paper B. Solid blue line: original resistance; Dashed blue line: original reactance; Dash-dotted red line: retrieved resistance; Dotted red line: retrieved reactance.

method does not amplify noise and deviations that can be found in measurement data, nor does it introduce any. The retrieval method presented can therefore be considered robust in terms of stability of the solution and in terms of sensitivity to input deviations.

The surface impedances obtained with this retrieval method can be directly used in simulation methods with impedance boundary conditions. Unphased simulation methods can also benefit from impedance retrieval, as angle-dependent absorption and reflection coefficients can be derived. Moreover, the RMK+1 model chosen in this method allows to describe surface impedances with continuous frequency. As a result, the transformation from frequency to time domain is facilitated and can be performed either by inverse Fourier transform or by Z-transform to create an IIR filter [20].

CHAPTER 3

Simulation methods

With suitable tools to create geometrical models and an appropriate method to describe boundary properties, the only element missing to obtain a good room acoustic simulation is the calculation algorithm. This chapter reviews the different simulations methods in acoustics with the perspective of their applicability to small and moderately sized rooms based on their literature. Each method is presented with the main elements of its theory and a brief discussion of its strengths and limitations. The Equivalent Source Method is further studied to investigate its potential application to interior problems and room acoustics. Implementation guidelines are thus determined and solutions to its flaws are suggested.

3.1 Geometrical acoustics

3.1.1 Acoustical radiosity

Unlike other geometrical acoustics methods, acoustical radiosity is based on the assumption that all reflections are diffuse [29, 40], i.e. sound is emitted in all directions at every reflection. The reflected sound intensity I as a function of the reflection angle ϕ then follows Lambert's law

$$I(\phi) = I(0) \cos \phi. \quad (3.1)$$

$I(0)$ is determined from the incident sound intensity and the absorption coefficient of the reflecting surface. An illustration of Lambert's law is shown in Fig. 3.1, where the sound intensity reflected in one direction corresponds to the distance from the reflection point to the intersection point with the circle at the corresponding angle. The relation in Eq. (3.1) implies that the incidence angle has no influence on the reflection angle. Moreover, the use of the absorption coefficient eliminates phase information from the simulation. Because every point on the boundary reflects sound in all directions, the energy emitted by one boundary element dS depends on the energy received from all the other elements dS' . The geometry is shown in Fig. 3.2. The positions of elements dS and dS' are respectively noted r and r' . The irradiation density $B(r, t)$ can then be defined as the sound intensity per unit area received on the boundary. It follows that the sound intensity $dI'(\theta', t)$ reflected from dS' towards dS is

$$dI'(\theta', t) = (1 - \alpha(r'))B(r', t) \cos \theta' dS', \quad (3.2)$$

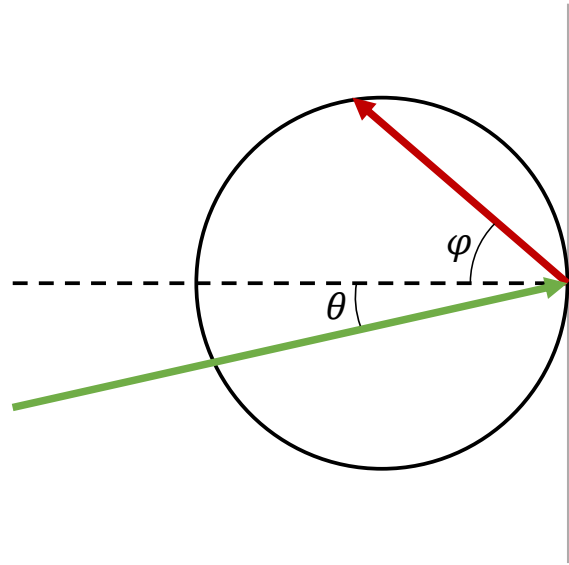


Figure 3.1: Diffuse reflection as per Lambert's law.

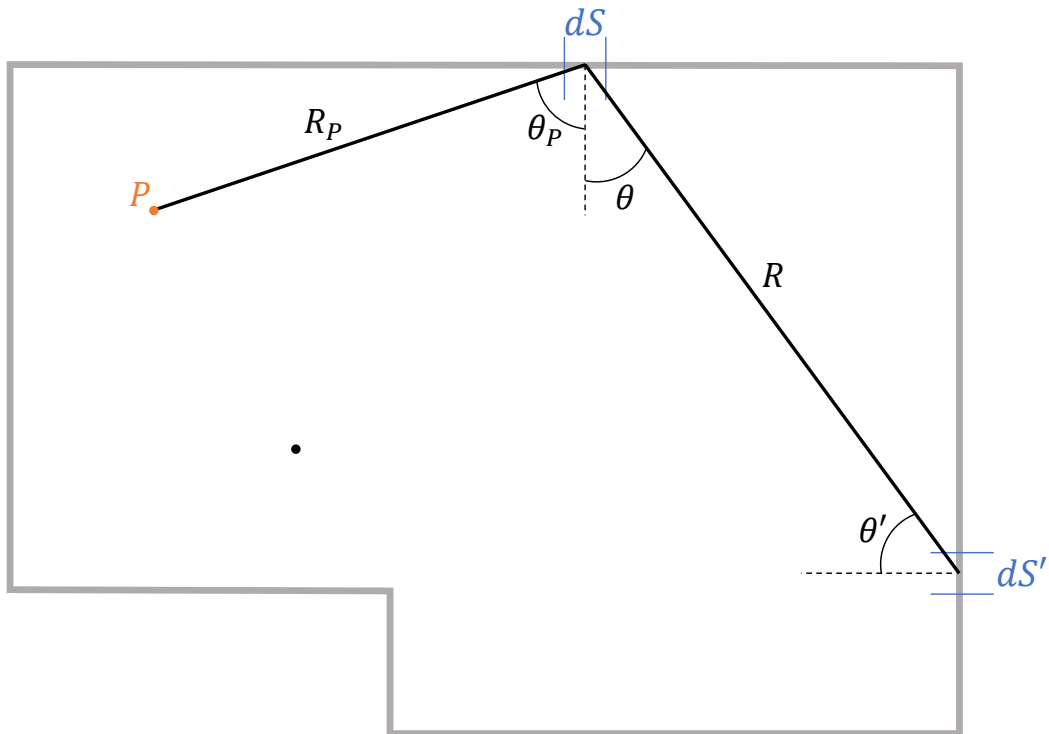


Figure 3.2: Geometry of the acoustical radiosity. Black dot: sound source; Orange dot: receiver point.

with α the absorption coefficient of the surface approximated to be independent of time and incidence angle. The total irradiation density on the element dS due to all the

other elements on the boundary and the source in the room is calculated with the integral equation

$$B(r, t) = \int_S (1 - \alpha(r')) B(r', t - R'/c) \frac{\cos \theta \cos \theta'}{\pi R^2} dS' + B_d(r, t), \quad (3.3)$$

where $B_d(r, t)$ is the direct contribution from the source. Once the equation is solved and the irradiation density is known for all elements at all times, the energy density $w(r_P, t)$ at a receiver P located at r_P can be determined from

$$w(r_P, t) = \int_S (1 - \alpha(r)) B(r, t - R_P/c) \frac{\cos \theta_P}{\pi c R_P^2} dS + w_d(r_P, t), \quad (3.4)$$

with $w_d(r_P, t)$ the contribution from the source in the room.

The assumption of completely diffuse reflections is valid for high frequencies and late reflections [14]. However, early specular reflections are highly important for the perception of sound in a room. The acoustical radiosity is therefore not a suitable method by itself to simulate room acoustics. Nevertheless, this assumption is an interesting feature for hybrid methods where the acoustical radiosity can be used to complement a method assuming purely specular reflections.

3.1.2 Ray-tracing

The ray-tracing technique was adapted from optics as a mean to investigate the impulse response of rooms [24]. In this method, sound is considered to propagate as straight rays emanating from a chosen source. The rays are distributed over the solid angle while making sure that their number is large enough to be representative. They are then propagated and reflected by the different surfaces. Scattering can be taken into account in different ways. For example, the new direction of propagation after a reflection can be determined by a linear combination of the specular direction vector and a random direction vector [48]. This random direction is found by considering Lambert's law in Eq. (3.1) as a probability distribution where the angle ϕ is measured from the specular direction. The coefficients of the linear combination are then based on the scattering coefficient of the surface. Each ray carries a certain amount of energy according to the source power and directivity. The history of each ray is tracked by storing its reflection points on the different surfaces. Every time a ray hits a surface, its energy is decreased by using the absorption coefficient of said surface. A ray is terminated either when it reaches a certain reflection order or when its energy drops below a defined threshold, depending on how the algorithm is built. When defining a receiver point, a volumetric detector is created to work around the infinitely small probability of a ray hitting a point [27]. An illustration of ray-tracing up to the second reflection order taken from [48] is given in Fig. 3.3. Each ray passing through the detector can give information about its arrival time, energy and incidence direction. If the source is considered to emit a pulse signal, summing information from all the rays detected at the receiver position

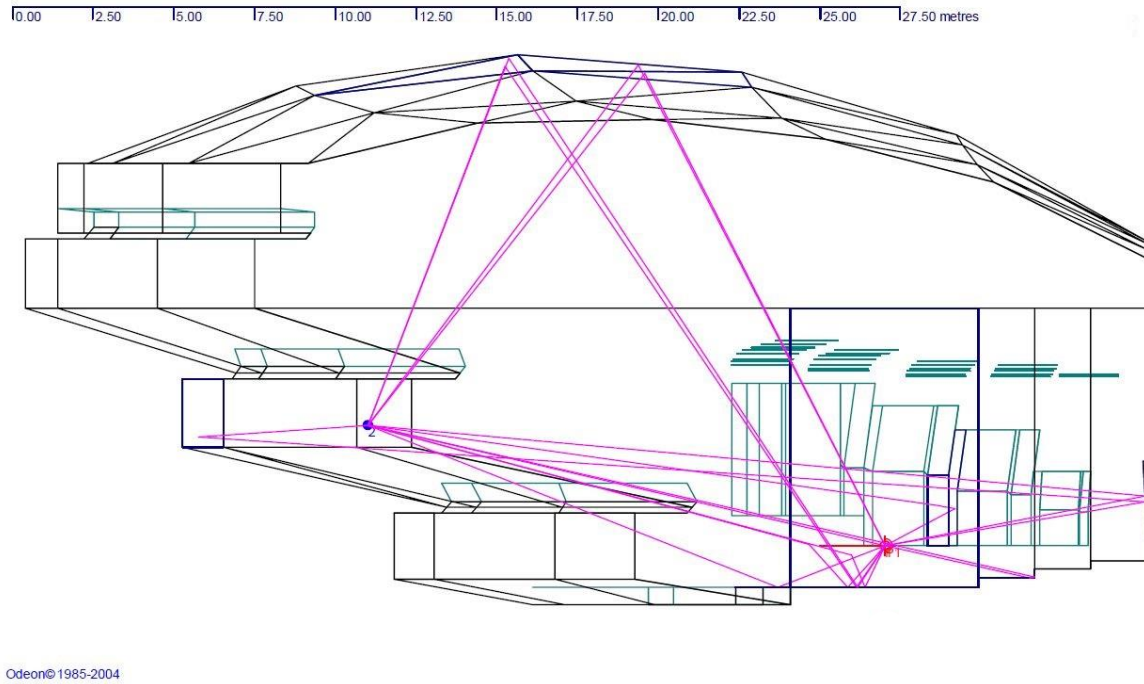


Figure 3.3: Example of ray-tracing up to the second reflection order, from [48].

results in an echogram from which the impulse response and different room acoustic parameters can be derived. The classical implementations of ray-tracing perform energy-based calculations. Nevertheless, it is possible to carry out phased simulations by using the pressure reflection coefficient instead of the absorption coefficient [51].

The main drawback of the ray-tracing technique is also its advantage and core assumption: the propagation of sound as rays. This assumption is only valid at high frequencies and discards effects due to the finiteness of the surfaces. Diffraction, which occurs when wavelengths are of same dimensions as surfaces for example, can only be tackled by complementing ray-tracing with an approximate dedicated algorithm [49]. Another issue that arises with ray-tracing is the number of rays needed to obtain accurate results. It needs to be high enough in order to be representative of all the possible travel paths in the room, but a precise estimate of the sufficient number cannot be easily calculated.

3.1.3 Beam-tracing

The beam-tracing method is a modification of the ray-tracing technique where three-dimensional beams are emitted by the source instead of rays [34]. Each beam is constituted of a central axis and bounding rays defining its cross-section, all of which emanating from the source. Consequently, the bounding rays are divergent and the area of the cross-section grows as the beam travels more distance. Triangular cross-sections are the most common geometry because they allow to discretize a sphere around the source

with fair accuracy. Reflection is considered to be only specular in this method and can be either phased or handled in energy terms [58]. When it occurs that the cross-section of a beam extends beyond the reflection surface, the beam is split and each part is then propagated separately as illustrated in Fig. 3.4. Since the beams are themselves volumetric objects, the receiver positions can simply be represented as points.

The advantage of the beam-tracing method lies in the number of beams needed for a simulation. The volumetric character of a beam indeed allows to cover more reflection paths at once than a single ray. However, scattering cannot be accounted for and splitting beams in the case of reflections over multiple surfaces is a tedious process. For these reasons, the beam-tracing method is far less widespread than the ray-tracing technique.

3.1.4 The Image Source Method

The Image Source Method is based on geometrically determining the image positions of the source in the room by use of symmetry relative to the boundaries [38]. This process is done recursively to obtain higher order image sources, as illustrated in Fig. 3.5 for a rectangular room. Each image source represents one reflection path and its order corresponds to the reflection order of the path, with the underlying assumption that all reflections are specular. The positions of the image sources account for the propagation distance between the original source and the last reflection point of the path. The

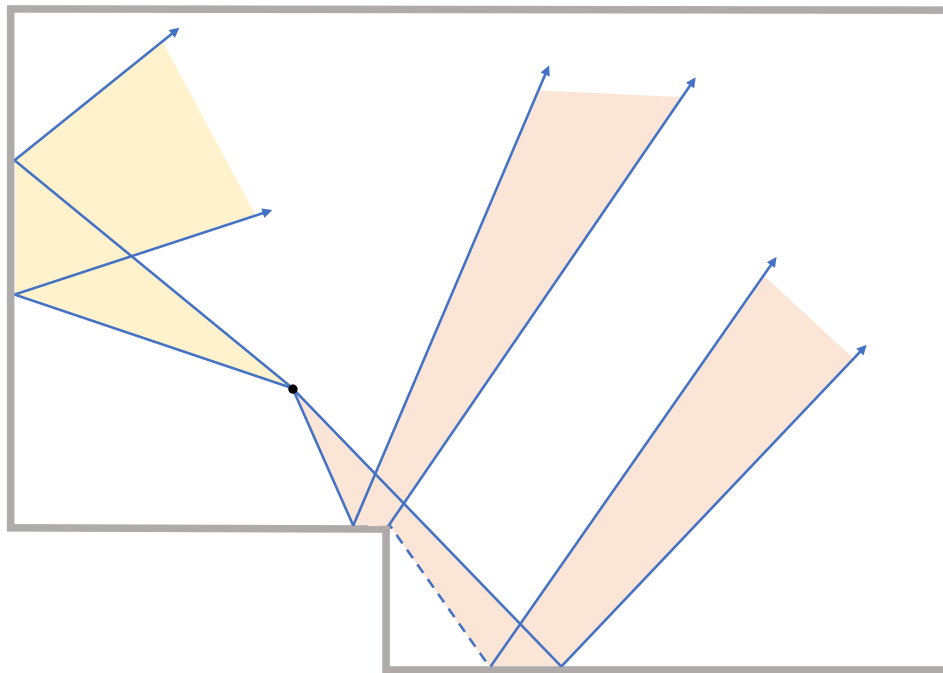


Figure 3.4: Example of beam reflections.

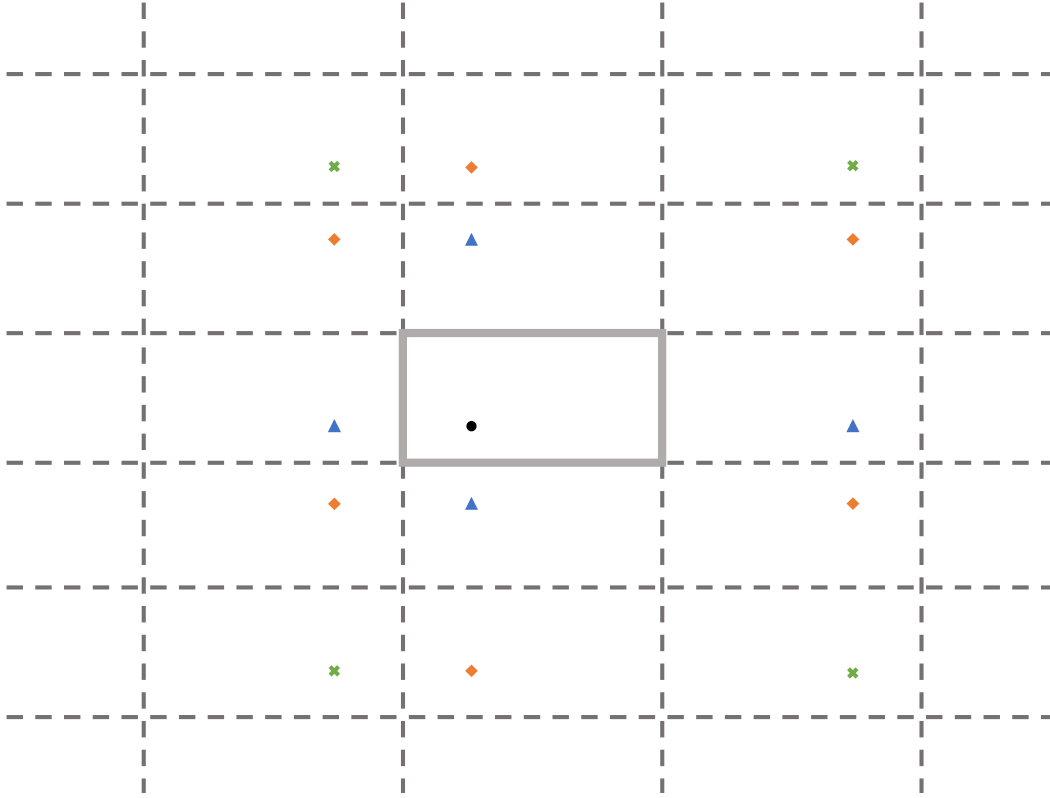


Figure 3.5: Image source positions for a rectangular room. Black disc: original source; Blue triangles: 1st order image sources; Orange diamonds: 2nd order image sources; Green crosses: 3rd order image sources.

source strengths are then calculated to satisfy the boundary conditions according to the pressure reflection coefficients of the surfaces [7]

$$q_i(t) = \prod_{m=1}^M R_m q_0(t). \quad (3.5)$$

In this equation q_i is the source strength of image source i , M is its order, R_m are the reflection coefficients of the surfaces on the reflection path, and q_0 is the strength of the original source. The sound field in the room is finally computed by propagating the sound pressures from the original and image sources with Green's function in free field. As a result, the wave equation is satisfied as well as the boundary conditions. The solution provided by the Image Source Method is exact in the case of a rectangular room. However, rooms with arbitrary shapes contain diffraction which cannot be modelled. In such geometries, some image sources might also be non-valid if they are not visible from the original source or the receiver. Visibility checks must therefore be performed to retain only the valid image sources.

As mentioned previously, the Image Source Method only accounts for specular reflection and does not model diffraction effect. Moreover, the number of image sources

needed in a simulation grows exponentially with the duration of the impulse response [7]. As a consequence the method becomes very heavy computationally for long impulse responses. To avoid this problem, the Image Source Method can be combined with another method. An interesting combination is the CARISM [13], and its phased version PARISM [35], where image sources treat early specular reflections and acoustical radiosity takes care of late diffuse reflections. A novel combination of image sources with the Equivalent Source Method will also be introduced in section 3.3.3.

3.2 Numerical methods for differential equations

3.2.1 Finite Difference schemes

The most straightforward way to numerically solve a differential equation is to approximate it with finite difference [33]. In acoustics, the Finite Difference in the Time Domain is most commonly used to solve the system of equations

$$\frac{\partial \mathbf{u}}{\partial t} = -\frac{1}{\rho} \nabla p, \quad (3.6)$$

$$\frac{\partial p}{\partial t} = -\rho c^2 \nabla \cdot \mathbf{u}, \quad (3.7)$$

which is equivalent to the wave equation presented in Eq. (1.1). In order to solve the system, the volume of the domain is discretized with two cartesian grids of respectively sound pressure nodes and particle velocity nodes. The grids are staggered in space and time to apply the finite difference [60]. An illustration of the staggered grids is shown in Fig. 3.6 for a one-dimensional space, where m and n respectively denote the indices of spatial steps and time steps. The system of equations is then approximated by finite difference to create the update equations. For a one-dimensional space and first order finite difference, the update equations are

$$u(m + 1/2, n + 1/2) = u(m + 1/2, n - 1/2) - \frac{1}{\rho} \frac{\Delta t}{h} (p(m + 1, n) - p(m, n)), \quad (3.8)$$

$$p(m, n + 1) = p(m, n) - \rho c^2 \frac{\Delta t}{h} (u(m + 1/2, n + 1/2) - u(m - 1/2, n + 1/2)), \quad (3.9)$$

with Δt the time resolution and h the spatial resolution. Given some initial conditions, the particle velocity and sound pressure can then be calculated alternatively for every new time step in this time-marching scheme.

The main limitation of the Finite Difference in the Time Domain is that it requires to be implemented on a cartesian grid. This leads to a staircase approximation of the boundary if the domain cannot be fitted with such a discretization. The resulting

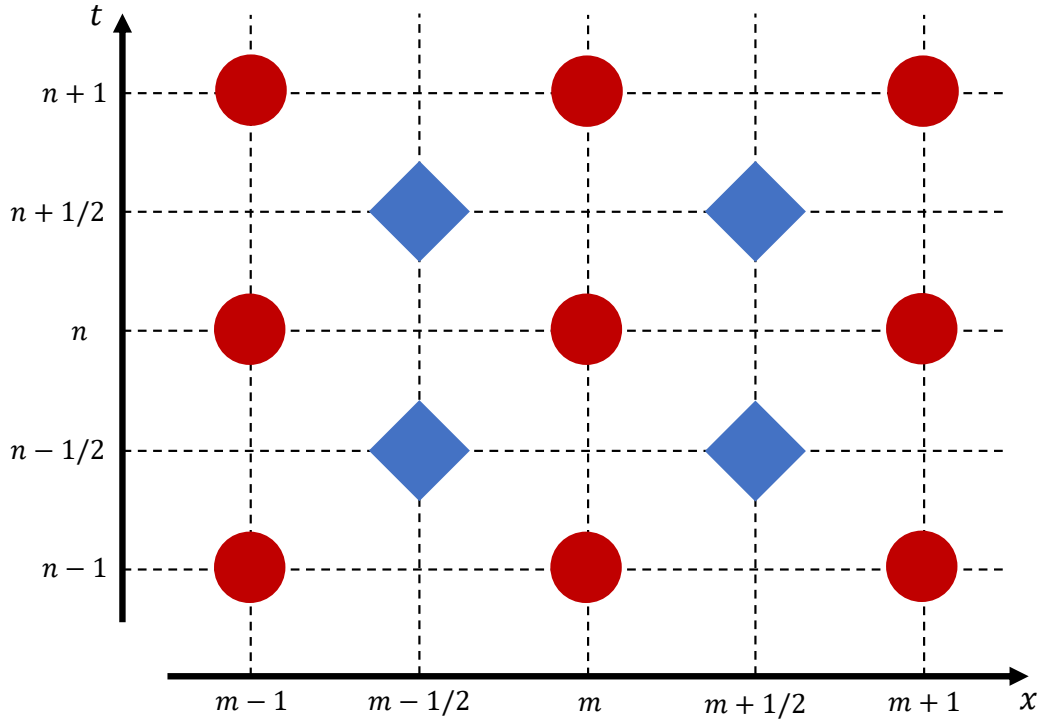


Figure 3.6: Staggered grids for the Finite Difference in the Time Domain, with space on the horizontal axis and time on the vertical axis. Red discs: sound pressure nodes; Blue diamonds: particle velocity nodes.

simulations can then be highly inaccurate [3]. As a solution the domain can be discretized with cells of arbitrary shape centered on pressure nodes, and the method is then called the Finite Volume Method [4]. In such a case the flow of velocity potential needs to be calculated at each cell interface in order to compute the update equations, which can be a tedious operation in three-dimensional space. Although it is able to operate in any geometry, one discretization drawback remains in the Finite Volume Method. The entire volume of the domain indeed needs to be meshed with cells. In addition, stability conditions and minimization of dispersion error impose finer spatial and time resolutions than other numerical methods.

3.2.2 The Finite Element Method

The Finite Element Method is a very common tool to numerically solve differential equations. Its principle is explained here in the frequency domain for a one-dimensional case [1]. Although more complicated, an implementation in the time domain and on a three-dimensional domain follows the same steps. Starting from a domain bounded between 0 and L , the Helmholtz equation is

$$c^2 \frac{d^2 p}{dx^2} + \omega^2 p = 0, \quad (3.10)$$

with prescribed boundary conditions $p(0)$ and $p(L)$. By multiplication with a weight function ϕ and integration, the wave equation can be expressed in its weak integral form

$$\int_0^L c^2 \frac{d\phi}{dx} \frac{dp}{dx} dx - \omega^2 \int_0^L \phi p dx = 0. \quad (3.11)$$

The two integrals in the equation can be seen as stiffness and mass terms, so that $K = \int_0^L c^2 \frac{d\phi}{dx} \frac{dp}{dx} dx$ and $M = \int_0^L \phi p dx$. The next step is to discretize the domain into elements. Each element e covers a portion Ω^e of the domain and is made up of $m + 1$ nodes, with m the order of the element. Shape functions N_i^e , also called basis functions, are then used to approximate the sound pressure in the elements

$$p(x) = \sum_{i=1}^{m+1} N_i^e(x) p_i^e = \mathbf{N}^e \mathbf{p}^e. \quad (3.12)$$

p_i^e is the sound pressure at node i of element e , and \mathbf{N}^e and \mathbf{p}^e are vectors which components are $N_i^e(x)$ and p_i^e . It is common practice to use polynomials as shape functions due to requirements on differentiability and nodal values. These functions are shown in Fig. 3.7 for first and second order elements. They are defined with the local variable ξ rather than x for simplicity. Following this, the stiffness and mass terms in the weak integral form can be rewritten for each element by replacing $p = \mathbf{N}^e \mathbf{p}^e$ and $\phi = (\mathbf{N}^e)^T$

$$\mathbf{K}^e = c^2 \int_{\Omega^e} \left(\frac{d\mathbf{N}^e}{dx} \right)^T \frac{d\mathbf{N}^e}{dx} dx, \quad (3.13)$$

$$\mathbf{M}^e = \int_{\Omega^e} (\mathbf{N}^e)^T \mathbf{N}^e dx. \quad (3.14)$$

Eq. (3.11) then becomes

$$\sum_{e=1}^{n_e} (\mathbf{K}^e - \omega^2 \mathbf{M}^e) \mathbf{p}^e = 0, \quad (3.15)$$

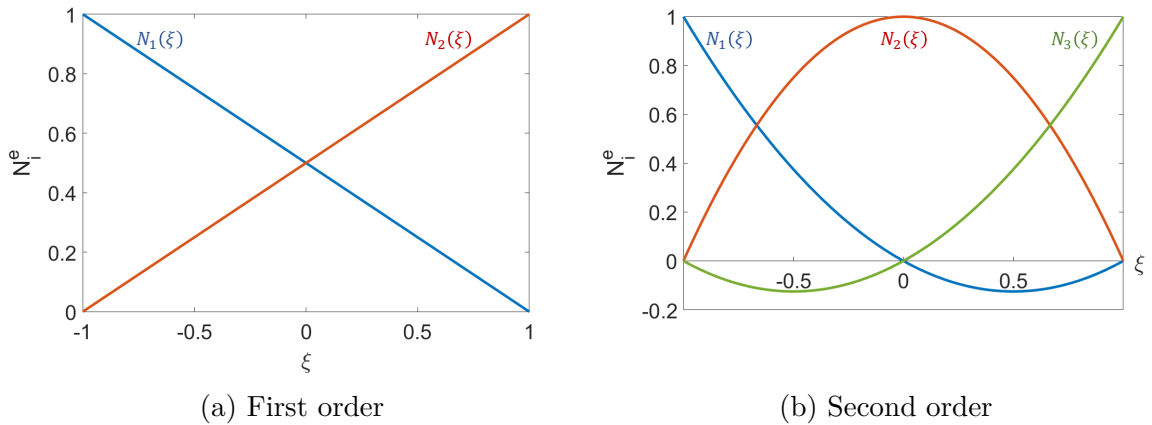


Figure 3.7: Local shape functions in the Finite Element Method.

with n_e the number of elements in the discretization. The global pressure vector \mathbf{p} comprising all the nodes is linked to the local element vectors by the localization matrices \mathbf{L}^e

$$\mathbf{p}^e = \mathbf{L}^e \mathbf{p}. \quad (3.16)$$

In these matrices, each line represents one local node in element e and each column one global node. The components of \mathbf{L}^e are then equal to 1 when the local node corresponds to a global node and equal to 0 otherwise; hence, there is only one non-zero value per line. Changing from local to global coordinates, the global stiffness and mass matrices are then

$$\mathbf{K} = \sum_{e=1}^{n_e} (\mathbf{L}^e)^T \mathbf{K}^e \mathbf{L}^e, \quad (3.17)$$

$$\mathbf{M} = \sum_{e=1}^{n_e} (\mathbf{L}^e)^T \mathbf{M}^e \mathbf{L}^e. \quad (3.18)$$

It follows that the matrix equation of the system is

$$(\mathbf{K} - \omega^2 \mathbf{M}) \mathbf{p} = 0, \quad (3.19)$$

which can be generalized to three-dimensional problems. Impedance boundary conditions can be inserted in the equation by introducing the global dissipation matrix \mathbf{C} , which is derived in the same manner as \mathbf{K} and \mathbf{M} . The matrix \mathbf{C}^e of the elements Ω_e located at a boundary with surface impedance Z_a in a three-dimensional case is calculated as

$$\mathbf{C}^e = \frac{1}{c} \int_{\partial\Omega_e} \frac{1}{Z_a} (\mathbf{N}^e)^T \mathbf{N}^e dS. \quad (3.20)$$

The resulting matrix equation is

$$(\mathbf{K} + j\omega \mathbf{C} - \omega^2 \mathbf{M}) \mathbf{p} = 0. \quad (3.21)$$

A source term can now be added to the right-hand side of the equation to investigate the transfer function of the domain, and the solution is found by inverting the matrix $\mathbf{K} + j\omega \mathbf{C} - \omega^2 \mathbf{M}$.

The inverse Fourier transform can be applied to Eq. (3.21) to obtain the time-domain formulation of the Finite Element Method [42]

$$\mathbf{M} \frac{\partial^2 \mathbf{p}}{\partial t^2} + \mathbf{C} \frac{\partial \mathbf{p}}{\partial t} + \mathbf{K} \mathbf{p}(t) = 0. \quad (3.22)$$

The first and second order derivatives in this equation need to be discretized in order to solve the problem. This can be done with Newmark methods [39], which are equivalent to different finite difference approximations. Hence, the equations of the Finite Volume Method can also be derived from the time-domain formulation of the Finite Element Method.

The Finite Element Method can return an accurate solution to the differential equation modelled. In the case of the wave equation, this means that all the reflection and diffraction phenomena are simulated accurately. Moreover the matrix to be inverted is sparse for both frequency-domain and time-domain formulations, which makes the calculations simpler and faster. However, in a three-dimensional problem, the whole volume of the domain has to be meshed. This has a significant impact on the size of the matrix and thus calculation time. As a consequence, the computational load of the Finite Element Method is too heavy to be applied to room acoustics. Its typical applications in acoustics indeed cover much smaller volumes, such as hearing aids, microphones and ducts.

3.2.3 The Boundary Element Method

The Boundary Element Method also works by solving an integral formulation of a differential equation. It can be applied to the wave equation in the time domain but it is more commonly encountered for the Helmholtz equation in the frequency domain [59]. The frequency domain case is thus presented here. The Helmholtz equation is expressed in 3D with $k = \omega/c$ as

$$\nabla^2 p + k^2 p = 0. \quad (3.23)$$

The equation is multiplied by the free-field Green's function in the frequency domain G as a weight function, and then integrated over the volume V of the domain

$$\int_V (\nabla^2 p + k^2 p) G dV = 0. \quad (3.24)$$

After a double integration by parts it is found that

$$\int_V (\nabla^2 p) G dV = \int_V (\nabla^2 G) p dV + \int_S \left(p \frac{\partial G}{\partial n} - G \frac{\partial p}{\partial n} \right) dS, \quad (3.25)$$

with S the boundary of the domain and n the normal direction to S . Eq. (3.24) then becomes

$$- \int_V p (\nabla^2 G + k^2 G) dV = \int_S \left(p \frac{\partial G}{\partial n} - G \frac{\partial p}{\partial n} \right) dS. \quad (3.26)$$

As a solution to the inhomogeneous Helmholtz equation, Green's function respects

$$\nabla^2 G + k^2 G = -\delta(\mathbf{r} - \mathbf{r}_0), \quad (3.27)$$

where \mathbf{r} denotes coordinates in the domain and \mathbf{r}_0 is the position of the source. In addition, Euler's equation allows to write

$$\frac{\partial p}{\partial n} = -\rho \frac{\partial u_n}{\partial t}, \quad (3.28)$$

with ρ the density of air and v_n the normal particle velocity at the boundary. Since Helmholtz equation assumes pure tones, the time derivative is equivalent to

$$\frac{\partial u_n}{\partial t} = j k c v_n. \quad (3.29)$$

Thanks to these relations, and after defining P as an observation point and Q as a point on the boundary, Eq. (3.26) becomes

$$C(P)p(P) = \int_S \left(p(Q) \frac{\partial G}{\partial n}(P, Q) + j\rho k c u_n(Q) G(P, Q) \right) dS, \quad (3.30)$$

with $C(P)$ being a collocation factor such that

$$C(P) = \begin{cases} 0 & \text{if } P \notin V \\ 1/2 & \text{if } P \in S \\ 1 & \text{if } P \in V \end{cases}. \quad (3.31)$$

Adding the boundary condition $u_n(Q) = Y_a(Q)p(Q)$ and a source term finally yields

$$C(P)p(P) = \int_S \left(\frac{\partial G}{\partial n}(P, Q) + j\rho k c Y_a(Q) G(P, Q) \right) p(Q) dS + p_0(P). \quad (3.32)$$

The different terms of the equation can now be linked to their physical meaning. The sound pressure at a field point $p(P)$ is the sum of direct sound from the source $p_0(P)$, sound from a monopole distribution on the boundary $\int_S j\rho k c Y_a(Q) p(Q) G(P, Q) dS$, and sound from a dipole distribution on the boundary $\int_S p(Q) \frac{\partial G}{\partial n}(P, Q) dS$. From there, the problem is solved in two steps: first the sound pressure is determined on the boundary, and then it is calculated at any desired field point. To do so the integral equation is discretized similarly to the Finite Element Method, with the difference that only the boundary of the domain needs to be meshed. The sound pressure on a boundary element e is calculated from shape functions N_i^e and nodal values p_i^e as

$$p(Q) = \sum_{i=1}^M N_i^e(Q) p_i^e = \mathbf{N}^e \mathbf{p}^e, \quad (3.33)$$

with M the number of nodes in one element. The discretization of Eq. (3.32) follows as

$$C(P)p(P) = \sum_{e=1}^{n_e} \int_{S^e} \left(\frac{\partial G}{\partial n}(P, Q) + j\rho k c Y_a(Q) G(P, Q) \right) \mathbf{N}^e dS \mathbf{p}^e + p_0(P), \quad (3.34)$$

where n_e is the total number of elements and S^e is the surface of element e . This equation takes the matrix form

$$\mathbf{C}(P)\mathbf{p} = \mathbf{A}(P, Q)\mathbf{p}_Q + \mathbf{p}_0, \quad (3.35)$$

with \mathbf{C} the diagonal matrix of collocation factors, \mathbf{p} the vector of observation points, \mathbf{p}_Q the vector of boundary points, \mathbf{p}_0 the vector of direct sound pressure at the observation points, and

$$\mathbf{A}(P, Q) = \int_{S^e} \left(\frac{\partial G}{\partial n}(P, Q) + j\rho k c Y_a(Q) G(P, Q) \right) \mathbf{N}^e dS. \quad (3.36)$$

One option to determine the sound pressure on the boundary is the collocation method. It consists in placing the observation points P in the same positions as the boundary points Q . It then follows that $\mathbf{C} = \mathbf{I}/2$ and $\mathbf{p} = \mathbf{p}_Q$, \mathbf{I} being the identity matrix. The resulting system of equations is

$$\left(\frac{\mathbf{I}}{2} - \mathbf{A}(Q, Q)\right) \mathbf{p}_Q = \mathbf{p}_0, \quad (3.37)$$

which is solved by inverting the matrix $(\mathbf{I}/2 - \mathbf{A}(Q, Q))$. Finally, once the sound pressure on the boundary is known, the sound pressure at any receiver in the domain is calculated from Eq. (3.35) with $\mathbf{C}(P) = \mathbf{I}$ and the observation points P at the desired locations.

The derivation of the problem equations follows the same steps in the time domain as in the frequency domain. The integral form before discretization in Eq. (3.32) is expressed in the time domain as [53]

$$\begin{aligned} C(P)p(P, t) = & -\frac{1}{4\pi} \int_S \frac{\partial r_{pq}}{\partial n} \left[\frac{1}{r_{pq}^2} p(Q, t - r_{pq}/c) + \frac{1}{cr_{pq}} \frac{\partial p}{\partial t}(Q, t - r_{pq}/c) \right] dS \\ & - \frac{\rho}{4\pi} \int_S \frac{1}{r_{pq}} \left[\int_0^{t-r_{pq}/c} \frac{\partial p}{\partial t}(Q, t - r_{pq}/c - \tau) y_a(Q, \tau) d\tau - \frac{\partial u}{\partial t}(Q, t - r_{pq}/c) \right] dS \\ & + p_0(P, t), \end{aligned} \quad (3.38)$$

with r_{pq} the distance between the observation point P and the boundary point Q . The time interval is then discretized with time steps $t_k = k\Delta t$, and the different variables are discretized the help of continuous interpolation functions $\psi_k(t) = \psi(t - t_k)$ [5]. The matrix form of Eq. (3.38) for observation points on the boundary at the time step $t_m = m\Delta t$, corresponding to Eq. (3.37) in the frequency domain, follows as

$$\left(\frac{\mathbf{I}}{2} + \mathbf{A}^0 + \mathbf{C}^0\right) \mathbf{p}_Q(m) = -\sum_{k=1}^m (\mathbf{A}^k + \mathbf{C}^k) \mathbf{p}_Q(m-k) + \sum_{k=0}^m \mathbf{B}^k \mathbf{u}_Q(m-k) + \mathbf{p}_0(m), \quad (3.39)$$

where the matrices \mathbf{A}^k , \mathbf{B}^k and \mathbf{C}^k are defined as

$$A_{ij}^k = \frac{1}{4\pi} \int_S \frac{\partial r_{iq}}{\partial n} \left[\frac{1}{r_{iq}^2} \psi(t_k - r_{iq}/c) + \frac{1}{cr_{iq}} \frac{\partial \psi}{\partial t}(t_k - r_{iq}/c) \right] N_j^e(Q) dS, \quad (3.40)$$

$$B_{ij}^k = \frac{\rho}{4\pi} \int_S \frac{1}{r_{iq}} \frac{\partial \psi}{\partial t}(t_k - r_{iq}/c) N_j^e(Q) dS, \quad (3.41)$$

$$C_{ij}^k = \frac{\rho}{4\pi} \int_S \frac{1}{r_{iq}} \left[\sum_{l=0}^k \frac{\partial \psi}{\partial t}(t_k - r_{iq}/c - t_l) \mathbf{N}^e \mathbf{y}_a^e(t_l) \Delta t \right] N_j^e(Q) dS. \quad (3.42)$$

The matrices \mathbf{A}^k , \mathbf{B}^k and \mathbf{C}^k are only dependent on relative times prescribed by the positions of the boundary elements. They are therefore independent of the time step, and the matrix $(\frac{\mathbf{I}}{2} + \mathbf{A}^0 + \mathbf{C}^0)$ needs to be inverted only once to solve the problem.

Similarly to the Finite Element Method, the Boundary Element Method can return an accurate solution to the wave equation modelled with its boundary conditions. It thus accounts for all the wave phenomena encountered in room acoustics. It also has the advantage that only the boundary of the domain needs to be meshed. Therefore, its computational load only grows with the surface area of the domain and not its volume. However, this advantage comes with a cost. Indeed, the matrix to be inverted is fully populated in both frequency and time domains, making the operation heavy. Due to this trade-off, the computational load of the Boundary Element Method is comparable to that of the Finite Element Method. Consequently, it is commonly used for the same range of geometries, and it is generally favored for investigations on radiation and scattering because its formulation does not require a bounded domain for exterior problems.

3.3 The Equivalent Source Method

The Equivalent Source Method is commonly used in acoustics for scattering and radiation problems [41]. It was originally formulated in the frequency domain for exterior problems [23]. Various applications have followed [6, 44, 45], including enclosures [21], street canyons [15], and large open scenes [37]. The Equivalent Source Method has also been formulated in the time domain [26]. Despite some applications to scattering problems [25, 31, 32], it remains less developed than the frequency-domain formulation. History and state-of-the-art knowledge on the Equivalent Source Method for both frequency and time formulations has recently been reviewed [30].

3.3.1 Background theory

The Equivalent Source Method is considered in the time domain in the present work. It can be seen as a compromise between the Image Source Method and the Boundary Element Method. Sources are placed outside the calculation domain and their strengths are adjusted to respect the boundary conditions, similarly to the Image Source Method. But rather than using image positions, equivalent sources are located all around the boundary of the domain in a way recalling the Boundary Element Method. An illustration of the equivalent source positions is shown in Fig. 3.8. The main elements of the theory are presented here for rigid boundaries and linear time interpolation, and complete explanations can be found in paper C. In the Equivalent Source Method, sound is assumed to propagate freely in space according to Green's function in Eq. (1.3). The acoustic problem then consists in solving the boundary condition equation. For a rigid surface, the equation at one control point on the boundary can be expressed as

$$\mathbf{u}(t) \cdot \boldsymbol{\eta}_n = 0. \quad (3.43)$$

$\mathbf{u}(t)$ is the particle velocity, and $\boldsymbol{\eta}_n$ is the normal unit vector of the surface. This equation is differentiated over time in order to apply the conservation of momentum, and sound

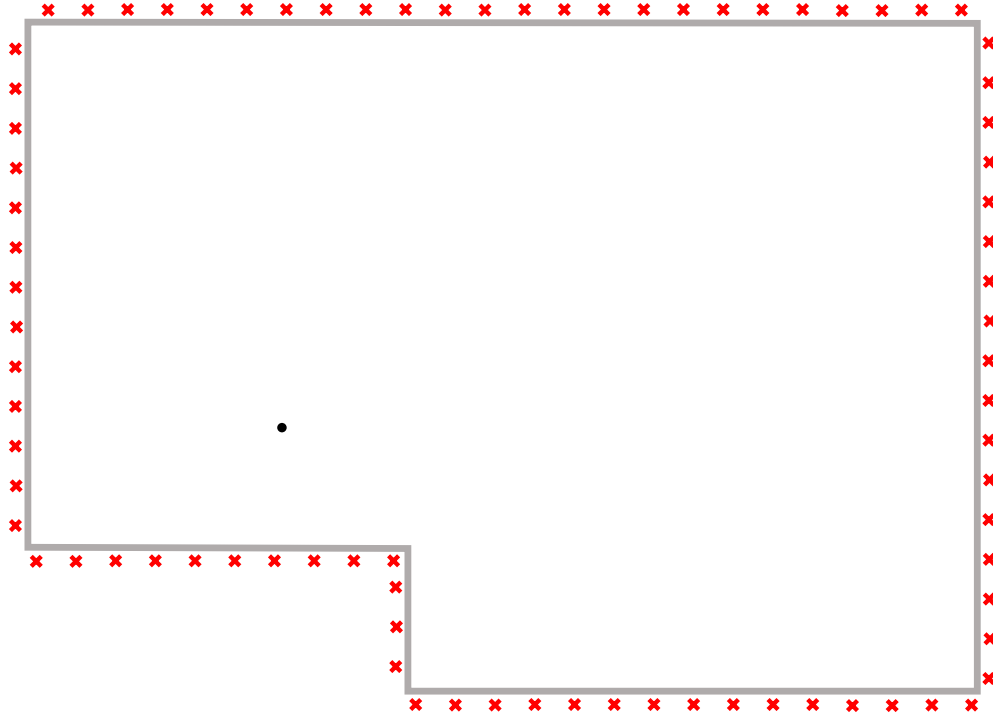


Figure 3.8: Positions of equivalent sources (red crosses) in a 2D room model.

pressure is split between incident pressure p_i and reflected pressure p_r to give

$$\nabla p_r(t) \cdot \boldsymbol{\eta}_n = -\nabla p_i(t) \cdot \boldsymbol{\eta}_n. \quad (3.44)$$

The right-hand side of this equation is fully known from data on the input signal, whereas the left-hand side contains the unknown strengths of the equivalent sources. The reflected sound pressure at one control point b can be decomposed into the sum of contributions from all equivalent sources e . The reflected sound pressure then becomes

$$p_r(t) = \frac{1}{4\pi} \sum_e \frac{q_e(t - r_{be}/c)}{r_{be}}, \quad (3.45)$$

with q_e the source strength of equivalent source e , and r_{be} the distance between control point b and source e . Consequently the gradient of the reflected sound pressure is

$$\nabla p_r(t) = \frac{1}{4\pi} \sum_e \left(-\frac{q_e(t - r_{be}/c)}{r_{be}^2} - \frac{1}{cr_{be}} \frac{\partial q_e}{\partial t}(t - r_{be}/c) \right) \boldsymbol{\eta}_{be}, \quad (3.46)$$

with $\boldsymbol{\eta}_{be}$ the unit directional vector from source e to point b . Similarities can be seen with Eq. (3.38) from the time-domain Boundary Element Method. The time domain now needs to be discretized for numerical implementation. The time resolution is noted Δt , inducing $t = n\Delta t$ with $n \in \mathbb{N}$ for the time variable, and $r_{be}/c = \nu_{be}\Delta t$ with $\nu_{be} \in \mathbb{R}$ for the travel time between equivalent source e and control point b . Δt will later be

omitted in function arguments. The integer numbers surrounding ν_{be} are noted ν_{be}^- and ν_{be}^+ such that $\nu_{be}^- \leq \nu_{be} \leq \nu_{be}^+$. From linear time interpolation, the source strength and its derivative in discrete time are expressed as

$$q_e(n - \nu_{be}) = (\nu_{be} - \nu_{be}^-)q_e(n - \nu_{be}^-) + (\nu_{be}^+ - \nu_{be})q_e(n - \nu_{be}^+), \quad (3.47)$$

$$\frac{\partial q_e}{\partial t}(n - \nu_{be}) = \frac{q_e(n - \nu_{be}^-) - q_e(n - \nu_{be}^+)}{\Delta t}. \quad (3.48)$$

The left-hand side of Eq. (3.44) in discrete time then is

$$\begin{aligned} \nabla p_r(n) \cdot \boldsymbol{\eta}_n = \frac{1}{4\pi} \sum_e \left(\left(-\frac{\nu_{be}^+ - \nu_{be}}{r_{be}^2} - \frac{1}{cr_{be}\Delta t} \right) q_e(n - \nu_{be}^-) \right. \\ \left. + \left(-\frac{\nu_{be} - \nu_{be}^-}{r_{be}^2} + \frac{1}{cr_{be}\Delta t} \right) q_e(n - \nu_{be}^+) \right) \boldsymbol{\eta}_{be} \cdot \boldsymbol{\eta}_n. \end{aligned} \quad (3.49)$$

After noting the scalar product $\sigma_{be} = \boldsymbol{\eta}_{be} \cdot \boldsymbol{\eta}_n$, the factors multiplying $q_e(n - \nu_{be}^-)$ and $q_e(n - \nu_{be}^+)$ can be arranged respectively in matrices \mathbf{A} and \mathbf{B} so that

$$A_{be} = \frac{1}{4\pi} \left(-\frac{\nu_{be}^+ - \nu_{be}}{r_{be}^2} - \frac{1}{cr_{be}\Delta t} \right) \sigma_{be}, \quad (3.50)$$

$$B_{be} = \frac{1}{4\pi} \left(-\frac{\nu_{be} - \nu_{be}^-}{r_{be}^2} + \frac{1}{cr_{be}\Delta t} \right) \sigma_{be}. \quad (3.51)$$

Next, the matrices are decomposed according the values of ν_{be}^- and ν_{be}^+ . These values are sorted as

$$\nu_0 = \min(\nu_{be}^-), \quad (3.52)$$

$$\nu_k = \nu_0 + k, \quad (3.53)$$

with $k \in \mathbb{N}$. The decomposition is then defined as

$$\mathbf{A} = \sum_{k=0}^n \mathbf{A}_k, \quad (3.54)$$

$$\mathbf{B} = \sum_{k=1}^n \mathbf{B}_k, \quad (3.55)$$

where

$$A_{k,be} = \begin{cases} A_{be} & \text{if } \nu_{be}^- = \nu_k \\ 0 & \text{otherwise} \end{cases}, \quad (3.56)$$

$$B_{k,be} = \begin{cases} B_{be} & \text{if } \nu_{be}^+ = \nu_k \\ 0 & \text{otherwise} \end{cases}. \quad (3.57)$$

Following this, the final matrix form of Eq. (3.44) is found to be

$$\mathbf{A}_0 \mathbf{q}(n - \nu_0) = -\nabla \mathbf{p}_i(n) \cdot \boldsymbol{\eta}_n - \sum_{k=1}^n (\mathbf{A}_k + \mathbf{B}_k) \mathbf{q}(n - \nu_k). \quad (3.58)$$

The size and values of the matrices \mathbf{A} and \mathbf{B} depend on the discretization of the domain boundary. Equivalent sources are commonly distributed uniformly with spacing h_s around the boundary, although random positions can also be used [43]. The orthogonal distance between the sources and the boundary is noted d . Control points have also been distributed uniformly over the boundary surfaces in the literature. Nevertheless, a sparse distribution has been shown to be an efficient discretization of the boundary in paper D. It consists in defining 4 control points per equivalent source placed in a square with side h_p centered on the orthogonal projection of the source on the surface. The uniform and sparse distributions are illustrated in Fig. 3.9. It is seen that a sparse distribution allows to greatly reduce the number of control points and thereby the size of the problem.

The Equivalent Source Method cumulates advantages from the Boundary and Finite Element Methods. Indeed, only the boundary of the domain needs discretization, and the matrix \mathbf{A}_0 inverted to solve the problem is sparse. Moreover, \mathbf{A}_0 is time-independent. This means that the matrix inversion is performed only once, and the operation to calculate the source strengths at a new time step consists of a matrix multiplication. As a result, the computation time of simulations grows linearly with the duration of the impulse response calculated. The computation efficiency of the Equivalent Source Method in the time domain makes it an attractive solution for room acoustic simulations.

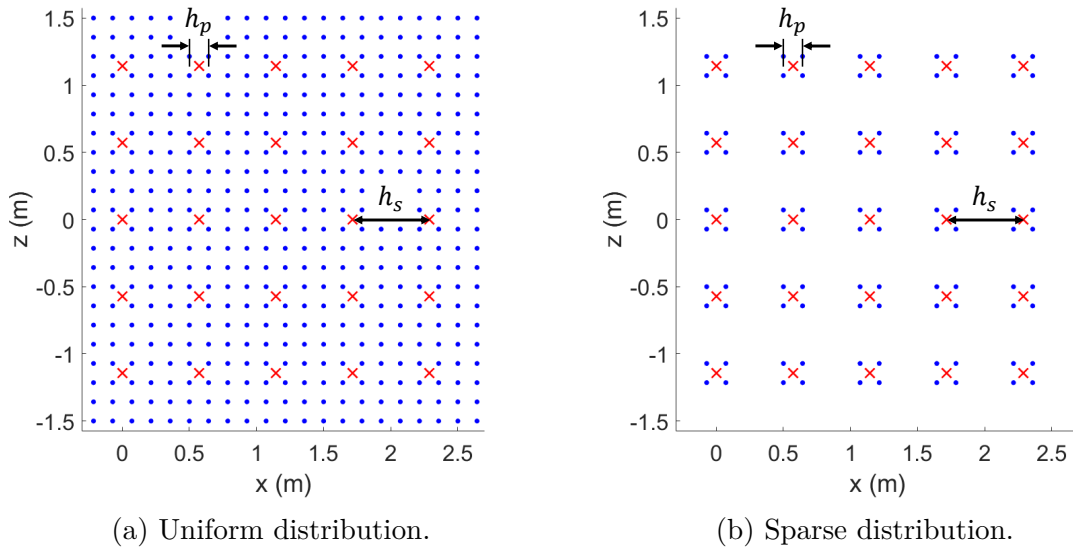


Figure 3.9: Close-up front view of the discretization of a surface, from paper D. Blue dots: control points; Red crosses: equivalent sources.

Its accuracy and its application to interior problems have therefore been investigated in paper C.

3.3.2 Parametric study

This section presents the main findings of paper C. In this study, the Equivalent Source Method in the time domain was implemented with a uniform distribution of control points, as seen in Fig. 3.10. The method was first tested with the reflection of sound on a finite and rigid plate. The aim was to investigate its fundamental behaviour with regards to the geometric parameters d , h_s and h_p . Results showed that simulations become unstable when equivalent sources have a large influence on the responses of their neighbour sources, and reciprocally. The equivalent sources thus should be placed close enough to the surface they discretize in order to avoid this instability. In terms of geometric parameters, the positions of equivalent sources should respect

$$\frac{d}{L} < \frac{1}{3}, \quad (3.59)$$

with $L = \sqrt{d^2 + h_s^2}$. The investigation on the finite plate test case pointed out another behaviour of the Equivalent Source Method. For small values of d , the amplitude of the reflected sound field tends to be overestimated. As d increases and the equivalent sources are located further from the surface, the amplitude of the reflected sound field decreases and is eventually underestimated. This behaviour is illustrated in Fig. 3.11 where the sound pressure calculated at a receiver point in front of the plate is shown for two orthogonal distances d . As a consequence, there exists a value d_0 between overestimation and underestimation where the error of the Equivalent Source Method is minimal. Through regression analysis, this value was found to be related to the other

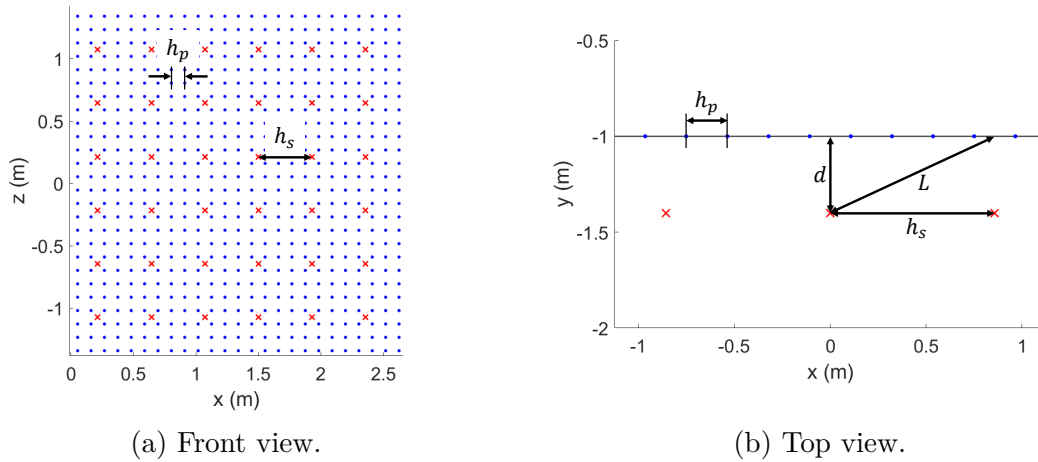


Figure 3.10: Close-up illustration of the discretization of a surface in the Equivalent Source Method, from paper C. Blue dots: control points; Red crosses: equivalent sources.

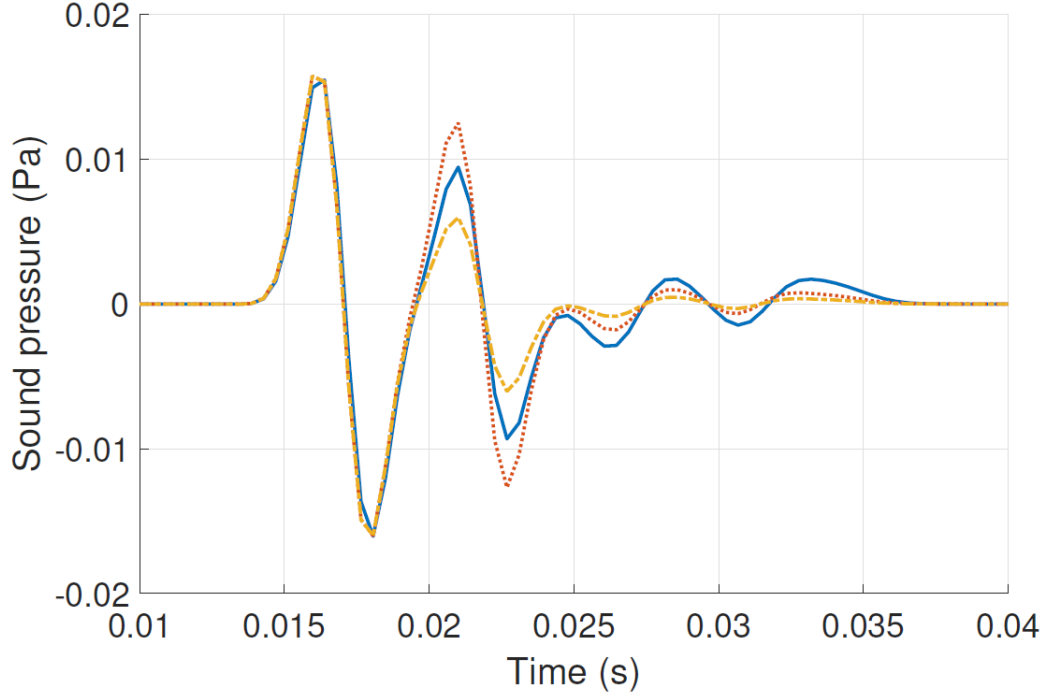


Figure 3.11: Sound pressure at a receiver point in front of a finite plate for $h_p = 143$ mm and $\kappa = 4$, from paper C. Solid blue line: reference sound pressure; Dotted red line: ESM with $d/L = 0.022$; Dash-dotted yellow line: ESM with $d/L = 0.066$.

geometric parameters as

$$\frac{d_0}{\sqrt{d_0^2 + h_s^2}} = 3\kappa^{-3}. \quad (3.60)$$

After unveiling its properties with regards to geometric parameters, the Equivalent Source Method in the time domain has been applied to an interior problem. The impulse response of a rectangular box was simulated in two cases, one with rigid boundaries and the other with constant and uniform surface impedance $Z_a = 3\rho c$. Both cases highlighted the propagation of errors in the simulation. When equivalent sources are close to the surfaces, the overestimation of the reflected amplitude is replicated at every reflection in the room. Hence, the amplitude of the sound field rises with time, which leads to instability. Similarly, when equivalent sources are placed further away from the surfaces, the underestimation of the reflected sound field occurs at every reflection and results in large numerical damping as shown in Fig. 3.12.

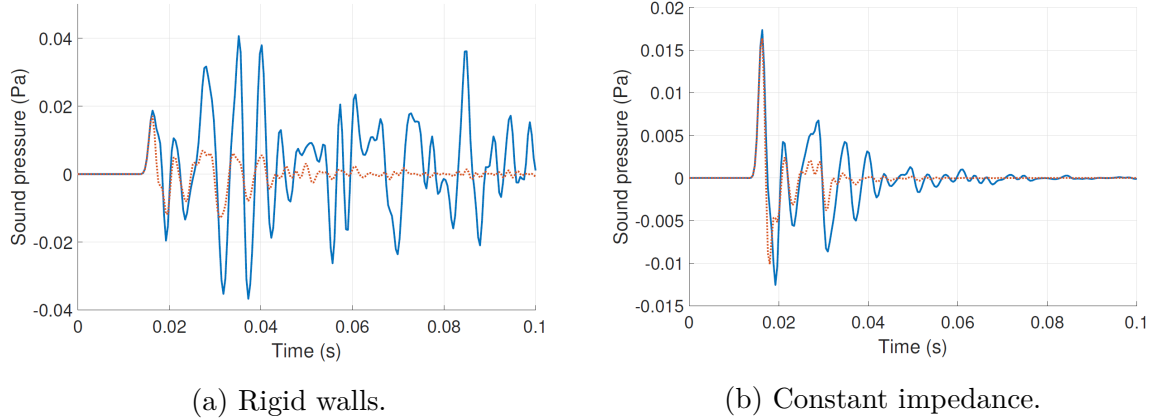


Figure 3.12: Sound pressure at a receiver point in a rectangular box for $h_p = 143$ mm, $\kappa = 4$ and $d/L = 0.094$, from paper C. Solid blue line: reference sound pressure; Dotted red line: Equivalent Source Method.

3.3.3 Combination of image and equivalent sources

The Image-Equivalent Source Method has been introduced in paper D. It consists in combining image and equivalent sources into the same algorithm. This novel combination aims at overcoming the respective drawbacks of the two individual methods. Image sources are indeed very efficient to model specular reflections, but the computational load associated with the maximum image order required grows exponentially with the duration of the impulse response calculated. Moreover, diffraction effects cannot be modelled with image sources. On the other hand, the computation time of the Equivalent Source Method grows linearly with the duration of the impulse response. The modelling of successive specular reflections in a room was however found to be highly inaccurate due to numerical damping. The integration of low-order image sources to the equivalent source algorithm thus allows to accurately simulate the early part of the room response, while late reflections and diffraction effects are accounted for by equivalent sources.

On top of the expected advantages on accuracy and efficiency, image and equivalent sources can be combined in a simple process. The calculations are based on the algorithm of the Equivalent Source Method where only the construction of the incident sound field is modified. Image sources are first determined up to an arbitrary order. The incident sound pressure is then defined as the sum of the contributions from the original source in the room and from the K image sources considered

$$p_i(t) = \sum_{k=0}^K p_k(t). \quad (3.61)$$

The individual contributions $p_k(t)$ of the image sources are calculated according to Eq. (3.5). The incident sound pressure is then injected in Eq. (3.44), and the derivation of the problem equations follows the steps explained in section 3.3.1.

The Image-Equivalent Source Method has been applied to the rectangular box with impedance boundaries test case from paper C. A large gain in accuracy was found compared to the simulations performed with the Equivalent Source Method. These promising results are a good sign of the proper functioning of the algorithm. Nevertheless, the error estimate of the simulations was biased due to the fact that the Image Source Method was used to compute the reference impulse response. Consequently, the Image-Equivalent Source Method awaits further investigation to validate its applicability to room acoustics.

CHAPTER 4

Discussion

The present study has introduced a method to convert absorption coefficients measured in reverberation chambers into surface impedances. The impedance retrieval method has been shown to be robust and efficient thanks to the constrained optimization problem set up and to the RMK+1 impedance model defined. It can thus be employed to improve the accuracy of boundary conditions and thereby the accuracy of room acoustics simulations. However, a few limitations exist and should be kept in mind. The method retrieves an approximate surface impedance expressed with a general model. Fine frequency variations due to cavity phenomena, for example, therefore cannot be captured. Another approximation is made with the assumption of local reaction. Nevertheless, the surface impedances retrieved with the proposed method can be reliable and carry valuable phase information. The impedance retrieval method thus constitutes an improvement of the description of boundaries in room acoustics.

With reliable surface impedance boundary conditions available, simulations of room acoustics with phased and time-domain methods become closer to practical applications. Time-domain calculations appear as the best solutions for low-frequency room acoustics due to computation efficiency considerations. The Equivalent Source Method in the time domain has therefore been investigated with the perspective of solving interior problems. Its formulation allows to solve the acoustic problem modelled by inverting a sparse matrix. The inversion operation is performed only once, and the solution at a given time step is then computed by multiplying the inverted matrix with a vector comprising known information from already calculated past time steps. Moreover, the simulation domain is discretized only on its boundary, thus limiting the size of the system of equations considered. For these reasons, the Equivalent Source Method has the potential to perform room acoustic simulations in a timely manner. However, despite its attractiveness, the results obtained indicate that this method is not suited to room acoustics due to the propagation of errors with multiple reflections on surfaces.

Advantage can nonetheless be taken from the computation efficiency of the Equivalent Source Method. By adding low-order image sources to the algorithm, its inaccuracy can be mitigated while avoiding the prohibitive computational load of the Image Source Method for long impulse responses. Hence, the Image-Equivalent Source Method has been introduced. This novel combination remains to be validated, but preliminary results seem encouraging to pursue further research.

CHAPTER 5

Conclusion

The present project has treated the issue of room acoustic simulations at low frequencies. In order to obtain accurate results, the acoustic problem needs to be described with a proper mathematical model that includes propagation of sound and characterization of boundary conditions. In addition, the method employed to solve the problem should be computationally efficient to enable practical applications.

The first objective of the project was to design a method allowing to accurately characterize boundary conditions from the available data on room acoustic materials. To do so, a general impedance model that can fit the surface impedances of most materials was pursued. After testing several options, the RMK+1 model was found to be the best solution. It is based on the classic damped oscillator model, to which a fractional term has been added. Following this, an inverse method to convert absorption coefficients measured in reverberation chambers into surface impedances was established. The method consists in solving an optimization problem provided with constraints according to prior information on the type of material considered. It has first been shown that such a method combined with the general impedance model was capable of retrieving theoretical surface impedances with reasonable accuracy. The robustness of the method was then proven. Iterative retrievals of impedances indeed concluded that the constraints associated with the optimization problem limited the space of variables to a unique solution. Moreover, impedance retrieval from measured absorption data indicated that the method proposed does not suffer from deviations in the input data and does not introduce any deviation either. Thus, the impedance retrieval method introduced in this project enables the characterization of common room acoustic materials with surface impedance from the data currently available.

Improvements of the impedance retrieval method can be achieved from further research. The constraints defined for different types of materials could be extended to include materials that have not been covered in the study carried out. Moreover, the choice of which constraints to apply to a retrieval case is currently made manually from prior information. A method to automatically detect the constraints needed from the absorption coefficient data would therefore be a great complement.

The second objective of the project consisted in finding a simulation method for room acoustics that exhibits computation efficiency and accuracy at low frequencies. The focus was put on investigating the Equivalent Source Method in the time domain due its apparent advantages regarding efficiency. This investigation has allowed to further the understanding of the method for both exterior and interior problems. Indeed, stability

conditions on the geometric parameters prescribing the discretization of surfaces have been established. Guidelines have also been suggested for accurate modelling of sound reflection over flat surfaces. Moreover, a discretization technique has been introduced that can lead to large gains in terms of computation time. When applied to interior problems, it has been found that the errors in the sound field propagate and are amplified at every new reflection. This propagation of errors thus causes either unstable simulations or large numerical damping. The Image-Equivalent Source Method has consequently been introduced in an attempt to limit the inaccuracy of the Equivalent Source Method in interior problems. This novel hybrid method combines low-order image sources that model early specular reflections and equivalent sources that account for late reflections and diffraction effects. The preliminary study carried out suggests that accurate simulations of interior problems could potentially be achieved with this method.

The study of the Equivalent Source Method in the time domain could be deepened as only the geometric parameters have been investigated in this work. The influences of the time resolution, the spectral content of the input signal, and the size of the surfaces discretized could notably be examined. A study focusing on the modelling of diffraction effects with equivalent sources would also give precious knowledge on the method. Besides, research can be pursued on the Image-Equivalent Source Method to assess its validity in room acoustics.

Bibliography

- [1] N. Atalla and F. Sgard. *Finite element and boundary methods in structural acoustics and vibration*. Boca Raton, United States of America: CRC Press, 2017. Chapter 4, pages 63–83.
- [2] B. Berglund, T. Lindvall, and D. H. Schwela. *Guidelines for community noise*. Geneva, Switzerland: Worlds Health Organization, 1999.
- [3] S. Bilbao. “Modelling of complex geometries and boundary conditions in Finite Difference/Finite Volume Time Domain room acoustics simulation.” In: *IEEE Trans. Audio Speech Lang. Processing* 21.7 (2013), pages 1524–1533.
- [4] S. Bilbao et al. “Finite Volume Time Domain room acoustics simulation under general impedance boundary conditions.” In: *IEEE Trans. Audio Speech Lang. Processing* 24.1 (2016), pages 161–173.
- [5] M. J. Bluck and S. P. Walker. “Analysis of three-dimensional transient acoustic wave propagation using the boundary integral equation method.” In: *Int. J. Numer. Meth. Eng.* 39.8 (1996), pages 1419–1431.
- [6] A. Boag, Y. Leviatan, and A. Boag. “Analysis of three-dimensional acoustic scattering from doubly periodic structures using a source model.” In: *J. Acoust. Soc. Am.* 91.2 (1992), pages 572–580.
- [7] J. Borish. “Extension of the image model to arbitrary polyhedra.” In: *J. Acoust. Soc. Am.* 75.6 (1984), pages 1827–1836.
- [8] J. Brunskog. “The forced sound transmission of finite single leaf walls using a variational technique.” In: *J. Acoust. Soc. Am.* 132.3 (2012), pages 1482–1493.
- [9] S. Das and I. Pan. *Fractional order signal processing: Introductory concepts and applications*. Heidelberg, Germany: Springer, 2012. Chapter 1, pages 1–12.
- [10] J. L. Davy et al. “The average specific forced radiation wave impedance of a finite rectangular panel.” In: *J. Acoust. Soc. Am.* 136.2 (2014), pages 525–536.
- [11] D. G. Duffy. *Green’s functions with applications*. 1st edition. Boca Raton, United States of America: CRC Press, 2001. Chapter 3.
- [12] A. P. French. *Vibrations and waves*. New York, United States of America: Norton, 1971. Chapter 8.

- [13] J. Brunskog G. Koutsouris, C.-H. Jeong, and F. Jacobsen. “Combination of acoustical radiosity and the image source method.” In: *J. Acoust. Soc. Am.* 133.6 (2013), pages 3963–3975.
- [14] M. Hodgson. “Evidence of diffuse surface reflections in rooms.” In: *J. Acoust. Soc. Am.* 89.2 (1991), pages 765–771.
- [15] M. Hornikx and J. Forssén. “The 2.5-dimensional equivalent sources method for directly exposed and shielded urban canyons.” In: *J. Acoust. Soc. Am.* 122.5 (2007), pages 2532–2541.
- [16] ISO 10534-1:1996. *Acoustics – Determination of sound absorption coefficient and impedance in impedance tubes – Part 1: Method using standing wave ratio*. Geneva, Switzerland: International Organization for Standardization, 1996.
- [17] ISO 10534-2:1998. *Acoustics – Determination of sound absorption coefficient and impedance in impedance tubes – Part 2: Transfer-function method*. Geneva, Switzerland: International Organization for Standardization, 1998.
- [18] ISO 354:2003. *Acoustics – Measurement of sound absorption in a reverberation room*. Geneva, Switzerland: International Organization for Standardization, 2003.
- [19] F. Jacobsen and P. M. Juhl. *Fundamentals of general linear acoustics*. Chichester, United Kingdom: John Wiley & Sons Ltd, 2013. Chapter 2, pages 5–10.
- [20] H. Jeong and Y. W. Lam. “FDTD modelling of frequency dependent boundary conditions for room acoustics.” In: *Proc. 20th Int. Congr. Acoust.* Sidney, Australia (2010), 7 pages.
- [21] M. E. Johnson et al. “An equivalent source technique for calculating the sound field inside an enclosure containing scattering objects.” In: *J. Acoust. Soc. Am.* 104.3 (1998), pages 1221–1231.
- [22] L. E. Kinsler et al. *Fundamentals of acoustics*. 4th ed. New York, United States of America: John Wiley and Sons, Inc., 1999.
- [23] R. Kress and A. Mohsen. “On the simulation source technique for exterior problems in acoustics.” In: *Math. Method Appl. Sci.* 8.4 (1986), pages 585–597.
- [24] A. Krokstad, S. Strøm, and S. Sørsdal. “Calculating the acoustical room response by the use of a ray tracing technique.” In: *J. Sound Vib.* 8.1 (1968), pages 118–125.
- [25] W. Kropp and P. U. Svensson. “Application of the time domain formulation of the method of equivalent sources to radiation and scattering problems.” In: *Acustica* 81 (1995), pages 528–543.
- [26] W. Kropp and P. U. Svensson. “Time domain formulation of the method of equivalent sources.” In: *Acta Acustica* 3.1 (1995), pages 67–73.
- [27] A. Kulowski. “Algorithmic representation of the ray tracing technique.” In: *Appl. Acoust.* 18 (1985), pages 449–469.
- [28] H. Kuttruff. *Room acoustics*. 5th ed. London, United Kingdom: Taylor and Francis, 2009. Chapter 7, pages 221–229.

- [29] H. Kuttruff. *Room acoustics*. 5th ed. London, United Kingdom: Taylor and Francis, 2009. Chapter 4, pages 121–126.
- [30] S. Lee. “Review: The use of equivalent source method in computational acoustics.” In: *J. Comput. Acoust.* 25.1 (2017), 1630001 (19 pages).
- [31] S. Lee, K. S. Brentner, and P. J. Morris. “Acoustic Scattering in the time domain using an equivalent source method.” In: *AIAA J.* 48.12 (2010), pages 2772–2780.
- [32] S. Lee, K. S. Brentner, and P. J. Morris. “Assessment of time-domain equivalent source method for acoustic scattering.” In: *AIAA J.* 49.9 (2011), pages 1897–1906.
- [33] R. J. LeVeque. *Finite difference methods for ordinary and partial differential equations: Steady-state and time-dependent problems*. Philadelphia, United States of America: SIAM, 2007.
- [34] T. Lewers. “A combined beam tracing and radiant exchange computer model of room acoustics.” In: *Appl. Acoust.* 38 (1993), pages 161–178.
- [35] G. Marbjerg et al. “Development and validation of a combined phased acoustical radiosity and image source model for predicting sound fields in rooms.” In: *J. Acoust. Soc. Am.* 138.3 (2015), pages 1457–1468.
- [36] L. E. Maxwell and G. W. Evans. “Chronic noise exposure and reading deficits: The mediating effects of language acquisition.” In: *Environ. Behav.* 29.5 (1997), pages 638–656.
- [37] R. Mehra et al. “Wave-based sound propagation in large open scenes using an equivalent source formulation.” In: *ACM Trans. Graph.* 32.2 (2013), pages 1–13.
- [38] D. Mintzer. “Transient sounds in rooms.” In: *J. Acoust. Soc. Am.* 22.3 (1950), pages 341–352.
- [39] N. M. Newmark. “Method of computation for structural dynamics.” In: *Proc. Am. Soc. Civil Eng.* 85 (1959), pages 67–94.
- [40] E.-M. Nosal, M. Hodgson, and I. Ashdown. “Improved algorithms and methods for room sound-field prediction by acoustical radiosity in arbitrary polyhedral rooms.” In: *J. Acoust. Soc. Am.* 116.2 (2004), pages 970–980.
- [41] M. Ochmann. “The source simulation technique for acoustics radiation problems.” In: *Acustica* 81.6 (1995), pages 512–527.
- [42] T. Okuzono et al. “Fundamental accuracy of time domain finite element method for sound-field analysis of rooms.” In: *Appl. Acoust.* 71 (2010), pages 940–946.
- [43] G. Pavić. “An engineering technique for the computation of sound radiation by vibrating bodies using substitute sources.” In: *Acta Acust. United Ac.* 91.1 (2005), pages 1–16.
- [44] S. Ramakrishna and P. R. Stepanishen. “Acoustic scattering from cylinders with a plane of symmetry using internal multipole line source distributions I.” In: *J. Acoust. Soc. Am.* 93.2 (1993), pages 658–672.

- [45] S. Ramakrishna and P. R. Stepanishen. “Acoustic scattering from cylinders with a plane of symmetry using internal multipole line source distributions II.” In: *J. Acoust. Soc. Am.* 93.2 (1993), pages 673–682.
- [46] S. W. Rienstra. “Impedance models in time domain including the extended Hemholtz resonator model.” In: *Proc. 12th AIAA/CAS Aeroacoust. Conf.* Cambridge, United States of America (2006), Paper 2006–2686.
- [47] J. H. Rindel. “An impedance model for estimating the complex reflection factor.” In: *Proc. Forum Acusticum* (2011), pages 1535–1540.
- [48] J. H. Rindel. “Evaluation of room acoustic qualities and defects by use of auralization.” In: *Proc. 148th Meet. Acoust. Soc. Am.* San Diego, United States of America (2004), 1pAA1 (16 pages).
- [49] J. H. Rindel, G. B. Nielsen, and C. L. Christensen. “Diffraction around corners and over wide barriers in room acoustic simulations.” In: *Proc. 16th Int. Congr. Sound Vib.* Krakow, Poland (2009).
- [50] T. Sakuma, S. Sakamoto, and T. Otsuru. *Computational simulation in architectural and environmental acoustics: Methods and applications of wave-based computation*. Tokyo, Japan: Springer, 2014.
- [51] L. Savioja and U. P. Svensson. “Overview of geometrical room acoustic modelling techniques.” In: *J. Acoust. Soc. Am.* 138.2 (2015), pages 708–730.
- [52] A. Smith. “Noise, performance efficiency and safety.” In: *Int. Arch. Occup. Environ. Health* 62.1 (1990), pages 1–5.
- [53] T. Terai and Y. Kawai. “The application of Kirchhoff’s formula to the numerical calculation of transient response in an enclosure.” In: *J. Acoust. Soc. Jpn.* 11.1 (1990), pages 1–10.
- [54] S. I. Thomasson. “On the absorption coefficient.” In: *Acustica* 44 (1980), pages 265–273.
- [55] S. I. Thomasson. *Theory and experiments on the sound absorption as function of the area, Report No. TRITA-TAK-8201*. Stockholm, Sweden: Department of Technical Acoustics, Royal Institute of Technology, 1982.
- [56] M. L. S. Vercammen. “Improving the accuracy of sound absorption measurement according to ISO 354.” In: *Proc. Int. Symp. Room Acoust.* Melbourne, Australia (2010).
- [57] M. Vorländer. *Auralization: Fundamentals of acoustics, modelling, simulation, algorithms and acoustic virtual reality*. Berlin Heidelberg, Germany: Springer, 2008.
- [58] A. Wareing and M. Hodgson. “Beam-tracing model for predicting sound fields in rooms with multilayer bounding surfaces.” In: *J. Acoust. Soc. Am.* 118.4 (2005), pages 2321–2331.

- [59] Y. Yasuda and T. Sakuma. “Boundary Element Method.” In: *Computational simulation in architectural and environmental acoustics: Methods and applications of wave-based computation*. Edited by T. Sakuma, S. Sakamoto, and T. Otsuru. Tokyo, Japan: Springer, 2014. Chapter 4, pages 79–92.
- [60] K. S. Yee. “Numerical solution to initial boundary value problems involving Maxwell’s equations in isotropic media.” In: *IEEE Trans. Antennas Propag.* 14.3 (1966), pages 302–307.

Appendices

APPENDIX **A**

Retrieving complex surface impedances from statistical absorption coefficients



Retrieving complex surface impedances from statistical absorption coefficients

Boris MONDET¹; Jonas BRUNSKOG²; Cheol-Ho JEONG³; Jens Holger RINDEL⁴

^{1,2,3} Acoustic Technology, DTU Electrical Engineering, Technical University of Denmark

^{1,4} Odeon A/S, Scion-DTU, Denmark

ABSTRACT

In room acoustic simulations the surface materials are commonly represented with energy parameters, such as the absorption and scattering coefficients, which do not carry phase information. This paper presents a method to transform statistical absorption coefficients into complex surface impedances which are needed for phased or time-domain calculation methods. An impedance model based on fractional calculus is suggested to achieve a general model for common acoustic materials. The parameters governing the model are determined by solving an optimisation problem, with constraints ensuring that the impedance found has a physical meaning and respects causality in the time domain. Known material models, such as Miki's and Maa's models, are taken as references to assess the validity of the suggested model. Due to the non-uniqueness of retrieving complex-valued impedances from real-valued absorption coefficients, prior information about the absorber of interest can be used as constraints, which is shown to help determine the correct impedance from absorption coefficient. Further stability and sensitivity investigations indicate that the method presented constitutes an efficient solution to convert sound absorption coefficients back to their original complex surface impedances.

Keywords: Phase retrieval, Surface impedance, Absorption coefficient

I-INCE Classification of Subjects Number: 76

1. INTRODUCTION

Room acoustic simulations have seen a great development in the last thirty years, and nowadays they are used worldwide by acoustic practitioners to predict the behaviours of newly designed renovated rooms. Current software offering room acoustic simulations are based on geometrical acoustics, a high-frequency approximation yielding accurate results above Schroeder's frequency with relatively short computation times. However, problems arise at low frequencies or in small rooms: assumptions behind geometrical acoustics do not hold due to the low modal density, and traditional wave-based methods, such as boundary or finite element methods (BEM, FEM), finite volume method (FVM), or finite difference in the time domain (FDTD), are too time-consuming for practical applications. A possible solution would be to create a hybrid method combining the speed of geometrical acoustics and the accuracy of wave-based methods. Such a hybridization requires an adequate yet different description of the boundary conditions. Indeed, geometrical acoustics only requires energy parameters like absorption and scattering coefficients, which are widely available, whereas wave-based methods need a phased representation of the boundary with complex surface impedances or pressure reflection coefficients. These phased representations are not available for most of the materials encountered in room acoustics, according to ISO 10534 (1) it is only possible to measure such quantities for normal incidence. A compromised solution would be to retrieve the surface impedance from statistical absorption coefficient, which is the main aim of the present paper.

¹ bojmo@elektro.dtu.dk

² jbr@elektro.dtu.dk

³ chj@elektro.dtu.dk

⁴ jhr@odeon.dk

2. CURRENT BOUNDARY REPRESENTATION

2.1 Statistical absorption coefficient

In 1982, Thomasson (2) defined three different absorption coefficients: the statistical absorption coefficient, its approximated version, and the alternative absorption coefficient. The method presented in this paper aims at transforming absorption coefficients, which are assumed to have been measured in reverberation chambers. The statistical absorption coefficient is thus considered; for a given frequency, it can be expressed as

$$\alpha_s = 8 \int_0^{\pi/2} \frac{\operatorname{Re}(Z_a(\theta)) \sin \theta}{|Z_a(\theta) + Z_r(\theta)|^2} d\theta \quad (1)$$

where θ is the incidence angle of the sound wave, Z_a is the surface impedance of the material, and $Z_r(\theta)$ is the radiation impedance of the sample studied. All the acoustic impedances expressed in this paper are normalized by the characteristic impedance of air $\rho_0 c_0$. Thomasson (2), Rindel (3), and Davy et al. (4) successively proposed formulas for the radiation impedance, with Davy et al. being the only ones to suggest a unique formula for all frequencies yielding a complex impedance. For a rectangular sample, and assuming that the speed of sound is larger in the material studied than in air, it can be calculated with equations (53-63) from reference (4). In addition to the incidence angle, it should be noted that the radiation impedance is also dependent on the size of the sample; for an infinite sample, its value tends to $1/\cos \theta$. The international standard for reverberation chamber measurements (5) recommends relatively square samples with areas between 10 m^2 and 12 m^2 . Therefore, in this study, it is assumed that all the samples have a square shape and an area of 11 m^2 .

2.2 From absorption coefficient to surface impedance

The surface impedance is the ratio of sound pressure and particle velocity at a boundary. It can be decomposed into resistance and reactance, corresponding respectively to the real and imaginary parts. This quantity alone is assumed to be enough to give a complete representation of the boundary. The surface impedance is related to the pressure reflection coefficient by the formula

$$R(\theta) = \frac{Z_a(\theta) - Z_r(\theta)}{Z_a(\theta) + Z_r(\theta)}, \quad (2)$$

and to the statistical absorption coefficient by equation (1). Nevertheless, some conditions have to be respected to ensure that the surface impedance is physically feasible, as explained by Rienstra (6). If the boundary is a passive system it cannot give any energy to the sound wave, then the resistance must be positive:

$$\operatorname{Re}(Z_a(\omega)) \geq 0 \quad \text{for all } \omega \in \mathbb{R}, \quad (3)$$

ω being the angular frequency. The other conditions are related to the time domain surface impedance $Z_a(t)$. Like any physical representation, $Z_a(t)$ must respect causality. This implies in the frequency domain:

$$Z_a(\omega) \text{ analytic for } \operatorname{Im}(\omega) < 0, \quad (4)$$

with the $e^{j\omega t}$ convention. Moreover, $Z_a(t)$ is meant as a real quantity, and thus the following equality must be satisfied for the conjugate of the surface impedance:

$$Z_a^*(\omega) = Z_a(-\omega). \quad (5)$$

Several authors have attempted to retrieve surface impedances from absorption coefficients. In 2011, Rindel (7) modelled three types of sound absorbers as resonant systems: porous absorbers, membranes, and resonators. He notably pointed out the non-uniqueness of solutions when transforming an absorption coefficient into surface impedance by differentiating soft and hard surfaces. An illustration of this non-uniqueness is given in Figure 1, where isolines of the statistical absorption coefficient are plotted as a function of surface impedance for a given ke , the product of the wavenumber and the characteristic length of the sample. Because the statistical absorption coefficient is an energy parameter, there is an infinite number of complex surface impedances corresponding to any value it can take, as seen with the almost circular isolines. Therefore, extra information is needed in addition to the absorption coefficient to retrieve the right impedance, such as the frequency dependence and some other constraints. Figure 1 also gives an illustration of the point of maximal absorption coefficient. With some variations according to the value of ke , the surface impedance leading to the highest absorption coefficient is approximately $Z_a = 1.6$.

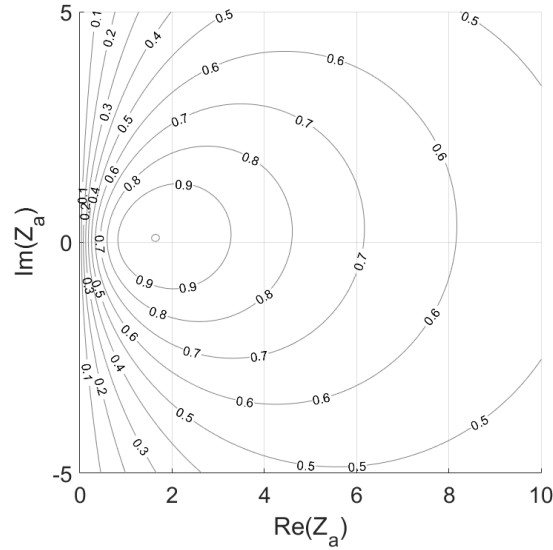


Figure 1 – Iso-absorption coefficient for $ke = 60$ according to Eq. (1)

In 2013, Jeong (8) proposed methods to retrieve the surface impedances of porous absorbers with rigid and air cavity backings as well as fabrics with air cavities. His methods were based on Miki's model and the determination of the flow resistances of the absorbers by solving an optimisation problem, which showed a good agreement in terms of absorption coefficient. They were later applied to measurement data from a round robin experiment (9,10), resulting in a reduction of the standard deviation in absorption coefficient (11).

2.3 Absorber test cases

Impedance models have been suggested for various materials commonly encountered in room acoustics. Porous absorbers have been described with empirical models for many years, and in this study the model presented by Miki (12) is considered. In the case of porous absorbers backed by an air cavity, a multilayered absorber model is applied (13). Three test cases are modelled with the following values for flow resistivity, thickness and cavity depth: $(\sigma, h, d) = (10, 50, 0), (30, 150, 0), (10, 50, 150)$ in $(\text{kPa.s.m}^{-2}, \text{mm}, \text{mm})$. These absorbers are later called 'Soft porous', 'Hard porous', and 'Porous with cavity'.

When a porous absorber is covered with a tight membrane, may it be fabric or a thin hard material, the mass and resistance of the membrane affect the surface impedance as explained by Cox and D'Antonio (13). Values for the quantities governing the membrane absorber are estimated to represent an aluminum plate covering a cavity filled with a porous material. The thickness of the plate is set to 5 mm and the cavity depth to 100 mm. The flow resistivity of the porous filling is 75 kPa.s.m^{-2} , and the density and resistance of the aluminum plate are respectively 2700 kg.m^{-3} and $500 \rho_0 c_0$.

Resonance absorbers (14) are commonly encountered as perforated panels in front of a porous material backed by an air cavity (15). Let us consider a 16-mm-thick panel with a perforation radius of 4 mm, and a perforation rate of 20%. The thickness of the porous material is 40 mm and the depth of the air cavity is 160 mm.

Microperforated panel absorbers have been described by Maa in 1998 (16). The test case for this type of absorbers is given dimensions commonly found in commercial products: the panel thickness is 1 mm, the tube radius is 0.05 mm, the perforation rate is 3%, and the cavity depth is 20 mm.

These different material models are taken as references to validate the impedances retrieved with the method presented in this paper. The surface impedances of the test cases are shown in Figure 2, where clear differences appear between the types of absorbers. The surface impedances of the membrane absorber and the microperforated panel lie where resistance is greater than the point of maximum absorption coefficient. The surface reactance of the membrane absorber is also always positive, with the surface impedance following the curve of an isoline at high frequencies. In the case of the microperforated panel, the surface reactance is negative at low frequencies but increases to positive values with frequency. Regarding the porous absorbers and the perforated panel, their surface impedances lie near the point of maximum absorption coefficient, sometimes with greater values and sometimes with lower values for their resistances and reactances. The effect of the air cavity can be

easily seen with the loops observed in the curves for the porous absorber with cavity and the perforated panel.

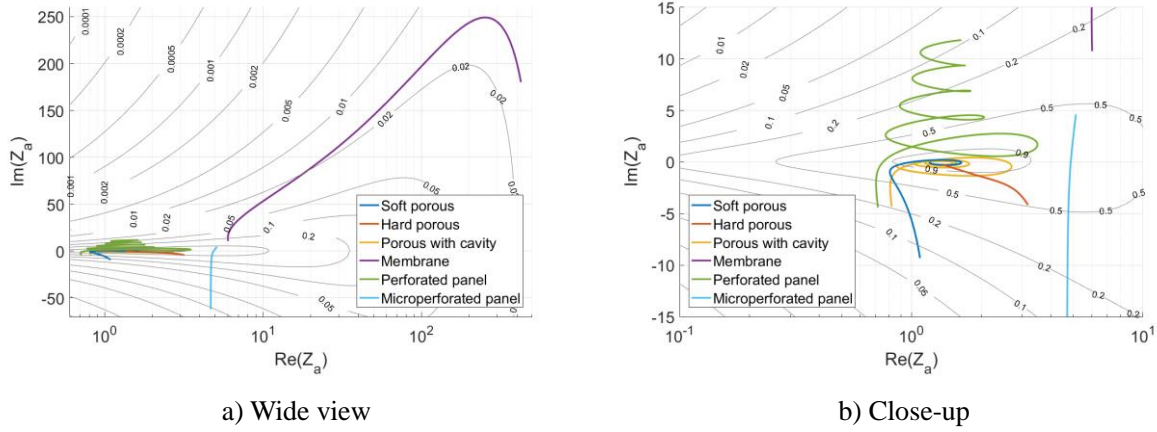


Figure 2 – Surface impedances of the test cases

3. IMPEDANCE RETRIEVAL METHOD

3.1 Possible general impedance models

In order to represent the different surface materials encountered in room acoustics, several models have been considered as general impedance models, with different levels of complexity. Local reaction is assumed, meaning that the surface impedance is constant over the surface of the sample and over the incidence angles. The models are of two types: a constant term to which are added fractional terms, or a spring-mass-damper model to which are also added fractional terms. The different models are displayed in Table 1. All the parameters are set constant, with $R, M, K, A, B, G \geq 0$, $0 \leq \alpha, \beta \leq 1$, and $-1 \leq \gamma \leq 1$. A fractional derivative (positive γ) or integral (negative γ) can be written

$$(j\omega)^\gamma = \cos(\gamma\pi/2)\omega^\gamma + j \sin(\gamma\pi/2)\omega^\gamma. \quad (6)$$

R, M and K represent the classical resistance, mass and stiffness terms, whereas A and B correspond to intermediate behaviours between them, typically found in porous and elastic materials, respectively. They indeed consist of a real and an imaginary part; hence, they contribute to both the resistance and the reactance of the surface impedance. Especially, they allow the real part of the surface impedance to be frequency dependent. Finally, G is equivalent to either A or B depending on the sign of γ .

Table 1 – Possible general models for surface impedance

Parameters	Name	Formula	
3	RMK	$Z_a(\omega) = K \cdot (j\omega)^{-1} + R + M \cdot (j\omega)^1$	(7)
	R+1	$Z_a(\omega) = R + G \cdot (j\omega)^\gamma$	(8)
5	RMK+1	$Z_a(\omega) = K \cdot (j\omega)^{-1} + R + G \cdot (j\omega)^\gamma + M \cdot (j\omega)^1$	(9)
	R+2	$Z_a(\omega) = A \cdot (j\omega)^{-\alpha} + R + B \cdot (j\omega)^\beta$	(10)
7	RMK+2	$Z_a(\omega) = K \cdot (j\omega)^{-1} + A \cdot (j\omega)^{-\alpha} + R + B \cdot (j\omega)^\beta + M(j\omega)^1$	(11)
	R+3	$Z_a(\omega) = A \cdot (j\omega)^{-\alpha} + R + G \cdot (j\omega)^\gamma + B \cdot (j\omega)^\beta$	(12)

3.2 Optimisation problem for direct impedance solving

The first step to find a general impedance model is to ensure that the models proposed in Table 1 are capable of representing the surface impedances of a broad range of typical building materials. This is performed through direct impedance solving: after creating an input impedance for each of the test cases described previously, the parameters of the possible general models are determined by minimizing the L2-norm between the input and output impedances. The cost function to be minimized is

$$F_Z = \sum_i \|Z_{in}(f_i) - Z_a(f_i)\|_2^2, \quad (13)$$

where Z_{in} and Z_a are respectively the input and modelled impedances, and f_i are the centre frequencies of the 1/3-octave bands between 100 Hz and 5000 Hz. No constraints are applied to this optimisation problem, and MATLAB solver *fmincon* is used to handle the problem. When the test case chosen for optimisation is extendedly reacting, the input impedance is taken equal to the surface impedance for an incidence angle of $\pi/4$, as an approximation of the surface impedance under diffuse incidence (17). The starting point of the optimisation is chosen near to the point of maximal absorption coefficient, i.e. $Z_{start}(f_i) = 1.6$.

The goodness of the fit for the optimal impedances to the input impedances is then assessed with the adjusted R^2 . This quantity allows to take into account the number of parameters and indicates whether or not additional parameters bring new information to the model. It is calculated from the R^2 value as follows:

$$R_{adj}^2 = 1 - \frac{(1 - R^2)(n - 1)}{n - q - 1}, \quad (14)$$

where n is the number of data points, and q is the number of parameters in the model excluding the constant term. The formula for R^2 makes use of the residual and total sums of squares:

$$SS_{res} = \|f_{ref} - f_{model}\|_2^2, \quad (15)$$

$$SS_{tot} = \|f_{ref} - \overline{f_{ref}}\|_2^2, \quad (16)$$

$$R^2 = 1 - \frac{SS_{res}}{SS_{tot}} = 1 - \frac{MSE}{V_{ref}}. \quad (17)$$

f_{ref} represents the reference data points, i.e. the input impedance in the present case, $\overline{f_{ref}}$ is its mean, and f_{model} corresponds to the fitted data points. The ratio between the residual and total sums of squares can also be seen as the ratio between the mean square error MSE of the model to the reference and the variance of the reference V_{ref} .

3.3 Optimisation problem for absorption solving

The objective of the present impedance retrieval method is to convert absorption coefficients to surface impedances. Commonly available data for room acoustics materials is the statistical absorption coefficient in octave bands from 125 Hz to 4000 Hz; this is therefore taken as input data to the optimisation problem. The strategy to retrieve the surface impedance is to minimize the difference between the input and the absorption coefficient corresponding to the retrieved impedance. Some constraints are applied to the optimisation in order to ensure that the right impedance is retrieved.

First, general constraints corresponding to the requirements for a physical impedance are set. The retrieved impedance is constrained to have a positive real part as in Eq. (3), while Eq. (4,5) are automatically satisfied with the functions chosen for the models.

Moreover, if the input absorption coefficient is greater than 0.01 in all octave bands, the search range for the impedance is limited to a real part between $0.002\rho_0c_0$ and $1600\rho_0c_0$, and an imaginary part between $-800\rho_0c_0$ and $800\rho_0c_0$; these values correspond to absorption coefficients greater than 0.005.

Besides, some constraints may be applied according to the different absorbers. On one hand, absorbers are considered to be soft when the real part of their surface impedance is close to or lower than that of air. On the other hand, absorbers are considered to be hard when their surface resistance is greater than that of air. Translated into constraints, the resistances of soft and hard materials are forced to be lower than $2\rho_0c_0$ and greater than $1\rho_0c_0$, respectively. The region where the resistance is comprised between $1\rho_0c_0$ and $2\rho_0c_0$ is purposely shared by both absorber types as it coincides with the values yielding the maximal absorption coefficients. Finally, additional constraints are applied in the case of porous materials: the imaginary part of the impedance must be negative, and the real part must be lower than $2\rho_0c_0$ for 2000 Hz and 4000 Hz octave bands.

The whole optimisation problem can be summarized as follows:

$$\min F = \sum_{oct} \|\alpha_{in}(f_{oct}) - \alpha_s(f_{oct})\|_2^2; \quad (18)$$

$$\text{Re}(Z_a(f_i)) \geq 0; \quad (19)$$

$$\text{if } \alpha_{in}(f_{oct}) \geq 0.01 \text{ for all } f_{oct} \quad 0.002 \leq \text{Re}(Z_a(f_i)) \leq 1600, \quad (20)$$

$$-800 \leq \text{Im}(Z_a(f_i)) \leq 800 ; \quad (21)$$

$$\text{Re}(Z_a(f_i)) \geq 1 \text{ or } \text{Re}(Z_a(f_i)) \leq 2 ; \quad (22)$$

$$\text{porous absorbers: } \text{Im}(Z_a(f_i)) \leq 0 , \quad (23)$$

$$\text{Re}(Z_a(f_i)) \leq 2 \text{ for } 1600 \text{ Hz} \leq f_i \leq 5000 \text{ Hz} . \quad (24)$$

In these equations, F is the cost function, a_{in} is the input absorption coefficient, a_s is the statistical absorption coefficient obtained from the retrieved impedance, f_{oct} represents the octave bands between 125 Hz and 4000 Hz, Z_a is the retrieved impedance, and f_i corresponds to the centre frequencies of the 1/3-octave bands between 100 Hz and 5000 Hz. The choice of the constraint in Eq. (22) depends on the absorber under consideration. From Figure 2, it can be inferred that the hardness constraint $\text{Re}(Z_a(f_i)) \geq 1$ is to be applied to membrane absorbers and microperforated panels, as well as high flow resistivity and thick porous absorbers. Inversely, the softness constraint $\text{Re}(Z_a(f_i)) \leq 2$ should be applied to perforated panels and thin porous absorbers with low flow resistivity. The starting point of the optimisation is identical to direct impedance solving with $Z_{start}(f_i) = 1.6$. The solutions found by the algorithm are considered valid under one condition:

$$F \leq 0.015 \text{ if } a_{in}(f_{oct}) \leq 1 \text{ for all } f_{oct} , \quad (25)$$

$$F \leq 0.25 \text{ otherwise} , \quad (26)$$

which is respectively equivalent to a root-mean-square error of 0.05 and around 0.2 between the input and retrieved absorption coefficients. Cases where the input absorption coefficient is greater than 1 are allowed a larger error because the general models proposed tend to yield values that exceed 1 to a lesser extent than what can be observed in measurements.

4. CONVERSION OF ABSORPTION COEFFICIENTS

4.1 Model selection

The method for direct impedance solving is applied to the test cases given in Section 2.3 with all the possible general models, in order to evaluate how well they can represent the different types of absorbers. The results of the optimisations are gathered in Table 2. It can first be seen that the RMK model performs poorly at reproducing the surface impedance of the membrane absorber, the adjusted R^2 value being even negative. This is not surprising because RMK only presents constant resistances, while the surface resistance of the membrane varies greatly as was seen in Figure 2. The fit of RMK to the surface impedance of the hard porous case is also significantly lower than that of the other models. The same observation can be made for the R+1 model with the perforated panel absorber. These two models can thus be considered inappropriate for a general impedance model. Among the four remaining models, the highest value of adjusted R^2 is found for either the RMK+1 or R+2 models in all the test cases except the hard porous absorber. It indicates that the extra parameters included in the RMK+2 and R+3 models do not bring new information. In addition, the adjusted R^2 values obtained with the RMK+1 and R+2 models are very close if not equal. Therefore, the two models with 5 parameters, RMK+1 and R+2, are the most efficient at representing the surface impedances of various common sound absorbers. Nevertheless, the results presented here do not allow to choose one model over the other; consequently, the two models are selected and their performances will be compared in the later sections.

Table 2 – Adjusted R^2 between input and retrieved impedances

Absorber	RMK	R+1	RMK+1	R+2	RMK+2	R+3
Soft porous	0.9813	0.9782	0.9863	0.9885	0.9864	0.9864
Hard porous	0.6323	0.9925	0.9962	0.9907	0.9971	0.9971
Porous with cavity	0.7256	0.7237	0.7274	0.7274	0.6778	0.6778
Membrane	-0.0709	0.7510	0.7202	0.7202	0.6693	0.6605
Perforated panel	0.9468	0.7872	0.9472	0.9417	0.9376	0.9376
Microperforated panel	0.9999	0.9845	0.9999	0.9999	0.9999	0.9999

Although similar in some aspects, the RMK+1 and R+2 models differ in their physical

interpretation. On one hand, the four terms in the RMK+1 model represent the classical spring-mass-damper system to which either an elastic or a porous behaviour is added. On the other hand, the R+2 model can be seen as a generalization of the RMK model where the fractional terms describe the intermediate behaviours between pure resistance and pure mass or stiffness. The spring-mass-damper system is still included in this model as the extreme case $\alpha = \beta = 1$.

4.2 Performance of the retrieval method

The RMK+1 and R+2 models were showed to be the most efficient general impedance models. However, the goal of this study is to retrieve surface impedances from statistical absorption coefficients. Therefore, the absorption solving method is applied to the same test cases as previously with the two selected models. From the results displayed in Table 3, a very poor fit can be observed for the membrane absorber with both general models. It is mostly due to the behaviour of the membrane input model: at high frequencies, the surface impedance follows the curve of an absorption coefficient isoline (cf. Figure 2). On the contrary, the general models can only yield monotonically increasing reactances, which results in absorption coefficients that keep decreasing at high frequencies. Considering the difficulty to describe membrane absorbers, it is likely that inaccuracies are present in the general and input models. When looking at the other absorbers, it is found that the RMK+1 model performs better for the hard porous absorber and the perforated panel, while the R+2 model shows a better fit with the soft porous absorber. The two models exhibit equivalent performances in the cases of the porous absorber with cavity and the microperforated panel. Overall, the RMK+1 model appears more advantageous than the R+2 model with theoretical input data. In practical applications though, input data consist in measurement results which are affected by noise from various origins. The retrieval method should thus be confronted to measured input data to confirm its validity.

Table 3 – R^2 between input and retrieved impedances

Absorber	RMK+1	R+2
Soft porous	0.6750	0.7814
Hard porous	0.9649	0.8581
Porous with cavity	0.7324	0.7324
Membrane	-1.1286	-1.1283
Perforated panel	0.8432	0.7918
Microperforated panel	0.6247	0.6258

4.3 Impedance retrieval from measured data

In 2009 Tompson and Vercammen led a round robin study on reverberation chambers (9,10). The statistical absorption coefficients of four different samples were measured in 13 laboratories in Europe. The results of this study are taken as input to the retrieval method to assess its sensitivity to the noise and deviations that exist in real measurements. The first sample in the study is a foam material with a flow resistivity estimated to $\sigma \cong 50 \text{ kPa.s.m}^{-2}$ and a thickness $h = 25 \text{ mm}$, to which the hardness constraint is applied for the optimisation. Another porous material was included in the study with a mineral wool sample whose flow resistivity is $\sigma = 19.8 \text{ kPa.s.m}^{-2}$ and thickness $h = 100 \text{ mm}$, categorized as a soft material for the optimisation. The third sample is a membrane absorber consisting of the same mineral wool as the second sample with a 5-mm thick hardboard cover. Finally, the fourth sample is a combination of the previous membrane and mineral wool absorbers, with units arranged in a chessboard pattern. 13 surface impedances are retrieved for each sample, corresponding to the 13 input absorption coefficients.

The normalized standard deviations (STDn) are then compared between the input absorption coefficients and the retrieved absorption coefficients, as shown in Figure 3. The first observation is that the two general impedance models often return similar results. For the two porous absorbers, it can be seen that the absorption coefficients retrieved with RMK+1 and R+2 have lower STDn than the ones measured at almost all frequencies. Only the foam absorber around 250 Hz does not follow this trend. Concerning the combined absorber, the STDn of the retrieved absorption coefficients are very similar to that of the measured ones. The membrane absorber is the only case where significant differences

appear between the two impedance models. Below 400 Hz, both the models and the measured data lead to close STDn. Above 400 Hz, however, the RMK+1 model yields a higher STDn than the measurements, whereas the R+2 model exhibit values close to the measured data and even lower values in the highest octave band.

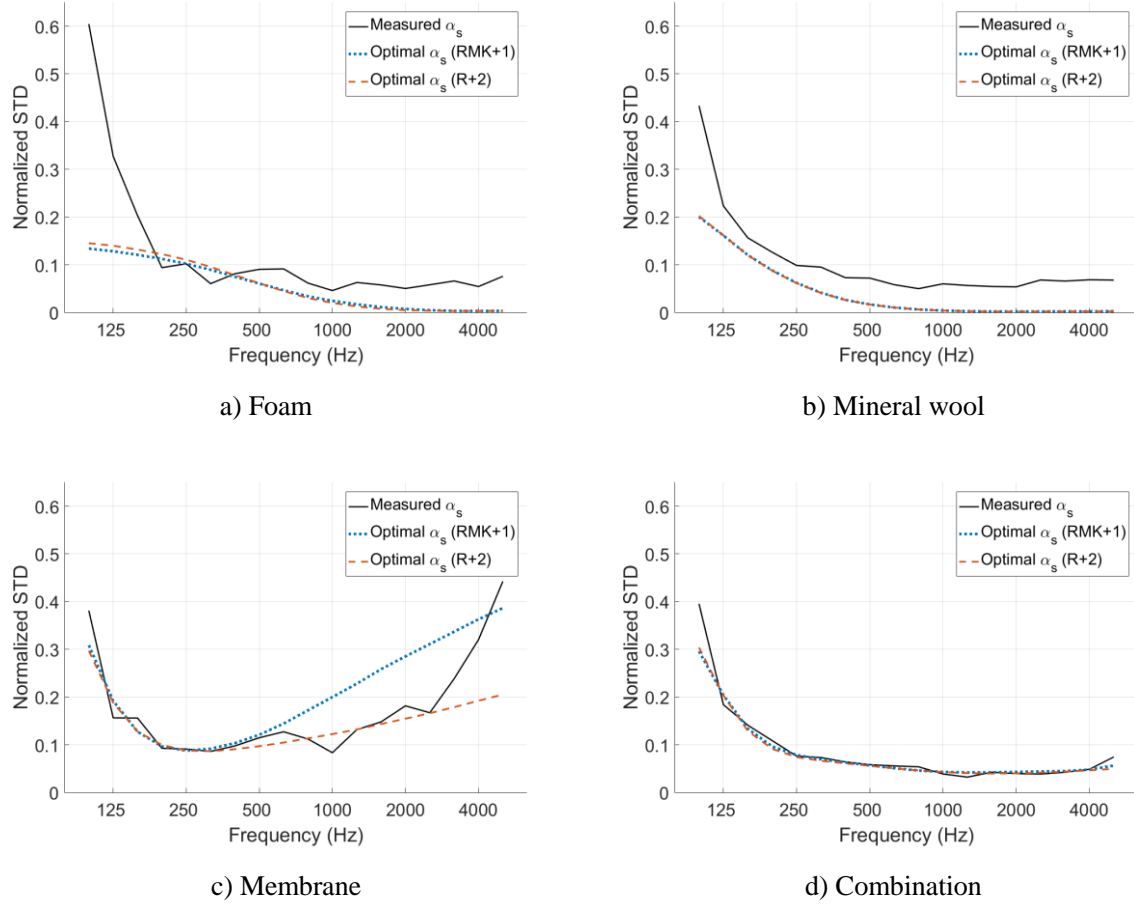
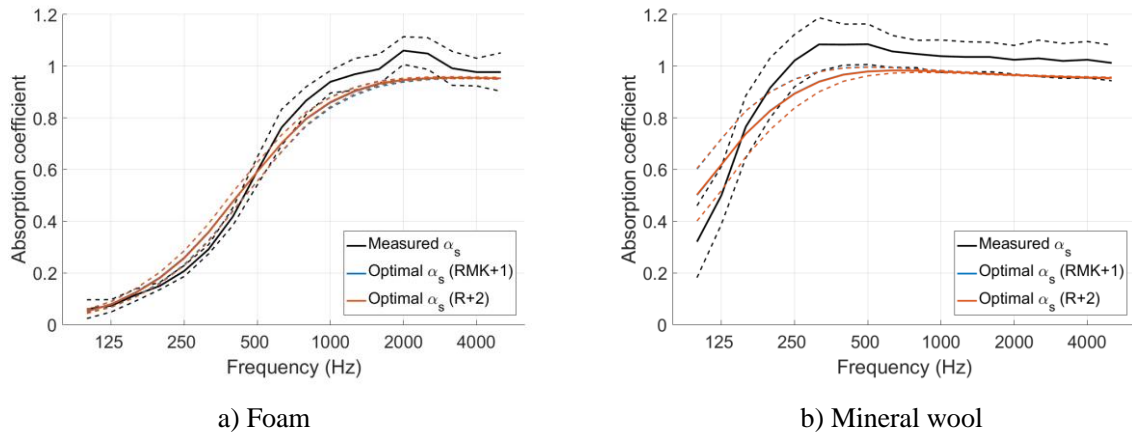


Figure 3 – Normalized standard deviations of input and retrieved absorption coefficients

Another illustration of these results is displayed in Figure 4, where the standard deviations are represented as ranges in dashed lines along the means of the absorption coefficients in solid lines. The curves corresponding to RMK+1 and R+2 almost always overlap, the only discrepancies appearing in the membrane absorber case and especially at high frequencies. Besides, the retrieved impedances tend to yield lower values of absorption coefficient than the measurements. This is seen with the foam absorber above 500 Hz, with the mineral wool above 160 Hz, and with the membrane absorber above 1600 Hz. The combined absorber is the only case where the results of the retrieval method are similar to the results of the measurements, both in terms of mean value and standard deviation.



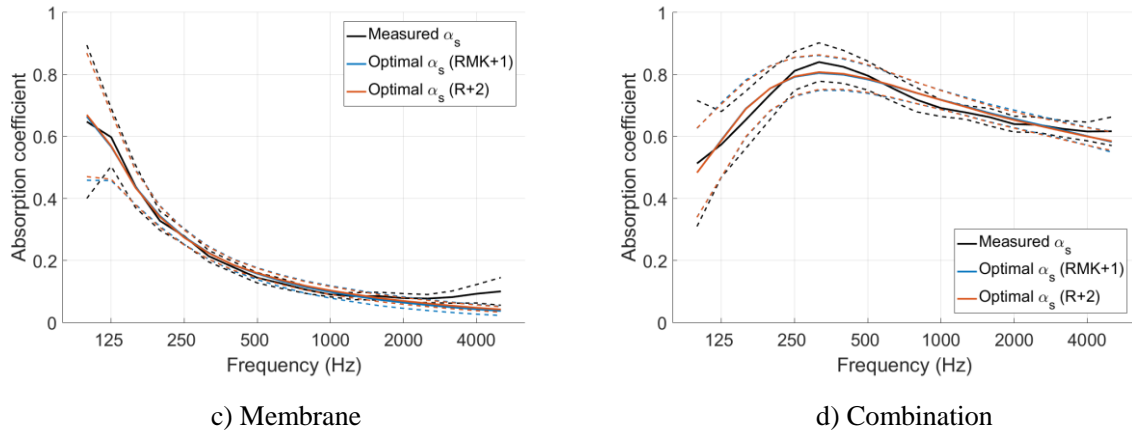


Figure 4 – Absorption coefficients of the different samples. Dashed lines: ± 1 STD

5. DISCUSSION

The general impedance models presented in this paper are based on fractional calculus. The formulas of these models all imply that the imaginary part of the surface impedance is monotonically increasing. While this is a fair assumption in most cases, the theoretical models for the impedances of porous absorbers with cavities and membrane absorbers describe otherwise. Consequently, the performance to retrieve the impedances of such absorbers is limited, as seen already in Table 2 with direct impedance solving. It can lead to even greater discrepancies in absorption solving; it was for example the case with the membrane absorber in Table 3. As a result, the method presented should be applied with caution when retrieving the impedances of these absorbers, whichever general model is selected.

The results of impedance retrieval showed close results between the two models selected in section 4.1. The RMK+1 and R+2 are indeed similar mathematically, even though their physical interpretations differ. From the impedances retrieved in this paper, the R+2 model seems to yield more robust results than the RMK+1 when input data are based on measurements. However, the discrepancies observed are not large enough to completely discard the RMK+1 model, and further investigation is required. It is expected that a stability analysis and the study of transformation to the time domain will bring new clues to decide which of the models is best suited for surface impedance retrieval from statistical absorption coefficients.

One issue not addressed here is the amount of prior information about the sound absorber under study. It is critical to know the type of absorber in order to apply the right constraints, especially for porous absorbers. These absorbers indeed require more specific and restricting constraints than the others. A possible solution would be to implement an automatic material detection with machine-learning: based on the input absorption coefficient, the type of sound absorber would be deduced and the corresponding constraints applied. However, it would require a large amount of training data, which is not necessarily available for all types of sound absorber. Naturally, training data could be created from the theoretical models, but it would not cover all the phenomena taking place in measurements.

6. CONCLUSION

This paper presented a method to retrieve the surface impedances of various sound absorbers from their statistical absorption coefficients. After suggesting several general impedance models based on fractional calculus, a first optimisation problem was set to minimize the difference between those general impedance models and the theoretical impedance models of sound absorber test cases. It was demonstrated that a general surface impedance model could be most efficiently expressed with five parameters. Two general models were thus selected for further study: the RMK+1 and R+2 models. Theoretical absorption coefficients were then calculated, and the parameters of the two models were determined with a second optimisation problem. A good agreement was found between the original surface impedances and those retrieved with RMK+1 and R+2; the only exception was the case of a membrane absorber. The impedance retrieval method was finally applied to the results of a round robin

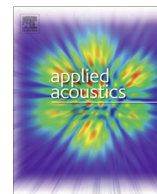
experiment where the absorption coefficients of four sound absorbers were measured in 13 different reverberation chambers. By retrieving the corresponding surface impedances, it was shown that the absorption coefficients obtained with the R+2 model always had similar or lower standard deviations than the ones measured in the laboratories, even in the case of the membrane absorber. Therefore, the impedance retrieval method presented with the R+2 model appeared to be robust to noisy input data, i.e. to deviations in measured absorption coefficients. Despite these promising results, further investigation is required to confirm the validity of this method, especially with a stability analysis of the optimisation problem. A transformation of the retrieved surface impedances to the time domain will also be implemented for later applications in numerical simulations for room acoustics.

REFERENCES

1. ISO 10534:1998. Acoustics - Determination of sound absorption coefficient and impedance in impedance tubes. International Organization for Standardization. Geneva, Switzerland 1998.
2. Thomasson S-I. Theory and experiments on the sound absorption as function of the area. Report No. TRITA-TAK-8201. Department of Technical Acoustics, Royal Institute of Technology. Stockholm, Sweden 1982.
3. Rindel JH. Modelling the angle-dependent pressure reflection factor. *Applied Acoustics*. 1993;38:223-234.
4. Davy JL, Lerner DJ, Wareing RR, Pearse JR. The average specific forced radiation wave impedance of a finite rectangular panel. *J. Acoust. Soc. Am.* 2014;136(2):525-536.
5. ISO 354:2003. Acoustics - Measurement of sound absorption in a reverberation room. International Organization for Standardization. Geneva, Switzerland 2003.
6. Rienstra SW. Impedance models in time domain. Messiaen - Project AST3-CT-2003-502938. Deliverable 3.5.1 of Task 3.5. 2005.
7. Rindel JH. An impedance model for estimating the complex reflection factor. *Forum Acusticum* 2011; 27 June - 1 July 2011; Aalborg, Denmark 2001. CD-ROM.
8. Jeong C-H. Converting Sabine absorption coefficients to random incidence absorption coefficients. *J. Acoust. Soc. Am.* 2013;133(6):3951-3962.
9. Tompson D, Vercammen M. Research for investigation of absorption measurement deviation. Report No. RA 547-1-BR. Laboratory for Acoustics, Peutz BV. Molenhoek, Netherlands 2009
10. Vercammen M. Improving the accuracy of sound absorption measurement according to ISO 354. ISRA 2010; 29-31 August 2011; Melbourne, Australia 2010. CD-ROM.
11. Jeong C-H, Chang J-H. Reproducibility of the random incidence absorption coefficient converted from the Sabine absorption coefficient. *Acta Acustica united with Acustica*. 2015;101:99-112.
12. Miki Y. Acoustical properties of porous materials - Modifications of Delany-Bazley models. *J. Acous. Soc. Jpn.* 1990;11(1):19-24.
13. Cox TJ, D'Antonio P. Porous absorption. In: Cox TJ, D'Antonio P. *Acoustic Absorbers and Diffusers: theory, design, and application*. 2nd ed. London, UK, and New York, USA: Taylor & Francis; 2009. p. 156-195.
14. Ingard U. On the theory and design of acoustic resonators. *J. Acoust. Soc. Am.* 1953;25(6):1037-1061
15. Attenborough K, Vér IL. Sound absorbing materials and sound absorbers. In: Vér IL, Beranek LL. *Noise and Vibration Control Engineering*. 2nd ed. New York, USA: John Wiley & Sons; 2006. p. 215-277
16. Maa DY. Potential of microperforated panel absorber. *J. Acoust. Soc. Am.* 1998;104(5):2861-2866.
17. Jeong C-H, Brunskog J. The equivalent incidence angle for porous absorbers backed by a hard surface. *J. Acoust. Soc. Am.* 2013;134(6):4590-4598.

APPENDIX B

From absorption to
impedance: Enhancing
boundary conditions in
room acoustic conditions



From absorption to impedance: Enhancing boundary conditions in room acoustic simulations[☆]

Boris Mondet^{a,b,*}, Jonas Brunskog^a, Cheol-Ho Jeong^a, Jens Holger Rindel^b

^aAcoustic Technology, DTU Electrical Engineering, Technical University of Denmark, Denmark

^bOdeon A/S, DTU Science Park, Denmark

ARTICLE INFO

Article history:

Received 25 October 2018

Received in revised form 25 April 2019

Accepted 26 April 2019

Available online 27 August 2019

Keywords:

Inverse problem

Surface impedance

Absorption coefficient

Room acoustics

ABSTRACT

In room acoustic simulations the surface materials are commonly represented with energy parameters, such as the absorption and scattering coefficients, which do not carry phase information. This paper presents a method to transform statistical absorption coefficients into complex surface impedances which are needed for phased or time-domain calculation methods. Two 5-parameter impedance models based on fractional calculus are suggested to achieve a general model for common acoustic materials, thereby ensuring that the impedance found has a physical meaning. The five parameters for the general models are determined by solving an inverse problem with an optimization method. Due to the non-uniqueness of retrieving complex-valued impedances from real-valued absorption coefficients, prior information about the absorber of interest can be used as constraints, which is shown to help determine the impedance more correctly. Known material models, such as Miki's and Maa's models, are taken as references to assess the validity of the suggested model. Further stability and sensitivity investigations indicate that the method presented constitutes an efficient solution to convert sound absorption coefficients back to their original complex surface impedances.

© 2019 Elsevier Ltd. All rights reserved.

1. Introduction

The simulation of room acoustics is an essential tool in the architectural design of various spaces. Concert halls have been at the heart of the development of this tool due to the utmost demand of acoustics in music listening conditions. Therefore, common simulation software are well suited to large volumes or high frequencies thanks to the principles of geometrical acoustics (GA) [1,2]. An adverse effect of this development is inaccuracies at low frequencies. It is especially true in rooms with small volumes, e.g. classrooms and meeting rooms [3], where the acoustic properties are also critical. The GA simulation methods developed are indeed typically based on a statistical description of the sound field with energy parameters. Consequently, boundaries are represented with absorption and scattering coefficients, whereas phase information that governs modal behaviour is necessary for accurate predictions at low frequencies. Solutions have been proposed, such as phased geometrical acoustics [4–8] and numerical wave-based methods [9–11], and they are currently under ongoing study

for their application to room acoustics. The former relies on the same principles as geometrical acoustics but includes phased reflections at the boundaries, while the latter directly solve the wave equation with numerical discretization and thus inherently carry phase information. Besides considerations of computation time and accuracy, another challenge these methods face is the lack of reliable boundary conditions. In order to accurately predict wave reflections, phased parameters are required to represent the boundary conditions, such as the surface impedance or the pressure reflection coefficient [6,12]. The problem lies in the availability of measured data for these quantities, which is restricted by experimental limitations and communication by manufacturers. Indeed, manufacturers of sound absorbers only provide information on the absorption coefficients of their products, usually measured in reverberation chambers according to ISO 354 [13], which suffers a serious reproducibility issue [14]. This paper proposes a robust method to inversely determine surface impedances of common building materials from their statistical absorption coefficients.

A few authors have attempted to retrieve surface impedances from absorption coefficients. Rindel used a resonant system to model the surface impedances of sound absorbers [15]. He notably pointed out the non-uniqueness of solutions when transforming an absorption coefficient into surface impedance. He dealt with this

[☆] Some results included in this paper have been presented in Internoise 2017, Hong Kong.

* Corresponding author.

E-mail address: bojmo@elektro.dtu.dk (B. Mondet).

by distinguishing between soft and hard surfaces, a strategy also used in the present paper. Since the absorption coefficient is an energy parameter, there is an infinite number of complex surface impedances corresponding to any value it can take. Therefore, extra information is needed in addition to the absorption coefficient to retrieve the right impedance, such as the frequency dependence of the impedance with physically inspired models and other constraints. However, Rindel's study only took into consideration three types of sound absorbers, namely porous absorbers, membranes, and resonators, thus leaving out other building materials. Jeong proposed methods to retrieve the surface impedances of porous absorbers with rigid and air cavity backings as well as fabrics with air cavities [16]. His methods were based on Miki's model and the determination of the flow resistances of the absorbers by solving an optimization problem, which showed a good agreement in terms of absorption coefficient. They were later applied to measurement data from a round robin experiment [14], resulting in a reduction of the standard deviation in the random incidence absorption coefficient calculated from the retrieved surface impedance [17]. Despite the inclusion of absorbers with air cavities, the impedance retrieval presented in this case is limited to porous materials. Consequently, there is still a need for a more general impedance retrieval method that would encompass a wide range of different materials found in real rooms.

The current paper is a continuation of the work presented in [18]. Its organization is as follows: the theory about surface impedance is first given in chapter 2 with requirements on its physical feasibility, its relation with the absorption coefficient, and several models corresponding to different sound absorbers. In chapter 3, two models of surface impedance are presented, the optimization problem to be solved is described with its associated constraints, and some theoretical test cases are introduced as references. Chapter 4 compares the results between theoretical and retrieved impedances, and analyzes the stability and sensitivity of the solution found via the optimization problem. Lastly, the results are further discussed in chapter 5, justifying the choice of one general model for surface impedance, assessing the validity of the retrieval method despite a few limitations, and foreseeing potential applications in room acoustic simulation.

2. Theory on surface impedance

Unless specifically stated otherwise, all the impedances mentioned thereafter are normalized by the characteristic impedance of air $\rho_0 c_0$.

2.1. Boundary representation

The surface impedance Z_a is a complex-valued parameter that describes the relation between the sound pressure p and the normal particle velocity v_n at a boundary ∂V [19]:

$$Z_a = \frac{1}{\rho_0 c_0} \frac{p}{v_n} \Big|_{\partial V}. \quad (1)$$

It is a function of frequency, the position on the boundary, and the incidence angle of the sound wave. Its real part is called the resistance, while its imaginary part is called the reactance.

The boundary properties for room acoustic simulations must be physically feasible, which leads to three requirements on the surface impedance. A boundary must be a passive system as it does not give any energy to the sound field. A boundary must also be a causal system so that the causes always precede the consequences they bring about. Lastly, the sound pressure and particle velocity in time domain are real-valued signals; therefore, when represented in the time domain, the surface impedance function must also take real values. Using the $e^{i\omega t}$ time convention, these

three requirements can be translated into mathematical expressions involving the surface impedance in the frequency domain [20]. Passivity, causality, and real values in the time domain are respectively expressed as:

$$\operatorname{Re}\{Z_a(\omega)\} \geq 0 \quad \text{for all } \omega \in \mathbb{R}; \quad (2)$$

$$Z_a(\omega) \quad \text{analytic for } \operatorname{Im}\{\omega\} < 0; \quad (3)$$

$$Z_a^*(\omega) = Z_a(-\omega). \quad (4)$$

Note that the complex angular frequencies ω appearing here are due to the mathematical transformation of the requirements defined in the time domain to the frequency domain. In the case of causality in Eq. (3), the time-domain impedance corresponds to an impulse response and must be equal to zero for any time $t < 0$. This can only be respected by introducing complex ω in the frequency domain.

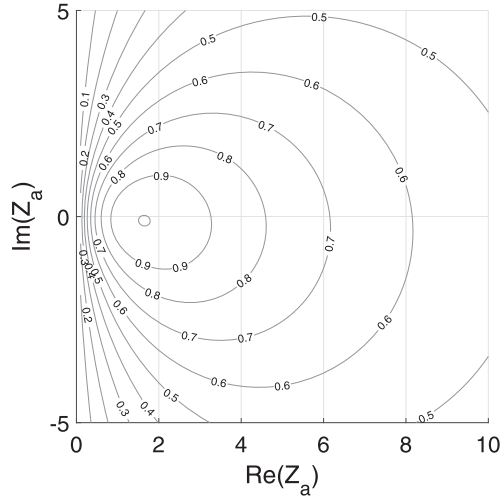
Besides these requirements, the surface impedance is related to the absorption coefficient, the most widely available parameter to describe materials in room acoustics. This parameter is regarded to be measured in reverberation chambers according to the international standard ISO 354 [13], resulting in the Sabine absorption coefficient. It corresponds to the statistical absorption coefficient as defined by Thomasson [21,22]:

$$\alpha_s = 8 \int_0^{\pi/2} \frac{\operatorname{Re}\{Z_a(\theta)\} \sin \theta}{|Z_a(\theta) + Z_r(\theta)|^2} d\theta \quad (5)$$

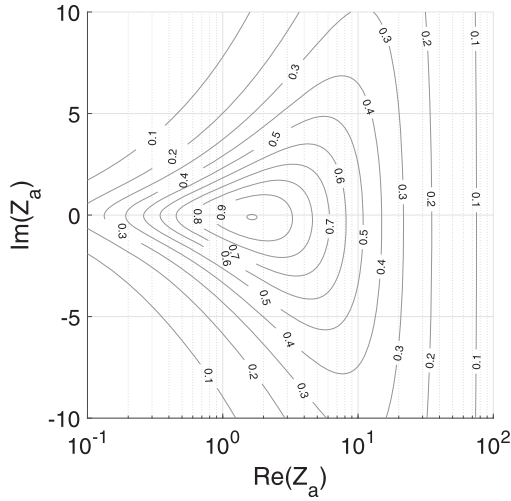
with θ the incidence angle of the sound wave and Z_r the radiation impedance of the sample under study. It is obtained from the ratio between the absorbed power and the projected incident power on a finite sample, averaged over all angles assuming a diffuse sound field. In the case of a locally reacting model for the surface impedance the equation can be used without any dependence of Z_a on θ . Contrary to the random incidence absorption coefficient that assumes an infinitely large absorptive surface [19], the statistical absorption coefficient takes into account the size and shape of the absorber sample as well as its influence on the sound field via the radiation impedance.

Unlike the surface impedance, which is the ratio between total sound pressure and particle velocity in the normal direction to a surface, the radiation impedance describes the ratio between radiated sound pressure and normal particle velocity at the boundary [23]. Thomasson [22], Rindel [24], Brunskog [25], and Davy et al. [26] successively proposed formulas for the radiation impedance, with Davy et al. combining Thomasson's theoretical formulas into a unique empirical formula yielding a complex impedance for all frequencies. For a rectangular sample, and assuming that the speed of sound is larger in the material studied than in air, it can be calculated with Eqs. (53)–(63) from reference [26]. In addition to the incidence angle θ , it should be noted that the radiation impedance is also dependent on the size of the sample; for an infinite sample, its value converges to $1/\cos \theta$. This radiation impedance was derived for samples mounted in an infinite baffle, though measurement setups for absorption coefficient typically consist of the absorber simply lying on the ground of the reverberation chamber. For this reason, the thinner a measured absorptive sample is the more accurately Eq. (5) will represent it. The international standard for reverberation chamber measurements [13] recommends relatively square samples with areas between 10 m^2 and 12 m^2 . Therefore, in this study and similarly to [15], an area of 11 m^2 is assumed with a square shape for all samples in order to minimize the potential discrepancies with measured samples which dimensions are unknown.

The corresponding isolines of the statistical absorption coefficient as a function of surface impedance are plotted in Fig. 1 for the frequency 2000 Hz. The highest value of absorption coefficient approximately occurs at $Z_a = 1.6$, with small variations depending



(a) Linear axes.



(b) Logarithmic x-axis.

Fig. 1. Isolines of Eq. (5) at 2000 Hz for a sample of 11 m².

on frequency, as is illustrated. It is also clear that different values of surface impedance can lead to the same statistical absorption coefficient.

2.2. Existing material models

Impedance models have been suggested for various materials commonly encountered in room acoustics. The models selected as references for the present study are presented here; they include porous absorbers with rigid and cavity backings, membrane absorbers, as well as perforated and microperforated panels. For the following, let us consider a two-dimensional space where x represents the normal direction to a boundary and y the parallel direction to it. A plane wave is propagating in air with a wavenumber k such that $k^2 = k_x^2 + k_y^2$. It meets the boundary with an incidence angle θ between its direction of propagation and the normal direction to the boundary. Consequently, the relations $k_x = k \cos \theta$ and $k_y = k \sin \theta$ for the wavenumber exist.

2.2.1. Porous absorbers with rigid backing

For a rigidly-backed absorber whose characteristic impedance is Z_c , thickness is h , and internal wavenumber is k_p with

$k_p^2 = k_{px}^2 + k_{py}^2$, the surface impedance with extended reaction is [27]

$$Z_a(\omega) = -jZ_c \frac{k_p}{k_{px}} \cot(k_{px}h). \quad (6)$$

When local reaction is assumed, the internal wavenumber k_p is equal to the normal component of the wavenumber k_x and the formula simplifies to

$$Z_a(\omega) = -jZ_c \cot(k_x h). \quad (7)$$

Porous absorbers have been described with empirical models for many years, and in this study the model presented by Miki [28] is used. The characteristic impedance Z_c and propagation constant g of a porous material can be written

$$Z_c = 1 + 0.07 \left(\frac{f}{\sigma} \right)^{-0.632} - j0.107 \left(\frac{f}{\sigma} \right)^{-0.632}, \quad (8)$$

$$\frac{g}{k} = 0.160 \left(\frac{f}{\sigma} \right)^{-0.618} + j \left(1 + 0.109 \left(\frac{f}{\sigma} \right)^{-0.618} \right), \quad (9)$$

with σ the flow resistivity of the material and f the frequency. It is interesting to note that these two formulas can be expressed with fractional calculus. For $-1 < \gamma < 1$, a fractional derivative (positive γ) or integral (negative γ) is defined in the frequency domain as [29]

$$(j\omega)^\gamma = \cos(\gamma\pi/2)\omega^\gamma + j \sin(\gamma\pi/2)\omega^\gamma. \quad (10)$$

The characteristic impedance and propagation constant then become

$$Z_c = 1 + 0.409 \left(\frac{j\omega}{\sigma} \right)^{-0.632}, \quad (11)$$

$$\frac{g}{jk} = 1 + 0.602 \left(\frac{j\omega}{\sigma} \right)^{-0.618}. \quad (12)$$

From these quantities, the surface impedance is determined by following Eq. (6) for extended reaction with $k_p = \frac{g}{j}$.

2.2.2. Porous absorbers with an air cavity

In the case of porous absorbers backed by an air cavity a multi-layered absorber model is applied [30]. Let us consider a visible material with a thickness h , a characteristic impedance Z_c , and a wavenumber k_p with $k_p^2 = k_{px}^2 + k_{py}^2$; the cavity behind it has a depth d and a surface impedance Z_d . The surface impedance of the whole system is then calculated as

$$Z_a(\omega) = \frac{-jZ_c Z_d k_p / k_{px} \cot(k_{px}h) + (Z_c k_p / k_{px})^2}{Z_d - jZ_c k_p / k_{px} \cot(k_{px}h)}. \quad (13)$$

An air cavity is most accurately modelled with extended reaction, leading to the impedance

$$Z_d = -j \frac{\cot(kd \cos \theta)}{\cos \theta}. \quad (14)$$

2.2.3. Membrane absorbers

Membrane absorbers are classically modelled as simple resonant systems [19] with damping, mass, and spring terms as follows:

$$\rho_0 c_0 Z_a(\omega) = r_i + j \left(\omega m - \frac{\rho_0 c_0^2}{\omega d} \right). \quad (15)$$

r_i represents the internal resistance of the system, which includes losses in the membrane as well as in the cavity where a porous material is often placed. m is the mass per unit area of the membrane, and d is the depth of the cavity. It is also assumed that the

wavelength of the incident sound is much larger than the depth of the cavity, i.e. $kd \ll 1$. By introducing the loss factor η , the internal resistance can be found as [31]

$$r_i = \eta \omega m. \quad (16)$$

However, it can be considered that this resistance has an influence only around the resonance frequency. Therefore, ω can be substituted with ω_0 in the equation above, leading to a constant r_i . Although widely accepted and used, this resonant system model is still a rather rough approximation and the behaviour of membrane absorbers remains hard to predict.

2.2.4. Perforated panels

The surface impedance of a perforated panel can be seen as the sum of the contributions from its openings and from the cavity behind it [32]. The impedance of the openings is dominated by the mass of air put into motion; for a panel of thickness h with circular openings of radius a , the effective length L_{eff} and the impedance Z_t of a single opening are

$$L_{eff} = h + 1.7a, \quad (17)$$

$$Z_t = \frac{j\omega L_{eff}}{c_0}. \quad (18)$$

The cavity of a perforated panel absorber is normally filled with a porous material, either completely or partially. The cavity impedance Z_{cav} can then be calculated with the corresponding model for porous absorbers. If the cavity is completely filled, Z_{cav} is equal to the surface impedance of a rigidly backed porous absorber, as described in Eq. (6). On the other hand, if the cavity is made of a porous layer backed by air, Z_{cav} is taken as the surface impedance of a porous absorber with an air cavity by following Eq. (13). Averaging the opening impedance over the surface of the panel with the perforation rate p , the total surface impedance of a perforated panel becomes

$$Z_a(\omega) = \frac{Z_t}{p} + Z_{cav}. \quad (19)$$

2.2.5. Microperforated panels

Microperforated panel absorbers have been described by Maa [33]. They are made of a thin panel with thickness h , which is perforated with tubes of radius a at a perforation rate p . The specific impedance of the tubes Z_t and its end correction Z_e can be written

$$\rho_0 c_0 Z_t = \frac{32\mu_0 h}{4a^2} \left(1 + \frac{s^2}{32}\right)^{1/2} + j\omega \rho_0 h \left(1 + \left(9 + \frac{s^2}{2}\right)^{-1/2}\right), \quad (20)$$

$$\rho_0 c_0 Z_e = \left(\frac{\rho_0 \mu_0 \omega}{2}\right)^{1/2} + j1.7\rho_0 \omega a, \quad (21)$$

where μ_0 is the dynamic viscosity of air and s is the perforate constant, given by

$$s^2 = \frac{\rho_0 \omega a^2}{\mu_0}. \quad (22)$$

Adding an air cavity of depth d as a backing, the surface impedance of the microperforated panel absorber is

$$Z_a(\omega) = \frac{Z_t + Z_e}{p} - j \frac{\cot(kd \cos \theta)}{\cos \theta}. \quad (23)$$

These material models give valuable information on the behaviours of the different materials' surface impedances, which will greatly help the retrieval method with constraints for the optimization problem, as described in the following section. The models have also been used to create reference test cases for the validation of the retrieval method.

3. The impedance retrieval method

3.1. General impedance models

Following the requirements described in Section 2.1, a general impedance model that would be able to describe all common sound absorbers is desired. Starting from six models with different numbers of parameters, a preliminary study [18] indicated two eligible models for this role. Both of them consist of five parameters and are based on a modification of the damped oscillator model with the help of fractional calculus. The RMK + 1 model is expressed as

$$Z_a(\omega) = K \cdot (j\omega)^{-1} + R_1 + M \cdot (j\omega)^1 + G \cdot (j\omega)^\gamma, \quad (24)$$

where $R_1, M, K, G \geq 0$ and $-1 \leq \gamma \leq 1$. The first three terms correspond to the classic damped oscillator model, also called RMK, to which a fourth term has been added, equivalent to either a fractional integral or derivative depending on the sign of γ . The second model investigated is the R + 2 model:

$$Z_a(\omega) = A \cdot (j\omega)^{-\alpha} + R_2 + B \cdot (j\omega)^\beta \quad (25)$$

with $R_2, A, B \geq 0$ and $0 \leq \alpha, \beta \leq 1$. The stiffness and mass terms of the damped oscillator model, corresponding to integer integral and derivative respectively, have here been replaced with fractional integral and derivative to obtain a more general model. The fractional integrals and derivatives are powerful terms that allow the resistance to be frequency-dependent in the present case. They appear in Miki's model, as mentioned previously, but also in the description of mechanical properties of elastic materials [34] and in the expression of electric impedances [35] to cite a few examples. It can be easily verified that the models in Eqs. (24) and (25) satisfy the requirements from Eqs. (2)–(4). However, these two surface impedance models do not take into account the incidence angle of the sound wave and therefore assume local reaction, contrary to the theoretical models presented in chapter 2. Besides, it is interesting to note that both models are bound to have a monotonically increasing reactance due to their formulations, which is not the case of all material models presented previously. Varying reactance can for example occur with porous absorbers with and without air cavity due to the \cotan terms in Eqs. (7) and (13), as well as with perforated panels for the same reason.

3.2. Optimization problem

To convert a real-valued function into a complex-valued one, the inverse problem to be solved is ill-posed: there is an infinite number of surface impedances that can match a given absorption coefficient. Consequently, the parameters of the RMK + 1 and R + 2 models are determined by solving a constrained optimization problem. The input data consist of the Sabine absorption coefficient in octave bands between 125 Hz and 4 kHz. At a given evaluation point Z_a , the cost function F is defined as the squared L2-norm between the corresponding statistical absorption coefficient $\alpha_s(Z_a)$ and the input absorption coefficient α_{in} :

$$F(Z_a) = \|\alpha_{in} - \alpha_s(Z_a)\|_2^2. \quad (26)$$

Both absorption coefficients in this equation are expressed in octave bands due to limitations on the input data, with three frequency components per octave band to calculate α_s .

The goal of the optimization is to find the surface impedance Z_a that minimizes the cost function F

$$\arg \min_{Z_a} F(Z_a) \quad (27)$$

subject to constraints depending on the absorber investigated. It is assumed in this study that prior information about the materials is

known, especially the type of absorber as detailed later, allowing to add extra constraints accordingly. Following the theoretical models in Section 2.2, two categories and their corresponding constraints are defined:

$$\text{Hard materials : } \operatorname{Re}\{Z_a(\omega)\} > 1 \quad \text{for all } \omega \in \mathbb{R}; \quad (28)$$

$$\text{Soft materials : } \operatorname{Re}\{Z_a(\omega)\} < 2 \quad \text{for all } \omega \in \mathbb{R}. \quad (29)$$

Thus, a material is considered hard if its resistance is larger than that of air, the propagation medium of sound waves, or soft if its resistance is of same order or lower than that of air. The two categories overlap in the region $1 < \operatorname{Re}\{Z_a(\omega)\} < 2$ to keep some flexibility, especially since the maximum absorption coefficient possible is attained in this region when $\operatorname{Im}\{Z_a(\omega)\} = 0$. Empirical experimentation with Eqs. (6) and (7) concluded that rigidly backed porous absorbers with approximately a flow resistivity $\sigma \leq 20 \text{ kN.s.m}^{-4}$ and a thickness $h \leq 10 \text{ cm}$ could be considered as soft materials. When adding an air cavity as backing, the theoretical model in Eq. (13) indicates that the values of the flow resistivity and thickness limits even decrease as the cavity depth increases. Perforated panels and membrane absorbers also fall under the same category of soft materials. All the other materials, i.e. microperforated panels and porous materials which parameters exceed the previously stated limits, are considered as hard materials.

In addition to this, specific constraints are applied depending on the type of absorber. Most porous absorbers reach an absorption coefficient close to 1 at high frequencies, meaning that their surface impedances approach $Z_a = 1.6$ as shown in Fig. 1. Moreover, all types of porous absorbers exhibit a negative surface reactance. Consequently, for porous absorbers with either rigid or cavity backing, the surface reactance is bound to be negative at all frequencies by applying a constraint on the highest frequency considered:

$$\text{Porous materials : } \operatorname{Im}\{Z_a(\omega)\} < 0 \quad \text{for } f = 5000 \text{ Hz}. \quad (30)$$

Concerning the resistance, it should also be bound to make sure that the surface impedance approaches the value for maximum absorption at high frequencies. For soft porous absorbers, it is already done through Eq. (29). For hard porous absorbers, however, an extra constraint should be introduced at the two highest octave bands:

$$\text{Hard porous materials : } \operatorname{Re}\{Z_a(\omega)\} < 2 \quad \text{for } f \geq 1600 \text{ Hz}. \quad (31)$$

Combined with Eq. (28) this binds the resistance of hard porous materials between 1 and 2 at the two highest octave bands. Eqs. (30) and (31) ensure that the absorption coefficient of a porous absorber reaches its maximum value at high frequencies with the correct convergence of the surface impedance. In the case of membrane absorbers, a specific constraint is also applied to mimic the theoretical model in Eq. (15). Indeed, both the RMK + 1 and R + 2 model can represent exactly a simple oscillator; however, some deviation is allowed due to the simplicity and inaccuracy of the theoretical membrane model. Therefore, the fractional terms are constrained to be close to mass and spring terms:

$$\text{Membranes : } \gamma \geq 0.9 \quad \text{for RMK + 1}; \quad (32)$$

$$\alpha \geq 0.8 \quad \text{and } \beta \geq 0.9 \quad \text{for R + 2}. \quad (33)$$

The solution to this constrained optimization problem is obtained with MATLAB's integrated solver *fmincon*, a gradient-based solver returning the first local minimum encountered from a given starting point. Consequently, different starting points could lead to different solutions. The local minimum is found by the interior-point method with numerical evaluations of derivatives by forward finite difference. The optimization is carried out on a 5-dimensional space based on the parameters of the impedance model selected. The parameters are normalized by their typical orders of magnitude to facilitate the progress of the algorithm,

such that the 5-dimensional space is $(R_1, M \cdot 10^4, K \cdot 10^{-4}, G \cdot 10^{4\gamma}, \gamma)$ for the RMK + 1 model and $(R_2, A \cdot 10^{-4\alpha}, \alpha, B \cdot 10^{4\beta}, \beta)$ for the R + 2 model. The tolerance on the cost function to detect a local minimum is 10^{-9} and the tolerance on the violation of constraints is 10^{-6} . The maximum number of function evaluations is set to 3000 and the maximum number of iterations to 1000. The optimization can also be terminated if the step size becomes smaller than 10^{-10} . The starting point of the solver is set to $R_1 = 1.6$ or $R_2 = 1.6$ and the other parameters equal to 0 with both general models. This value was chosen to correspond to the peak of the statistical absorption coefficient as a function of surface impedance, or near the peak value depending on frequency, as seen in Fig. 1. To ensure that the solution found by the solver is meaningful, validity conditions are introduced: if the value of the cost function for the local minimum found is too high, the optimization is run again with a new starting point. This point is chosen by assigning random values between 0 and 2 to all the normalized parameters, with the exception of the exponent parameters for which $-1 \leq \gamma \leq 1$ and $0 \leq \alpha, \beta \leq 1$. The validity conditions defined for this purpose depend on the input absorption coefficient to adapt to extreme cases. A given solution is considered valid if it respects

$$F < 0.250 \quad \text{if } \alpha_{in} > 1 \quad \text{in any octave band}; \quad (34)$$

$$F < 0.001 \quad \text{if } \alpha_{in} < 0.1 \quad \text{in 3 or more octave bands}; \quad (35)$$

$$F < 0.015 \quad \text{in the other cases}. \quad (36)$$

The case with $\alpha_{in} > 1$ is included as it is known that absorption coefficients measured in reverberation chambers can exceed 1 [14,16,17]. The condition value on the cost function in Eq. (36) is equivalent to a root-mean-square error of 0.050 in terms of absorption coefficient, which is considered acceptable by the authors for most cases. The other two condition values in Eq. (34) and (35) correspond to root-mean-square errors of 0.204 and 0.013 respectively, which are meant to adapt to extreme values of absorption coefficients.

3.3. Theoretical test cases

Based on the theoretical impedance models presented in Section 2.2, six test cases of sound absorbers have been created. The different parameters involved in each model were given values to correspond to realistic materials. Their statistical absorption coefficients were then calculated using Eq. (5) and averaged in octave bands in order to create input data to the optimization problem. The six test cases are respectively called 'soft porous', 'hard porous', 'porous with cavity', 'membrane', 'perforated panel', and 'microperforated panel'.

The two first test cases are porous absorbers with rigid backing. The first one, labelled 'soft porous', is thin and has a low density; its flow resistivity is $\sigma = 10 \text{ kPa.s.m}^{-2}$ and its thickness is $h = 50 \text{ mm}$. The second porous absorber represents a more dense material and is labelled 'hard porous', with a flow resistivity $\sigma = 30 \text{ kPa.s.m}^{-2}$ and thickness $h = 150 \text{ mm}$. Another theoretical test case was made by adding an air cavity to the soft porous absorber, leading to flow resistivity $\sigma = 10 \text{ kPa.s.m}^{-2}$, thickness $h = 50 \text{ mm}$, and cavity depth $d = 150 \text{ mm}$; it is labelled 'porous with cavity'.

The next test case, labelled 'membrane', corresponds to a hard-board membrane backed by a cavity filled with porous material. The thickness of the membrane is $h = 1 \text{ mm}$ and the density of its material is $\rho = 1000 \text{ kg.m}^{-3}$, hence a mass per unit area $m = \rho h$. The cavity is designed with a depth $d = 250 \text{ mm}$, and the loss factor of the system is set to $\eta = 0.5$.

Finally, two test cases consisting of panels were made. One is a perforated panel backed by a porous material and an air cavity; it is labelled 'perforated panel'. The perforations are circular with a radius $a = 4$ mm, length $L = 16$ mm, and they cover $p = 20\%$ of the surface. The porous material behind the panel has a flow resistivity $\sigma = 10$ kPa.s.m⁻² and a thickness $h = 140$ mm, while the depth of the air cavity is $d = 160$ mm. The last absorber is a microperforated panel simply backed by an air cavity. The perforations are also circular, their radius is $a = 0.05$ mm, their length is $L = 1$ mm, and they add up to a perforation rate $p = 3\%$. The air cavity behind the panel has a depth $d = 20$ mm. This absorber is labelled 'microperforated panel'.

The names 'soft porous', 'hard porous', 'porous with cavity', 'membrane', 'perforated panel', and 'microperforated panel' will be used throughout Sections 4.1 and 4.2 to refer to the theoretical test cases described here. In Section 4.3, however, the retrieval method will be tested against another set of input data coming from Vercammen's round robin study on reverberation chamber measurements [14].

4. Results

4.1. Goodness of fit to original impedances

The statistical absorption coefficients in octave bands of the theoretical test cases are now taken as input to the retrieval method, and the retrieved impedances are compared to the original ones. To assess how close these two quantities are, the coefficient of determination R^2 is calculated as [36]

$$R^2 = 1 - \frac{\|f_{ref} - f_{model}\|_2^2}{\|f_{ref} - \bar{f}_{ref}\|_2^2} \quad (37)$$

with f_{ref} the reference data points, \bar{f}_{ref} their mean, and f_{model} the data points from the explaining model. The ratio in the equation can also be seen as the ratio between the mean-square-error of the model to the reference and the variance of the reference. In the present case, the original impedance is taken as reference and the retrieved one as the explaining model. An R^2 value of 1 indicates that the original and retrieved impedances are identical, and the lower the value of R^2 the more different the two impedances are. The impedances are described in 1/3-octave bands from 100 Hz to 5 kHz, corresponding to the same frequency range as the input absorption coefficient but with a finer frequency resolution.

Two retrieval examples are given in Fig. 2 using the RMK + 1 model. In these two cases, both RMK + 1 and R + 2 models returned the same or very similar surface impedances so the comments given are valid for both of them. Fig. 2a shows the porous absorber with an air cavity. Despite a small offset in the imaginary part below 500 Hz, it can be observed that the retrieval method performs well in obtaining the general trend of the original impedance. However, the fine frequency variations are impossible to capture from the coarse energy-based and frequency-averaged input data. The absorption coefficients considered are given in octave bands, therefore the phenomena taking place in the cavity and modelled with the cotangent term in Eq. 13 are averaged out. Moreover, the frequency dependences of the RMK + 1 and R + 2 models do not allow to reproduce such oscillating behaviours. With the membrane absorber in Fig. 2b, however, the original and retrieved impedances are hardly distinguishable. It is due to the monotonic behaviour of the theoretical model, which can be easily reproduced with the RMK + 1 and R + 2 models. This result is an ideal case of impedance retrieval, and it illustrates the efficiency of the method in obtaining surface impedances from octave-band absorption coefficients.

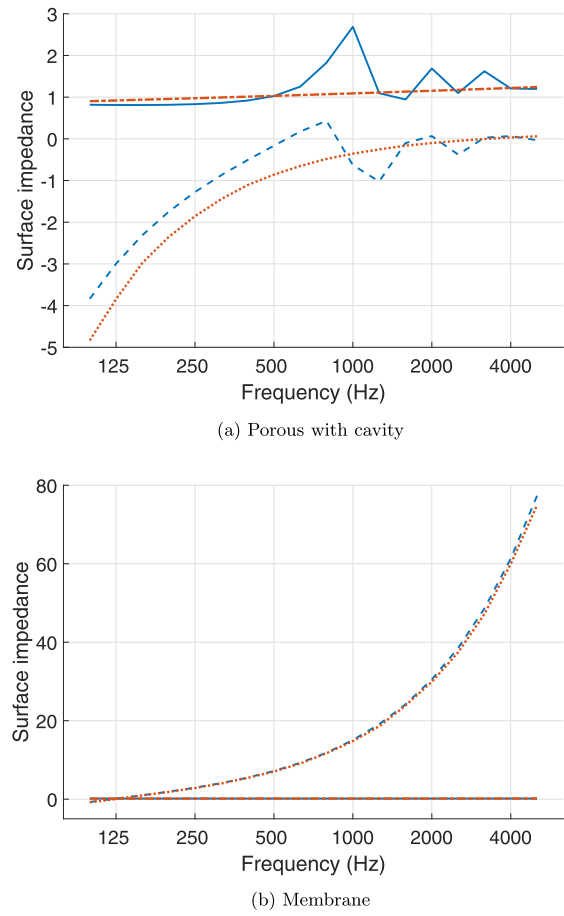


Fig. 2. Original and retrieved impedances in 1/3-octave bands using the RMK + 1 model. Solid blue line: original resistance; Dashed blue line: original reactance; Dash-dotted red line: retrieved resistance; Dotted red line: retrieved reactance. (a) Porous with cavity: $\sigma = 10$ kPa.s.m⁻², $h = 50$ mm, $d = 150$ mm; (b) Membrane: $h = 1$ mm, $\rho = 1000$ kg.m⁻³, $d = 250$ mm, $\eta = 0.5$. (For interpretation of the references to colour in this figure legend, the reader is referred to the web version of this article.)

The parameter values of the two models for all test cases are compiled in Table 1. It should be noted that, for a given model, different values of the parameters can lead to identical surface impedances. The resulting fit between original and retrieved impedances is shown in Table 2. In most cases the agreement between original and retrieved impedances is excellent, with an R^2 value larger than 0.9 in many occurrences and even larger than 0.99 for the membrane absorber with the RMK+1 model. When looking at all the test cases the two general models show comparable results. Nevertheless, the R+2 model is seen to perform better than the RMK+1 model with higher R^2 values for the soft porous and microperforated panel cases. On the down side, the lowest R^2 value found is 0.336 for the microperforated panel with the RMK+1 model, which indicates some deviation from the original impedance. The R+2 model also returns a low R^2 value of 0.419 in this case. Microperforated panels have not been as well studied as other widely used absorption materials, such as porous absorbers for example. Consequently, no additional specific constraints were applied in the retrieving algorithm. It is however expected that the fit between original and retrieved surface impedances would be improved with the help of appropriate constraints suited for microperforated panels. The porous absorber with cavity shown previously in example returned an R^2 value of 0.637 with both models, a fair agreement given the conditions. Indeed, the general models are not capable of reproducing frequency variations due to cavity phenomena in the absorbers. Moreover, input data are given

Table 1Parameters of the general models for the retrieved impedances; values normalized by $\rho_0 c_0$.

(a) RMK + 1 model					
Test case	K	R_1	M	G	γ
Soft porous	5688	1.09	$9.6 \cdot 10^{-6}$	56.8	-0.57
Hard porous	1611	$1.7 \cdot 10^{-3}$	$1.7 \cdot 10^{-5}$	15.5	-0.23
Porous with cavity	3112	$5.6 \cdot 10^{-6}$	$3.3 \cdot 10^{-11}$	0.54	0.08
Membrane	1447	0.15	$2.3 \cdot 10^{-3}$	$8.1 \cdot 10^{-5}$	1
Perforated panel	2888	$7.3 \cdot 10^{-7}$	$2.7 \cdot 10^{-4}$	0.14	0.22
Microperforated panel	$5.4 \cdot 10^4$	$2.3 \cdot 10^{-3}$	$2.1 \cdot 10^{-4}$	21.8	-0.11
(b) R + 2 model					
Test case	A	$-\alpha$	R_2	B	β
Soft porous	3871	-0.94	$3.8 \cdot 10^{-5}$	0.33	0.13
Hard porous	177	-0.55	$1.0 \cdot 10^{-3}$	$6.0 \cdot 10^{-2}$	0.28
Porous with cavity	3112	-1	$4.5 \cdot 10^{-6}$	0.54	0.08
Membrane	1008	-0.97	$6.2 \cdot 10^{-2}$	$2.0 \cdot 10^{-3}$	1
Perforated panel	2954	-1	0.66	$4.5 \cdot 10^{-4}$	0.95
Microperforated panel	$3.1 \cdot 10^4$	-0.92	3.74	0.11	0.37

Table 2 R^2 between original and retrieved surface impedances with the two general models.

Test case	RMK + 1	R + 2
Soft porous	0.821	0.951
Hard porous	0.957	0.972
Porous with cavity	0.637	0.637
Membrane	0.999	0.914
Perforated panel	0.920	0.901
Microperforated panel	0.336	0.419

in octave bands, which are averaged and smooth out said frequency variations; certain assumptions and prior knowledge would then be needed in order to retrieve these fine variations.

Overall, the two general models RMK + 1 and R + 2 showed a similar performance for retrieving the surface impedances of the theoretical test cases, with a slight advantage for the R+2 model. Apart from two test cases, the agreement with the original impedances was excellent. The discrepancies observed were due to the general impedance models not being able to reproduce the fine frequency variations in porous absorbers with air cavities and to the retrieval method not finding the correct impedance without specific constraints for microperforated panels.

4.2. Stability analysis

The cost function associated with the optimization problem to retrieve surface impedances is not guaranteed to have a unique minimum in spite of the constraints applied. Moreover, the optimization problem is solved with a gradient-based method, only returning the first minimum found by the solver. A stability analysis is thus necessary to ensure that the optimization problem is properly set. To do so, and for each test case, the surface impedance is retrieved repeatedly with random starting points and the different solutions are inspected to detect divergences. The range of the starting points depends on the input absorption coefficient: if its values are very low, it is expected that the parameters of the surface impedance will be large. For each starting point, the surface impedance retrieved is first assessed with the validity conditions from Eqs. (34)–(36). Then, all the valid solutions of a given test case are compared with each other. Two surface impedances are considered different enough to be separate solutions when the R^2 value between one of them and the mean of the two is lower than 0.99. In this calculation, the mean is taken as the reference function to determine R^2 in Eq. (37). The stability analysis is performed for

both general models RMK + 1 and R + 2, with the number of starting points being set for each case so that at least 13 valid solutions are retrieved. One result of the stability analysis is illustrated in Fig. 3 with the valid surface impedances found for the membrane absorber and the RMK + 1 model. In this case, 13 valid solutions were found out of 20 random starting points, and they were all similar enough to be considered identical. It can indeed be seen that all 13 surface impedances overlap below 1000 Hz, and the slight deviations appearing at high frequencies are hardly noticeable. The outcome of the stability analysis is summarized in Table 3. Only for the membrane absorber with the R+2 model two different valid solutions appeared; in all the other cases and with both general models, a unique valid solution to the optimization problem was found. This is a good indicator that the constrained problem is well set. Nevertheless, not all starting points lead to valid solutions, especially with the R + 2 model. Indeed, for the membrane absorber and the porous absorber with cavity, 40 starting points were needed to obtain respectively 17 and 16 valid solutions. In other words, only 40% of the starting points lead to valid solutions in the case of the porous absorber with cavity. This also happened to a lesser extent for the soft porous absorber and the perforated panel, where 30 starting points returned 18 and 13 valid solutions respectively. Regarding the RMK + 1 model, it is only for the membrane absorber that 20 starting points yielded 13 valid solutions, equivalent to a 65% rate in the worst scenario. In the other cases,

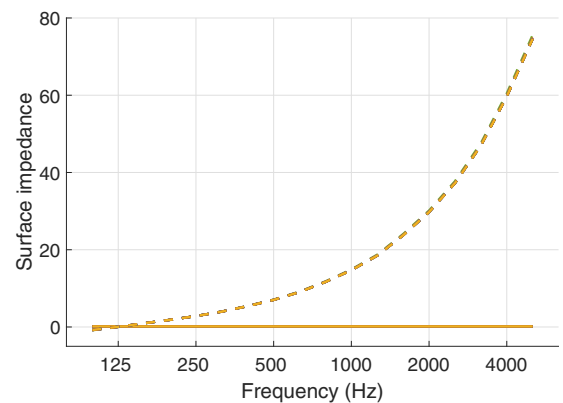


Fig. 3. Surface impedances of all the 13 valid solutions found from random starting points with the RMK + 1 model for the membrane absorber. Yellow: 13 overlapping solutions. Solid line: real part; Dashed line: imaginary part. (For interpretation of the references to colour in this figure legend, the reader is referred to the web version of this article.)

Table 3
Number of starting points, valid solutions, and separate solutions found with the two general models.

Test case	Starting points		Valid solutions		Separate solutions	
	RMK + 1	R + 2	RMK + 1	R + 2	RMK + 1	R + 2
Soft porous	20	30	20	18	1	1
Hard porous	20	20	20	20	1	1
Porous with cavity	20	40	20	16	1	1
Membrane	20	40	13	17	1	2
Perforated panel	20	30	20	13	1	1
Microperforated panel	20	20	20	20	1	1

20 valid solutions were retrieved out of 20 starting points. Hence, the RMK + 1 model exhibited a better convergence towards valid solutions.

The impedance retrieval method with the RMK+1 model appeared to be stable with a unique solution found in each case investigated. However, the R + 2 model exhibited two different valid solutions in one occurrence and showed great difficulties converging to valid solutions in many test cases. Consequently, the RMK + 1 model was found to be far more stable with regard to solving the optimization problem.

4.3. Sensitivity to measurement deviations

In this study noise is not meant as unwanted sound signal but is understood in a data processing point of view, i.e. random effects that pollute the desired information. For practical use of the retrieval methods, the input absorption coefficients will come from measurement data which are contaminated by noise from various origins. The same sound absorber measured at two different times or two different places can yield different absorption coefficients [14,17]. It is therefore important to study how the impedance retrieval method behaves with measured input data. To do so, results from a round robin study [14] conducted in 13 laboratories are taken as input data and the deviations of the absorption coefficients are compared between measurement and retrieval output. Four sound absorbers were investigated in that study: one porous absorber made of foam, one porous absorber made of mineral wool, one membrane absorber, and one arrangement of mineral wool and membrane absorbers in a chessboard pattern; and the same samples were measured in all laboratories. Therefore, for each sound absorber, the absorption coefficient was measured in 1/3-octave bands 13 times, once in each laboratory. In the present study, 13 surface impedances corresponding to the 13 laboratories were retrieved for each sound absorber from the octave band values of the measured absorption coefficients. Then, the retrieved absorption coefficients were calculated with Eq. (5), allowing the comparison with measurement data. As a result, the means and the standard deviations of the 13 measured and the 13 retrieved absorption coefficients are found in Fig. 4. The lines corresponding to the retrieved absorption coefficients with RMK + 1 and R + 2 often overlap, showing that the two models generally return similar solutions. When comparing to the measurements, different behaviours arise. First, divergences appear between the measured and retrieved absorption coefficients of the porous absorbers. The retrieval indeed tends to underestimate absorption at high frequencies. It should be noted here that the values of the measured absorption coefficients exceed 1 in both porous absorbers, for frequencies higher than 2000 Hz with the foam absorber and frequencies above 250 Hz with the mineral wool absorber. This is a known phenomenon happening in reverberation chamber measurements that is due to the finite size of the sample and a not perfectly diffuse sound field. The size effect is most influential at low frequencies, where the wavelengths are of same order as the sample dimensions, and it is taken into account when calculating

absorption coefficients from surface impedances with Eq. (5) through the radiation impedance. However, the non-isotropic sound field affects broadband frequencies and is not accounted for in the retrieval method as it assumes a perfectly diffuse sound field. Hence, the retrieved absorption coefficients tend to exceed 1 less than measured values. It is also seen that the standard deviations of the retrieved absorption coefficients become much lower than those of the measured ones above 1000 Hz. The reason behind this could be that the retrieval method overconstrains the surface impedances of porous absorbers at high frequencies. The second behaviour observed occurs with the membrane absorber. Below 1000 Hz, the measured and retrieved absorption coefficients are close to each other with both general models, but above 1000 Hz, the absorption coefficients retrieved with RMK+1 have very low standard deviations and are noticeably underestimated. Some modelling inaccuracies could be at the origin of this discrepancy. Lastly, for the chessboard absorber, the measured and retrieved absorption coefficients are similar both in terms of mean and standard deviation at all frequencies.

The relative standard deviation (RSD) between the 13 absorption coefficients of each sound absorber is also plotted in Fig. 5. Except for the membrane absorber, the RSD of the absorption coefficients retrieved with the RMK + 1 and R + 2 models are similar or identical. Besides, the two porous absorber cases exhibit the same behaviour: for both the foam and the mineral wool, the RSD of the retrieved absorption coefficients is consistently lower than that of the measured ones and even reach values close to 0 at frequencies higher than 2000 Hz and 1000 Hz, respectively. This is another illustration that porous absorbers may be overconstrained at high frequencies. Concerning the membrane absorber, the absorption coefficients retrieved with the general models have similar RSD values with the measured ones between 100 Hz and 630 Hz, and higher values above 630 Hz. This frequency region above 630 Hz corresponds to where the measured and retrieved absorption coefficients are around or below 0.1. It is seen that the RSD obtained with the RMK+1 model largely increases in the 1000 Hz and 2000 Hz octave bands but becomes smaller than the RSD of the measurement above 4000 Hz. For the R+2 model, its corresponding RSD appears to follow the behaviour of the measurement but with a sharper increase above 1000 Hz. Lastly, in the case of the chessboard arrangement, the RSD of the measured and retrieved absorption coefficients agree very well with each other; the only large difference appears at 100 Hz where the RSD is 0.1 lower for the retrieved coefficients. It should be kept in mind that the chessboard arrangement consists of small patches of porous and membrane absorbers. Despite the good match in terms of absorption coefficient, the retrieval method here returns an equivalent surface impedance for the whole arrangement. In a modeling perspective, to avoid introducing errors with such an approximation it would be beneficial to retrieve the surface impedances of the two types of patches separately if data is available. Nevertheless, this part of the study focuses on comparing deviations between input and retrieved absorption coefficients, for which the behaviour of the method is satisfactory.

Overall, the RSD values of the retrieved absorption coefficients were similar to or lower than those of the measured data thanks to the properties of the impedance models and to the optimization constraints. The only exception is the membrane absorber at high frequencies where the absorption coefficients are very low. It can then be said that the impedance retrieval method does not amplify noise and deviations that appear in measured data, and it does not introduce any noise either.

5. Discussion

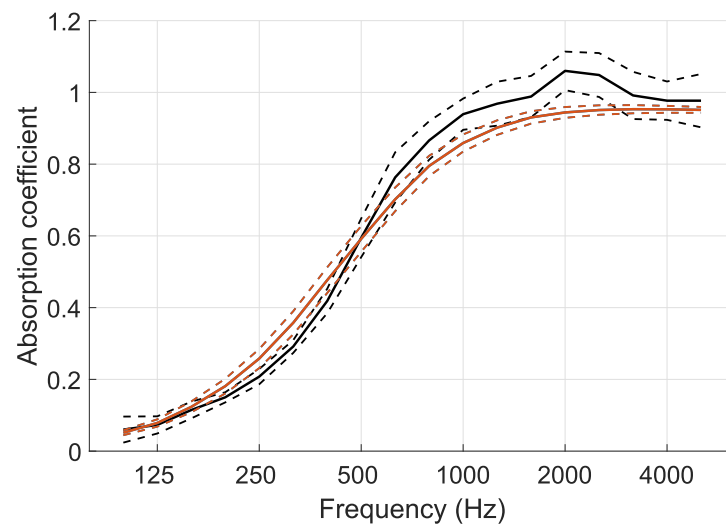
5.1. Choice of a general impedance model

In the light of the results presented here, the RMK + 1 model appears to be better suited than the R + 2 model to represent the various surface impedances of common sound absorbers found in room acoustics. The two models are closely related to each other

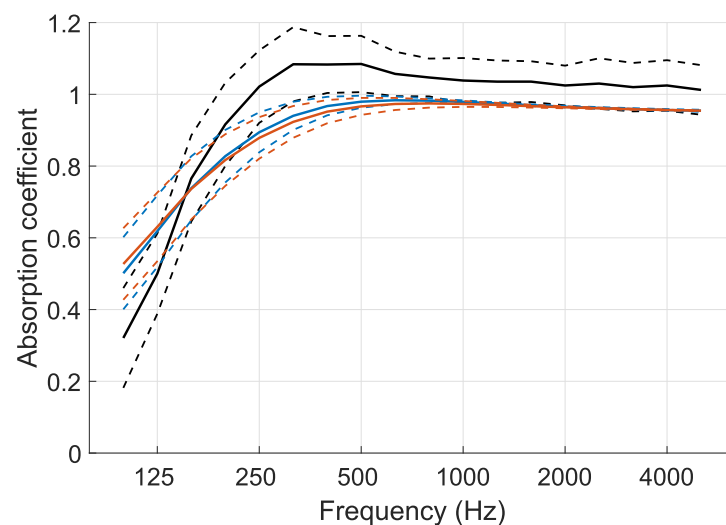
in their construction, and as could be expected, they lead to similar results in many cases. Despite this similarity, significant differences could be found in the stability analysis. It was indeed observed that the R + 2 model converged to valid solutions for less than half of the starting points in three different test cases, whereas the RMK + 1 model returned valid solutions for all starting points with every test case except one, where 65% of the starting points lead to valid solutions. Given that the fitness to known impedances and the sensitivity to measurement data showed no significant advantage for one or the other model, the choice in favour of the RMK + 1 model is made due to its higher stability.

5.2. Validity of the retrieval method

The efficiency of the method to convert octave-band absorption coefficients into surface impedances has been validated in the present paper. However, a few limitations exist and should be kept in

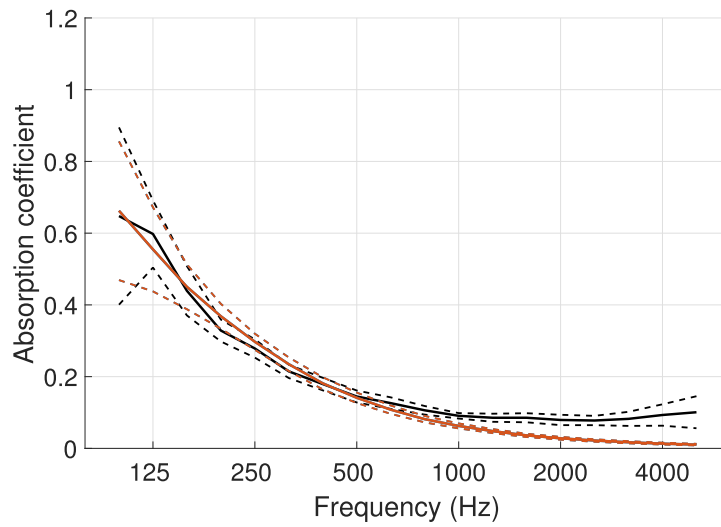


(a) Foam absorber.

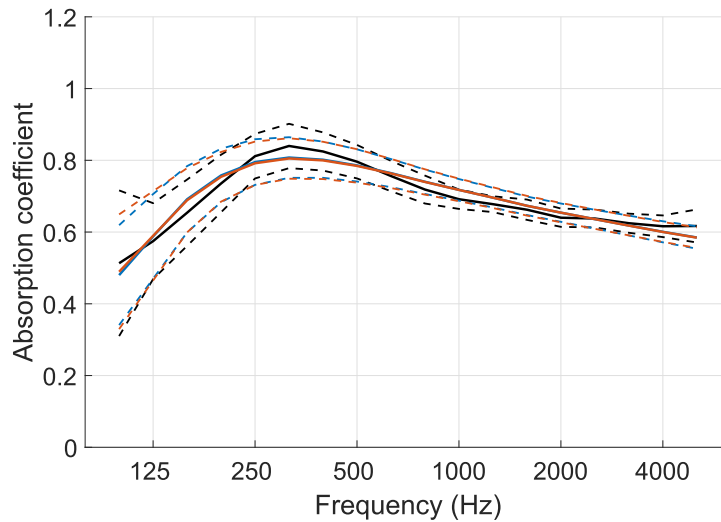


(b) Mineral wool absorber.

Fig. 4. Measured and retrieved means of the 13 1/3-octave band absorption coefficients. Black line: measured in [14]; Blue line: calculated from the retrieved impedances with RMK + 1; Red line: calculated from the retrieved impedances with R + 2; Dashed lines: standard deviations. (For interpretation of the references to colour in this figure legend, the reader is referred to the web version of this article.)



(c) Membrane absorber.



(d) Chessboard arrangement.

Fig. 4 (continued)

mind. The method relies on equations assuming local reaction and mounting of measured sample in an infinite baffle which lead to approximations. It was also seen that cavity phenomena occurring at high frequencies in some sound absorbers can not be reproduced and are smoothed out. Nevertheless, most of the numerical methods that can benefit from impedance boundary conditions are only suitable at low frequencies due to computation time considerations; it is thus considered an acceptable drawback. The optimization constraints are subject to another limitation: choosing which constraints apply to a given case relies on knowing the type of material under study. It was seen that a lack of knowledge about a material could impede the performance of the impedance retrieval. It would be advantageous if the surface impedance of a material could be retrieved without any prior knowledge. This could be achieved by implementing an automated detection of the material based on the frequency dependency of the values of absorption coefficient. Although outside the scope of this paper, further research on this topic would be a great addition to the presented

method. Furthermore, typical building materials like brick and concrete walls were not included in this study. Such hard materials reflect most of the incoming sound energy without a phase shift, implying that their surface impedances consist of a very large resistance and a low reactance. Given the formulation of the RMK + 1 model, it is foreseen that this behaviour will be nicely reproduced with the retrieval method, possibly with the help of adapted constraints.

5.3. Prospected applications

The present method to retrieve surface impedances from absorption coefficients will enable new improvements in the accuracy of room acoustic simulations. In the case of wave-based methods it will be possible to realistically represent boundaries, in contrast with the common rigid boundaries or educated guesses one has to assume to describe boundary conditions. Consequently, better input data to the numerical models will lead to better

simulation results. Some advantages can also be found in geometrical acoustics: knowledge about complex surface impedances allows to determine angle-dependent absorption coefficients based on complete information instead of relying on approximate real-valued impedances; hence, the calculation of reflections can be improved, especially in cases with grazing incidence. These improvements will benefit hybrid calculations doubly as they make use of wave-based methods at low frequencies and geometrical acoustics at high frequencies.

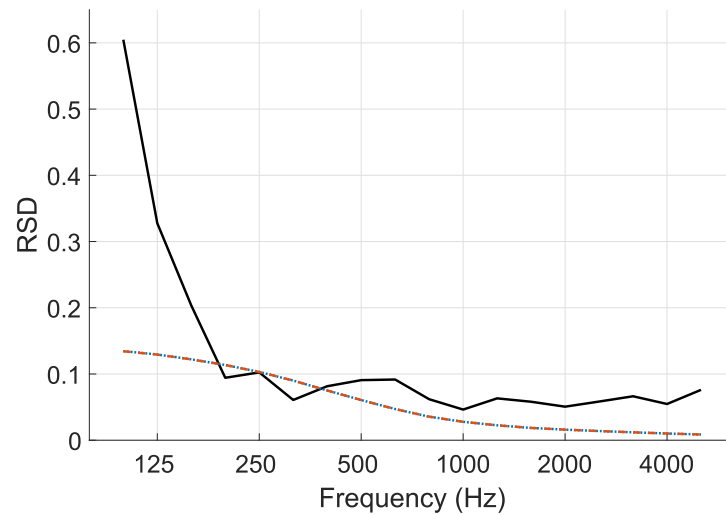
For frequency-domain calculations, implementing the new frequency-dependent boundary conditions is straight-forward. For time-domain calculations, however, some more work has to be done. In order to avoid convolution operations that are computationally heavy, the surface impedance can be turned into an infinite impulse filter through the Z-transform. A thorough investigation about filter orders and best practice for this operation with the RMK + 1 model would complement the present study

nicely, as it would bring time-domain room acoustic simulations one step closer to practical application.

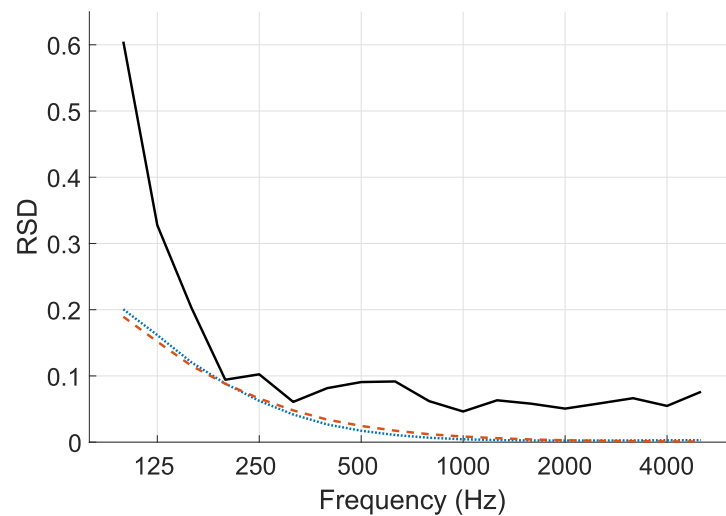
More generally, values of boundary parameters at very low frequencies can be inferred thanks to the general impedance model. Since measurement methods are hardly reliable in this frequency range, an extrapolation given by the RMK + 1 model can provide more accuracy than the simple and common assumption of constant values between the 63 Hz and 125 Hz octave bands.

6. Conclusion

The present paper introduced a method to obtain approximate surface impedances from octave-band absorption coefficients. A general impedance model to represent common building materials found in room acoustics is proposed, based on the simple oscillator model and an additional fractional calculus term. This model,

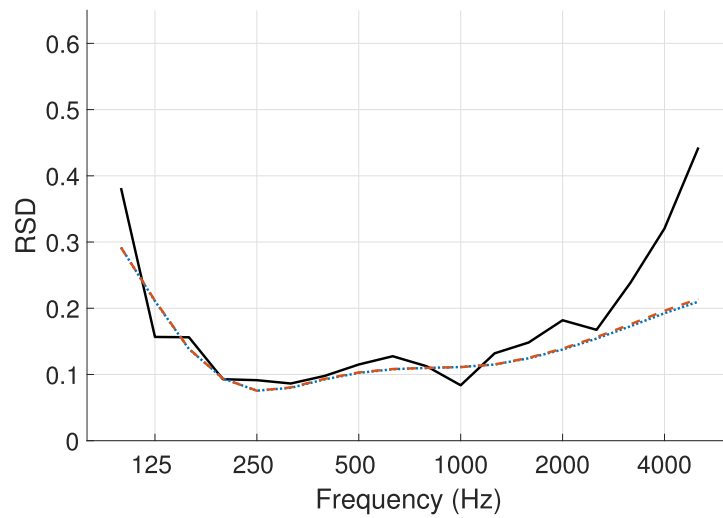


(a) Foam absorber.

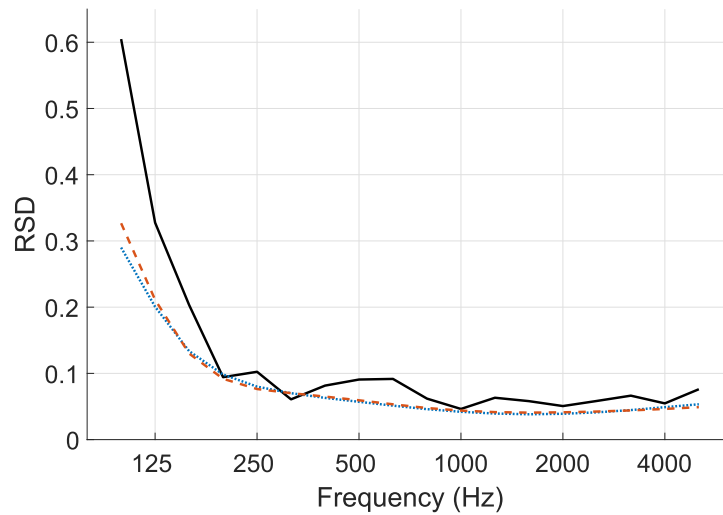


(b) Mineral wool absorber.

Fig. 5. Relative standard deviations between the 13 1/3-octave band absorption coefficients. Solid black line: measured in [14]; Dotted blue line: calculated from the retrieved impedances with RMK + 1; Dashed red line: calculated from the retrieved impedances with R + 2. (For interpretation of the references to colour in this figure legend, the reader is referred to the web version of this article.)



(c) Membrane absorber.



(d) Chessboard arrangement.

Fig. 5 (continued)

called RMK + 1, is therefore guaranteed to respect physical feasibility. For given absorption coefficient data, the parameters of the RMK + 1 model are determined by solving a constrained optimization problem to ensure that the solution found corresponds to the type of material investigated. Several tests have been performed to bring evidence on the efficiency of the retrieval method. Starting with theoretical test cases, the retrieved surface impedances showed an excellent fit with almost all the original impedances. This proves that the RMK + 1 model is capable of approximating the surface impedances of common sound absorbers and that the optimization problem is an efficient way to convert absorption coefficients. The stability of the method has also been tested by solving the optimization problem with different random starting points. For all of the theoretical test cases but one, solutions fulfilling the validity conditions were found from all the starting points. Furthermore, the valid solutions were always corresponding to the same surface impedance. This indicates that the retrieval method is stable. Lastly, the method has been confronted with real

measurement data from a study where sound absorber samples were measured in different laboratories. The deviations among the measured absorption coefficients have been compared to those among the retrieved ones, and it showed that the retrieval method rarely amplified noise that is inherently present in measurement data. Therefore it can be concluded that the optimization problem set to retrieve surface impedances is not oversensitive to noise in input data and does not generally introduce any noise either. Overall, the retrieval method with the RMK + 1 model has been found to be well-suited to common sound absorbers, stable, and not oversensitive to noise. Thus, it is considered an appropriate solution to obtain more complete information on boundary conditions from the widely available absorption coefficient data.

Now that the method to obtain surface impedances from absorption coefficient data has been validated, frequency-dependent impedance boundary conditions can be implemented in numerical methods, providing more accurate simulations for room acoustics.

References

- [1] Kuttruff H. Room acoustics. London, UK, and New York, USA: Taylor and Francis; 2009. p. 101–26. Ch. 4.
- [2] Bork I. Report on the 3rd round robin on room acoustical computer simulation – part ii: calculations. *Acta Acust United Ac* 2005;91(4):753–63.
- [3] Marbjerg G, Brunskog J, Jeong C-H. The difficulties of simulating the acoustics of an empty rectangular room with an absorbing ceiling. *Appl Acoust* 2018;141:35–45.
- [4] Suh JS, Nelson PA. Measurement of transient response of rooms and comparison with geometrical acoustic models. *J Acoust Soc Am* 1999;105(4):2304–17.
- [5] Wareing A, Hodgson M. Beam-tracing model for predicting sound fields in rooms with multilayer bounding surfaces. *J Acoust Soc Am* 2005;118(4):2321–31.
- [6] Jeong C-H, Ih JG, Rindel JH. An approximate treatment of reflection coefficient in the phased beam tracing method for the simulation of enclosed sound fields at medium frequencies. *Appl Acoust* 2008;69:601–13.
- [7] Marbjerg G, Brunskog J, Jeong C-H, Nilsson E. Development and validation of a combined phased acoustical radiosity and image source model for predicting sound fields in rooms. *J Acoust Soc Am* 2015;138(3):1457–68.
- [8] Prislán R, Veble G, Svensen D. Ray-trace modeling of acoustic green's function based on the semiclassical (eikonal) approximation. *J Acoust Soc Am* 2016;140(4):2695–702.
- [9] Lam YW, Hargreaves J. Time domain modelling of room acoustics. *Proc Acous* 2012 Nantes 2012;1:595–605.
- [10] Bilbao S, Hamilton B, Botts J, Savioja L. Finite volume time domain room acoustics simulation under general impedance boundary conditions. *IEEE/ACM Trans Audio Speech Language Process* 2016;24(1):161–73.
- [11] Hornikx M, Krijnen T, van Harten L. Openpstd: the open source pseudospectral time-domain method for acoustic propagation. *Comput Phys Commun* 2016;203:298–308.
- [12] Jeong C-H. Absorption and impedance boundary conditions for phased geometrical-acoustics methods. *J Acoust Soc Am* 2012;132(4):2347–58.
- [13] ISO 354:2003. Acoustics – measurement of sound absorption in a reverberation room. Geneva, Switzerland: International Organization for Standardization; 2003.
- [14] Vercammen MLS. Improving the accuracy of sound absorption measurement according to iso 354. In: *Proceedings of the International Symposium on Room Acoustics ISRA*.
- [15] Rindel JH. An impedance model for estimating the complex reflection factor. *Proc Forum Acust* 2011;1535–40.
- [16] Jeong C-H. Converting sabine absorption coefficients to random incidence absorption coefficients. *J Acoust Soc Am* 2013;133(6):3951–62.
- [17] Jeong C-H, Chang JH. Reproducibility of the random incidence absorption coefficient converted from the sabine absorption coefficient. *Acta Acust United Ac* 2015;101(1):99–112.
- [18] Mondet B, Brunskog J, Jeong C-H, Rindel JH. Retrieving complex surface impedances from statistical absorption coefficients. *Proc InterNoise 2017 Hong Kong* 2017:403–12.
- [19] Kuttruff H. Room acoustics. London, UK, and New York, USA: Taylor and Francis; 2009. p. 35–66. Ch. 2.
- [20] Rienstra SW. Impedance models in time domain including the extended hemholtz resonator model. In: *Proceedings of the 12th AIAA/CAS Aeroacoustics Conference*, Cambridge, USA. p. 2006–686.
- [21] Thomasson SI. On the absorption coefficient. *Acustica* 1980;44:265–73.
- [22] Thomasson SI. Theory and experiments on the sound absorption as function of the area. Report No. TRITA-TAK-8201. Stockholm, Sweden: Department of Technical Acoustics, Royal Institute of Technology; 1982.
- [23] Morfey CL. Dictionary of acoustics. London, United Kingdom: Academic Press; 2001.
- [24] Rindel JH. Modelling the angle-dependent pressure reflection factor. *Appl Acoust* 1993;38:223–34.
- [25] Brunskog J. The forced sound transmission of finite single leaf walls using a variational technique. *J Acoust Soc Am* 2012;132(3):1482–93.
- [26] Davy JL, Larner DJ, Wareing RR, Pearse JR. The average specific forced radiation wave impedance of a finite rectangular panel. *J Acoust Soc Am* 2014;136(2):525–36.
- [27] Allard JF, Atalla N. Propagation of sound in porous media. Chichester, UK: John Wiley and Sons; 2009. p. 29–44. Ch. 3.
- [28] Miki Y. Acoustical properties of porous materials – modifications of Delany-Bazley models. *J Acoust Soc Jpn* 1990;11(1):19–24.
- [29] Das S, Pan I. Fractional order signal processing: introductory concepts and applications. Heidelberg, Germany: Springer; 2012. Ch. 1. pp. 1–12.
- [30] Cox TJ, D'Antonio P. Acoustic absorbers and diffusers: theory, design and application. London, UK, and New York, USA: Taylor and Francis; 2009. p. 156–95. Ch. 5.
- [31] Cox TJ, D'Antonio P. Structure-borne sound: structural vibrations and sound radiation at audio frequencies. Germany: Springer, Heidelberg; 2005. p. 149–235. Ch. 4.
- [32] Ver IL, Beranek LL. Noise and vibration control engineering. Hoboken, USA: John Wiley and Sons; 2006. p. 215–78. Ch. 8.
- [33] Maa DY. Potential of microperforated panel absorber. *J Acoust Soc Am* 1998;104(5):2861–6.
- [34] Bagley RL. A theoretical basis for the application of fractional calculus to viscoelasticity. *J Rheol* 1983;27(3):201–10.
- [35] Axtell M, Bise ME. Fractional calculus application in control systems. In: *Proceedings of the IEEE NAECON 1990*, Dayton, USA. p. 563–6.
- [36] Devore JL. Probability and statistics for engineering and the sciences. Boston, USA: Brooks/Cole; 2011. p. 477–89. Ch. 12.

APPENDIX C

Parametric study of the Equivalent Source Method and interior domain calculations

Parametric study of the Equivalent Source Method and interior domain calculations

Boris Mondet^{a,b,*}, U. Peter Svensson^c, Jonas Brunskog^b, Cheol-Ho Jeong^b, Claus Lynge Christensen^a, Jens Holger Rindel^a

^a*Odeon A/S, DTU Science Park, Denmark*

^b*Acoustic Technology, DTU Electrical Engineering, Technical University of Denmark, Denmark*

^c*Dept. of Electronic Systems, Norwegian University of Science and Technology, Norway*

Abstract

To this day in room acoustics, simulation methods are not capable of delivering accurate results in a timely manner at low frequencies. The present paper investigates the potential of the Equivalent Source Method, commonly used in acoustics for radiation and scattering problems. The method is implemented in the time domain to meet the needs on computation efficiency. The stability and accuracy of the Equivalent Source Method in the time domain are first investigated with a single reflection on a rigid finite plate. This simple test case allows to understand the fundamental properties of the method. An interior problem is then studied, consisting of a rectangular box with rigid or finite uniform impedance boundaries. The impulse responses calculated show that errors propagate in simulations through the multiple reflections on surfaces, leading to either instability or numerical damping.

Keywords: Equivalent Source Method, Time domain, Interior problem, Numerical stability, Room acoustics

1. Introduction

For a long time the simulation of room acoustics has been dominated by geometrical acoustics methods. These methods are indeed computationally efficient and very well suited to spaces such as concert halls and auditoria [1]. However, they offer limited accuracy in small volumes where acoustic conditions are also of crucial importance [2]. This is the case for example in classrooms, offices, and meeting rooms. This shortcoming is due to the energy description of the sound field made in commercially available geometrical acoustics, which does not account for interference or modal behaviour. As a consequence, and thanks to the ever-increasing power of computers, numerical methods for differential equations are becoming attractive alternatives for room acoustic simulations. They rely on solving the wave equation, or an equation derived from it, and thus inherently represent interference, modes and diffraction effects. The most common methods in acoustics are the Finite Element Method [3], the Boundary Element Method [4], and the Finite Difference in the Time Domain with its offshoots [5]. In the present study the Equivalent Source Method (ESM) in the time domain was chosen to be applied to room acoustics. It is based on solving the boundary conditions associated with the wave equation but compromises some accuracy to simplify calculations and reduce computation time.

The Equivalent Source Method was originally designed for sound radiation and scattering from objects [6]. Its frequency-domain formulation has been applied to various problems, including enclosures [7], street canyons [8], and large open scenes [9]. Kropp and Svensson [10] introduced its formulation in the time domain, but research on the topic was not furthered until Lee, Brentner and Morris [11, 12]. They notably

*Corresponding author

Email address: bojmo@elektro.dtu.dk (Boris Mondet)

made use of truncated Singular Value Decomposition and running average to stabilize the solution to the numerical problem. However, they did not address the causes of instability. Lee [13] later gathered the state-of-the-art knowledge on the topic to establish guidelines for radiation and scattering problems. The present work investigates instability and accuracy issues in the Equivalent Source Method. Moreover, unlike previous studies, the method is employed to solve an interior problem by simulating the sound field inside a rectangular box.

The theoretical aspects of the Equivalent Source Method are presented in section 2. The problem to be solved is derived from the boundary condition equation, with both rigid and finite impedance boundaries. In section 3, the Equivalent Source Method is first investigated with a single-plane reflection. This simple test case allows to understand the fundamental behaviour of the method and establish stability and accuracy conditions. The conditions found are then assessed in section 4 on an interior problem by simulating the impulse response of a small rectangular room.

2. Theory

For the Equivalent Source Method treated in this study, sound propagation is considered in the time domain and a three-dimensional space. This is described with the free field Green's function [14]

$$G(r, t) = \frac{1}{4\pi} \frac{\delta(t - r/c)}{r} \quad (1)$$

with r the distance between source and receiver, t the time variable, δ the Dirac delta function, and c the speed of sound. Given a point source with strength $q(t) = \rho \partial Q / \partial t$, $Q(t)$ being the volume velocity, the sound pressure at a receiver position is then

$$p(r, t) = \frac{1}{4\pi} \frac{q(t - r/c)}{r}. \quad (2)$$

If sound is emitted from several sources, the sound pressure at the receiver location is calculated as the sum of the contributions of individual sources.

2.1. General principle

The Equivalent Source Method is based on placing sources outside the domain to satisfy boundary conditions together with the original source located in the room. Equivalent sources can be defined as monopoles or multipoles, and they can be distributed around the domain uniformly or not. The boundaries are also discretized with control points. In this study, a uniform distribution of monopoles is considered as illustrated in Fig. 1. The total number of equivalent sources and control points are respectively defined as N_e and N_b . The strengths of the equivalent sources are then determined by solving the boundary condition equations. The general case of impedance boundaries is explained in section 2.5, but the method is first described with rigid boundaries for simplicity. In the case of rigid boundaries, the particle velocity \mathbf{u} is bound to zero in the normal direction:

$$\mathbf{u}(t) \cdot \boldsymbol{\eta}_n = 0. \quad (3)$$

Bold characters are used to denote vectors. $\boldsymbol{\eta}_n$ is the unit normal vector to the surface pointing towards the domain. The particle velocity and sound pressure are linked by the conservation of momentum in its linearized form as

$$\frac{\partial \mathbf{u}}{\partial t}(t) = -\frac{1}{\rho} \nabla p(t). \quad (4)$$

By separating the sound pressure into incident and reflected pressures p_i and p_r , the boundary condition equation can be written as

$$\nabla p_r(t) \cdot \boldsymbol{\eta}_n = -\nabla p_i(t) \cdot \boldsymbol{\eta}_n. \quad (5)$$

The gradient of the incident sound pressure can be known exactly under the condition that the strength of the original source has an analytical and differentiable expression. If this is not the case, an estimate can

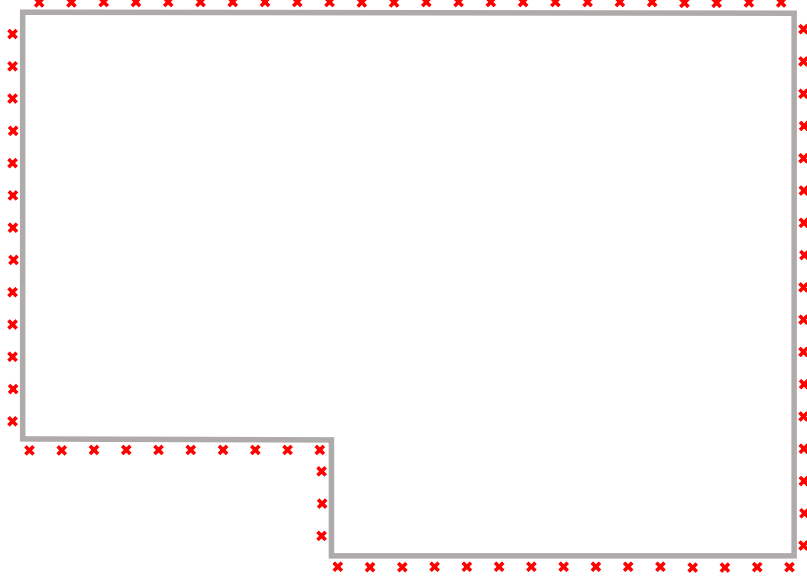


Figure 1: Uniform distribution of equivalent sources (red crosses) for a 2D interior problem.

be found from interpolation techniques. The reflected sound pressure, however, depends on the unknown strengths of the equivalent sources. At a given control point b , the reflected sound pressure is the sum of contributions from all equivalent sources $p_r(t) = \sum_{e=1}^{N_e} p_{be}(t)$. The boundary condition equation then becomes

$$\sum_{e=1}^{N_e} \nabla p_{be}(t) \cdot \boldsymbol{\eta}_n = -\nabla p_i(t) \cdot \boldsymbol{\eta}_n. \quad (6)$$

The pressure gradient from one equivalent source e can be expressed from Eq. (2) as

$$\nabla p_{be}(t) = \frac{1}{4\pi} \left(-\frac{q_e(t - r_{be}/c)}{r_{be}^2} - \frac{1}{cr_{be}} \frac{\partial q_e}{\partial t}(t - r_{be}/c) \right) \boldsymbol{\eta}_{be}, \quad (7)$$

where q_e is the strength of source e , r_{be} is the distance between point b and source e , and $\boldsymbol{\eta}_{be}$ is the unit directional vector from source e to point b . As numerical schemes cannot handle continuous time, the time variable t is discretized as $t_n = n\Delta t$, with $n \in \mathbb{N}$ and Δt the time resolution. The travel time between source e and point b can also be expressed in time steps as $r_{be}/c = \nu_{be}\Delta t$. This results in

$$t_n - r_{be}/c = (n - \nu_{be})\Delta t. \quad (8)$$

However, $\nu_{be} \in \mathbb{R}$ unlike n . Therefore, the values of the equivalent source strengths must be interpolated.

2.2. Time interpolation

The process is explained here for linear interpolation, but a more general approach for any order desired can be found in the appendix in section 7. The integer numbers surrounding ν_{be} are defined as

$$\nu_{be}^- \leq \nu_{be} \leq \nu_{be}^+. \quad (9)$$

Hence, the discrete time steps around $(n - \nu_{be})\Delta t$ are

$$(n - \nu_{be}^+)\Delta t \leq (n - \nu_{be})\Delta t \leq (n - \nu_{be}^-)\Delta t. \quad (10)$$

Linear interpolation can then be applied to the source strength

$$q_e((n - \nu_{be})\Delta t) = \frac{(n - \nu_{be}^-)\Delta t - (n - \nu_{be})\Delta t}{\Delta t} q_e((n - \nu_{be}^+)\Delta t) + \frac{(n - \nu_{be})\Delta t - (n - \nu_{be}^+)\Delta t}{\Delta t} q_e((n - \nu_{be}^-)\Delta t) . \quad (11)$$

This expression can easily be simplified to give

$$q_e((n - \nu_{be})\Delta t) = (\nu_{be} - \nu_{be}^-) q_e((n - \nu_{be}^+)\Delta t) + (\nu_{be}^+ - \nu_{be}) q_e((n - \nu_{be}^-)\Delta t) . \quad (12)$$

From now on Δt will be dropped in function arguments for clarity. Linear interpolation implies the first order approximation to calculate derivatives. Applying it to the source strength time derivative yields

$$\frac{\partial q_e}{\partial t}(n - \nu_{be}) = \frac{q_e(n - \nu_{be}^-) - q_e(n - \nu_{be}^+)}{\Delta t} . \quad (13)$$

Finally, injecting Eq. (12) and Eq. (13) in Eq. (7) results in

$$\nabla p_{be}(n) = \frac{1}{4\pi} \left(-\frac{\nu_{be} - \nu_{be}^-}{r_{be}^2} q_e(n - \nu_{be}^+) - \frac{\nu_{be}^+ - \nu_{be}}{r_{be}^2} q_e(n - \nu_{be}^-) - \frac{1}{cr_{be}} \frac{q_e(n - \nu_{be}^-) - q_e(n - \nu_{be}^+)}{\Delta t} \right) \boldsymbol{\eta}_{be} . \quad (14)$$

After factorisation it can be rewritten as

$$\nabla p_{be}(n) = \frac{1}{4\pi} \left(\left(-\frac{\nu_{be}^+ - \nu_{be}}{r_{be}^2} - \frac{1}{cr_{be}\Delta t} \right) q_e(n - \nu_{be}^-) + \left(-\frac{\nu_{be} - \nu_{be}^-}{r_{be}^2} + \frac{1}{cr_{be}\Delta t} \right) q_e(n - \nu_{be}^+) \right) \boldsymbol{\eta}_{be} . \quad (15)$$

2.3. Matrix form

The boundary equation to be solved at one control point is given by Eq. (6), which in discrete time becomes

$$\sum_{e=1}^{N_e} \nabla p_{be}(n) \cdot \boldsymbol{\eta}_n = -\nabla p_i(n) \cdot \boldsymbol{\eta}_n . \quad (16)$$

The left-hand side can be replaced by using Eq. (15)

$$\sum_{e=1}^{N_e} \frac{1}{4\pi} \left(\left(-\frac{\nu_{be}^+ - \nu_{be}}{r_{be}^2} - \frac{1}{cr_{be}\Delta t} \right) q_e(n - \nu_{be}^-) + \left(-\frac{\nu_{be} - \nu_{be}^-}{r_{be}^2} + \frac{1}{cr_{be}\Delta t} \right) q_e(n - \nu_{be}^+) \right) \boldsymbol{\eta}_{be} \cdot \boldsymbol{\eta}_n = -\nabla p_i(n) \cdot \boldsymbol{\eta}_n . \quad (17)$$

The scalar product is now defined as $\sigma_{be} = \boldsymbol{\eta}_{be} \cdot \boldsymbol{\eta}_n$. At this point, the factors multiplying $q_e(n - \nu_{be}^-)$ and $q_e(n - \nu_{be}^+)$ are written respectively as matrices $\mathbf{A}, \mathbf{B} \in \mathbb{R}^{N_b \times N_e}$, which components are

$$A_{be} = \frac{1}{4\pi} \left(-\frac{\nu_{be}^+ - \nu_{be}}{r_{be}^2} - \frac{1}{cr_{be}\Delta t} \right) \sigma_{be} , \quad (18)$$

$$B_{be} = \frac{1}{4\pi} \left(-\frac{\nu_{be} - \nu_{be}^-}{r_{be}^2} + \frac{1}{cr_{be}\Delta t} \right) \sigma_{be} . \quad (19)$$

It can be seen in this expression that the matrices \mathbf{A} and \mathbf{B} are independent of time. However, the system of equations cannot be set in matrix form yet. Indeed, the arguments of the source strengths in $q_e(n - \nu_{be}^-)$ and $q_e(n - \nu_{be}^+)$ depend on the pair be of equivalent source and control point. Therefore \mathbf{A} and \mathbf{B} need to be decomposed into matrices corresponding to the discrete time steps. For this purpose, the values of ν_{be}^- and ν_{be}^+ are sorted as

$$\nu_0 = \min(\nu_{be}^-), \quad (20)$$

$$\nu_k = \nu_0 + k, \quad (21)$$

with $k \in \mathbb{N}$. The matrix decomposition is then carried out as follows

$$\mathbf{A} = \sum_{k=0}^n \mathbf{A}_k, \quad (22)$$

$$\mathbf{B} = \sum_{k=1}^n \mathbf{B}_k, \quad (23)$$

with

$$A_{k,be} = \begin{cases} A_{be} & \text{if } \nu_{be}^- = \nu_k \\ 0 & \text{otherwise} \end{cases}, \quad (24)$$

$$B_{k,be} = \begin{cases} B_{be} & \text{if } \nu_{be}^+ = \nu_k \\ 0 & \text{otherwise} \end{cases}. \quad (25)$$

This allows to write the boundary condition equation in matrix form

$$\mathbf{A}_0 \mathbf{q}(n - \nu_0) + \sum_{k=1}^n (\mathbf{A}_k + \mathbf{B}_k) \mathbf{q}(n - \nu_k) = -\nabla \mathbf{p}_i(n) \cdot \boldsymbol{\eta}_n. \quad (26)$$

In this equation $\mathbf{q} \in \mathbb{R}^{N_e \times 1}$ and $\mathbf{p}_i \in \mathbb{R}^{N_b \times 1}$. The equation can be rearranged to have all the known information from already solved previous time steps on the right-hand side, leading to

$$\mathbf{A}_0 \mathbf{q}(n - \nu_0) = -\nabla \mathbf{p}_i(n) \cdot \boldsymbol{\eta}_n - \sum_{k=1}^n (\mathbf{A}_k + \mathbf{B}_k) \mathbf{q}(n - \nu_k). \quad (27)$$

This problem is solved by inverting the matrix \mathbf{A}_0 , which is independent of the time step. Therefore it is only needed to perform the matrix inversion once for the whole simulation. Moreover, \mathbf{A}_0 is sparse as seen from its construction in Eq. (24), making the inversion easier to compute. One of the properties of the Equivalent Source Method is the possibility to have more control points than sources. This leads to an overdetermined problem, and consequently the matrix \mathbf{A}_0 to be inverted is rectangular. In this paper, this inversion is done through non-truncated singular value decomposition: the matrix is decomposed as $\mathbf{A}_0 = \mathbf{U} \mathbf{S} \mathbf{V}^T$, with \mathbf{S} the diagonal matrix of singular values, and \mathbf{U} and \mathbf{V} the corresponding matrices of singular vectors. The inverse matrix is then calculated as $\mathbf{A}_0^{-1} = \mathbf{V} \mathbf{S}^{-1} \mathbf{U}^T$. As a consequence, the least-square solution to the system of equations is found.

2.4. Boundary discretization

The discretization of the domain boundary plays an important role in the Equivalent Source Method. The number of non-zero elements in the matrix \mathbf{A}_0 to be inverted depends on the positions of equivalent sources and control points. Indeed, only the elements of \mathbf{A} that correspond to $\nu_{be}^- = \nu_0$ are retained in \mathbf{A}_0 . In other words, for each equivalent source, only the control points that are reached within the first time step of arrival are taken into account to determine its strength. Discretization must therefore be performed with care.

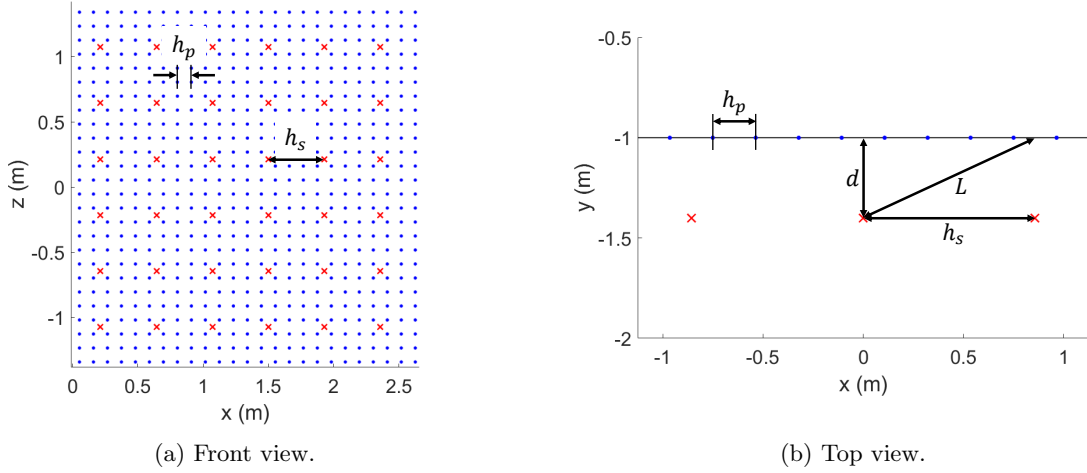


Figure 2: Close-up illustration of the discretization of a surface in the Equivalent Source Method. Blue dots: control points; Red crosses: equivalent sources.

Several parameters govern how the domain boundary is discretized. These parameters consist of the spacing between control points h_p , the spacing between equivalent sources h_s , and the orthogonal distance d between equivalent sources and the surface they are related to. The parameters h_s and h_p are linked by the ratio $\kappa = h_s/h_p$. The distance between an equivalent source and the orthogonal projection of its neighbour is also defined as $L = \sqrt{d^2 + h_s^2}$. An illustration of the geometry with the different parameters is given in Fig. 2. The relative positions of control points and equivalent sources can be decided freely. If control points are located at the orthogonal projections of the equivalent sources on the boundary, singularity can occur from the $1/r_{be}$ terms in matrices \mathbf{A} and \mathbf{B} when the value of d approaches 0. In this study it is chosen to keep the equivalent sources in central positions between control points with the value of κ equal to a power of 2. This allows to avoid potential singularities and ensures that at least four control points are used to determine the strength of a source.

Nevertheless, the choice of locating equivalent sources centrally relative to control points also affects the scalar product $\sigma_{be} = \boldsymbol{\eta}_{be} \cdot \boldsymbol{\eta}_n$ found in Eq. (18,19). This choice implies that the value of the scalar product σ_{be} varies together with the orthogonal distance d . Indeed, when d tends to 0, the vectors $\boldsymbol{\eta}_{be}$ and $\boldsymbol{\eta}_n$ approach orthogonality and their scalar product tends to 0. This is most influential on the nearest control points to an equivalent source, and hence on matrix \mathbf{A}_0 . As a consequence, larger values of q_e are needed to satisfy the boundary conditions when d tends to 0. Inversely, the value of σ_{be} grows as d increases, and lower values of q_e are found to solve the boundary condition equation.

Although there are κ^2 control points per equivalent source in a simulation, it is important to note that not necessarily κ^2 points are reached by a source in the shortest time interval. The number of these points retained with non-zero elements in \mathbf{A}_0 depends indeed on the travel times between the sources and control points and on the sampling frequency. The number of control points taken into account to solve the strength of one equivalent source is noted γ . If $\gamma = \kappa^2$, every control point is reached within the shortest time interval by only one source and is used to solve its strength. In this case, each line of \mathbf{A}_0 has one non-zero element. If $\gamma < \kappa^2$, some control points are not reached within the shortest time interval by any source. This means that their corresponding equations are not used to solve the system, and in the matrix \mathbf{A}_0 their corresponding lines contain only zeros. On the contrary, when $\gamma > \kappa^2$, some control points are used to solve the strength of more than one source, hence increasing the coupling of the system. Some lines of \mathbf{A}_0 then have more than one non-zero element.

2.5. Finite impedance boundaries

When considering boundaries with finite impedances the boundary condition becomes

$$\mathbf{u}(t) \cdot \boldsymbol{\eta}_n = p(t) * y_a(t), \quad (28)$$

with $y_a(t)$ the surface admittance expressed in the time domain. The equation is differentiated over time to apply the conservation of momentum, and the derivative of the convolution on the right-hand side can be written [15]

$$\frac{\partial (p * y_a)}{\partial t}(t) = \frac{\partial p}{\partial t}(t) * y_a(t). \quad (29)$$

The incident and reflected sound pressure are then separated to obtain

$$\frac{1}{\rho} \nabla p_r(t) \cdot \boldsymbol{\eta}_n + \frac{\partial p_r}{\partial t}(t) * y_a(t) = -\frac{1}{\rho} \nabla p_i(t) \cdot \boldsymbol{\eta}_n - \frac{\partial p_i}{\partial t}(t) * y_a(t). \quad (30)$$

Similarly to $\nabla p_i(t) \cdot \boldsymbol{\eta}_n$ previously, $\frac{\partial p_i}{\partial t}(t) * y_a(t)$ is a straightforward calculation if the strength of the original source is known analytically. Moreover the discretization of $\nabla p_r(t) \cdot \boldsymbol{\eta}_n$ has already been described in Eq. (15). Thus, only $\frac{\partial p_r}{\partial t}(t) * y_a(t)$ needs to be derived in a suitable form for matrix equation. From Green's function in Eq. (2) and first order approximation of the derivative in Eq. (13), the convolution operation at one control point b for one equivalent source e is

$$\frac{\partial p_{be}}{\partial t}(n) * y_a(n) = \frac{1}{4\pi r_{be} \Delta t} \sum_{m=0}^M (q_e(n - \nu_{be}^- - m) - q_e(n - \nu_{be}^+ - m)) y_a(m), \quad (31)$$

with M the truncation limit. The terms of the convolution corresponding to $m = 0$ are separated to isolate $q_e(n - \nu_{be}^-)$

$$\begin{aligned} \frac{\partial p_{be}}{\partial t}(n) * y_a(n) = & \left(\frac{y_a(0)}{4\pi r_{be} \Delta t} (q_e(n - \nu_{be}^-) - q_e(n - \nu_{be}^+)) \right. \\ & \left. + \frac{1}{4\pi r_{be} \Delta t} \sum_{m=1}^M (q_e(n - \nu_{be}^- - m) - q_e(n - \nu_{be}^+ - m)) y_a(m) \right). \end{aligned} \quad (32)$$

The convolution corresponding to the total reflected sound pressure at one control point is then

$$\frac{\partial p_r}{\partial t}(n) * y_a(n) = h_b(n, \nu_{be}) + \sum_{e=1}^{N_e} \frac{y_a(0)}{4\pi r_{be} \Delta t} (q_e(n - \nu_{be}^-) - q_e(n - \nu_{be}^+)), \quad (33)$$

with

$$h_b(n, \nu_{be}) = \sum_{e=1}^{N_e} \frac{1}{4\pi r_{be} \Delta t} \sum_{m=1}^M (q_e(n - \nu_{be}^- - m) - q_e(n - \nu_{be}^+ - m)) y_a(m). \quad (34)$$

All the elements composing h_b are known information from previous time steps, it can thus be computed as it is. Moreover, if the surface impedance is constant over frequency, $y_a(m) = 0$ for $m \geq 1$ and it follows that $h_b(n, \nu_{be}) = 0$. At this point it is seen from Eq. (33) that matrices \mathbf{A} and \mathbf{B} defined in Eq. (18,19) are modified and become

$$A'_{be} = \frac{1}{4\pi} \left(-\frac{\nu_{be}^+ - \nu_{be}}{r_{be}^2} - \frac{1}{cr_{be} \Delta t} \right) \sigma_{be} + \frac{y_a(0)}{4\pi r_{be} \Delta t}, \quad (35)$$

$$B'_{be} = \frac{1}{4\pi} \left(-\frac{\nu_{be} - \nu_{be}^-}{r_{be}^2} + \frac{1}{cr_{be} \Delta t} \right) \sigma_{be} - \frac{y_a(0)}{4\pi r_{be} \Delta t}. \quad (36)$$

The matrix decomposition process is then carried out in the same manner, and the whole system takes the following matrix form

$$\mathbf{A}'_0 \mathbf{q}(n - \nu_0) = -\nabla \mathbf{p}_i(n) \cdot \boldsymbol{\eta}_n - \sum_{k=1}^n (\mathbf{A}'_k + \mathbf{B}'_k) \mathbf{q}(n - \nu_k) - \frac{\partial \mathbf{p}_i}{\partial t}(n) * y_a(n) - \mathbf{h}(n). \quad (37)$$

This system is solved by inverting matrix \mathbf{A}'_0 which is still sparse and time-independent.

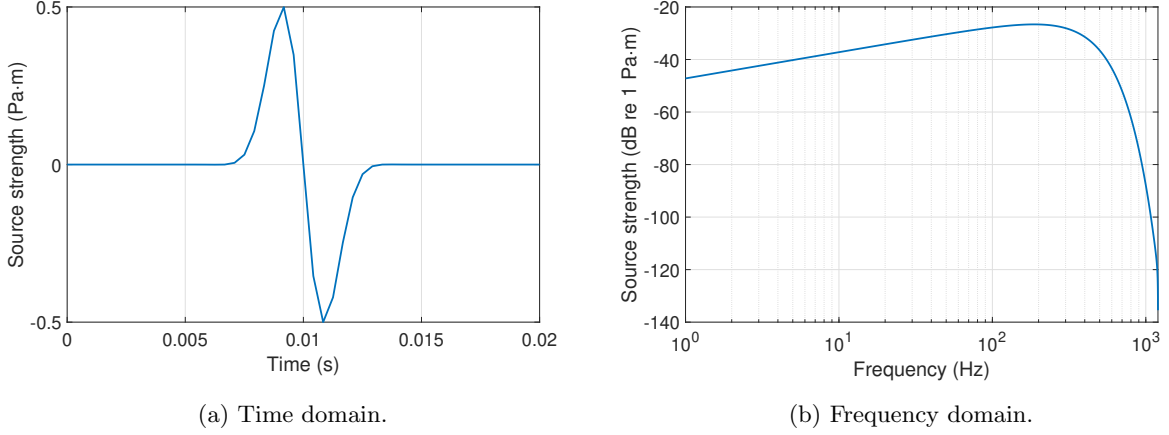


Figure 3: Signal emitted by the original source.

2.6. Methods used as references

The Edge Diffraction Method by Svensson [16, 17] is taken as reference for the simulation of the single-plane reflection in section 3. It is based on Biot and Tolstoy's [18] theory on diffraction of wedges and calculates the response to a delta pulse. The response can then be convoluted with the source signal in Fig. 3.

The exact solution for a rectangular box with rigid boundaries can be found with the Image Source Method, as well as a good estimate for the uniform impedance boundary condition [19, 20]. This method is thus chosen as a reference for the calculation of the impulse response in a rectangular room in section 4.

3. Parametric study

3.1. Numerical setup

All the sources in the simulation are considered as monopoles. The original source is set to emit a sine-modulated Gaussian pulse with a source strength

$$q(t) = -\alpha e^{-\frac{(t-t_0)^2}{2s^2}} \sin(\omega_0(t-t_0)). \quad (38)$$

α is the amplitude of the Gaussian pulse, t_0 defines the peak of the Gaussian pulse and the zero-crossing of its sine-modulated version, s is the bandwidth parameter of the pulse (corresponding to the standard deviation in a Gaussian distribution), and $\omega_0 = 2\pi f_0$ is the angular frequency of the modulation. These parameters are set to $\alpha = 1$ Pa.m, $t_0 = 10$ ms, $s = 1$ ms, and $f_0 = 150$ Hz. The resulting time signal and its frequency content are plotted in Fig. 3 with a sampling frequency $f_s = 2400$ Hz. This sampling frequency is used for all the simulations presented later, although it is seen that the half-power bandwidth of the input signal ranges from 29 Hz to 427 Hz and very little energy is present above 600 Hz. The function $q(t)$ was chosen as input signal for two reasons. The first one is the smoothness of the Gaussian pulse, which provides a finite frequency spectrum. The second reason is that numerical simulations in enclosures need a zero-mean input signal to avoid instabilities; hence, the modulation on the pulse. Indeed, input signals with a non-zero mean pressures lead to a high quasi-static pressure component (also called cavity mode), which is problematic for the Boundary Element Method and the Equivalent Source Method [21].

In order to determine the optimal values for the geometry parameters mentioned previously, the reflection of sound on a single and finite hard plane is investigated. This test case was chosen because it includes both specular reflection and diffraction, two important aspects at low frequencies. The plane is modelled infinitely thin, meaning that the sound field from the Equivalent Source Method is only valid in front of it. 15

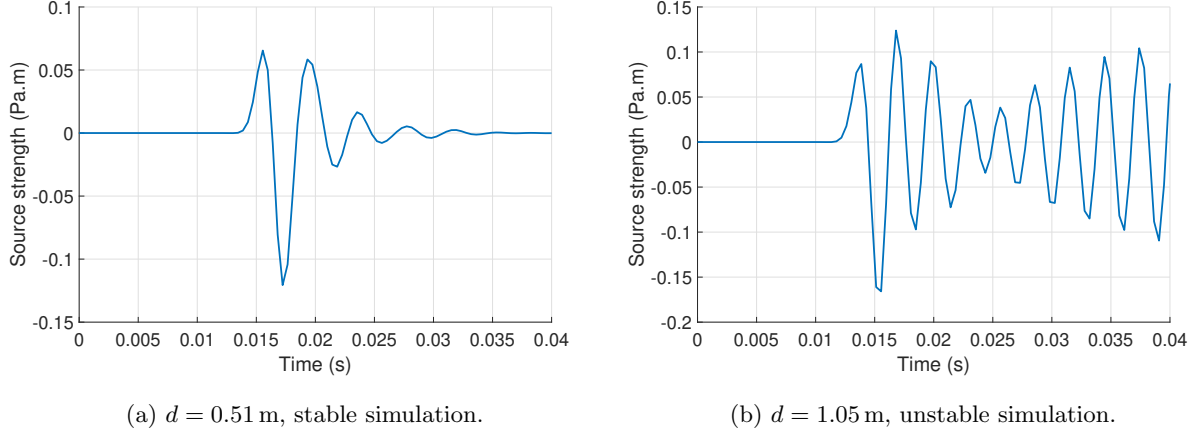


Figure 4: Signal emitted by an equivalent source located at $(x, y, z) = (-0.55 \text{ m}, -d, 1.64 \text{ m})$ for $h_p = 274 \text{ mm}$ and $\kappa = 4$.

simulations have been performed, corresponding to the five values of h_p (53.6 mm, 85.8 mm, 143mm, 214mm, 274mm) combined with the three values of κ (2, 4, 8). For each simulation the orthogonal distance d was varied from $h_p/100$ to $10h_p$ in 20 logarithmic steps. The rigid plane is centered on the origin with lengths of 6 m in the x -direction and 4 m in the z -direction. The sound source is placed at $(-1 \text{ m}, 2.5 \text{ m}, 0.5 \text{ m})$. The sound pressure is calculated on a horizontal grid of receivers at $z = -0.5 \text{ m}$ and ranging from $x = -3 \text{ m}$ to $x = 3 \text{ m}$ and from $y = 0 \text{ m}$ to $y = 4 \text{ m}$, with the distance between receivers being 0.1 m. The error estimate ϵ at one receiver is defined as the mean squared error normalized by the mean squared pressure of the reference

$$\epsilon = \frac{\sum_{n=0}^N (p(n) - p_0(n))^2}{\sum_{n=0}^N p_0(n)^2}, \quad (39)$$

N being the index of the last time step in the simulation, p the sound pressure obtained from the Equivalent Source Method, and p_0 the sound pressure from the reference method. This error is then averaged over all positions defined in the receiver grid to obtain the global error estimate of a simulation $\bar{\epsilon}$.

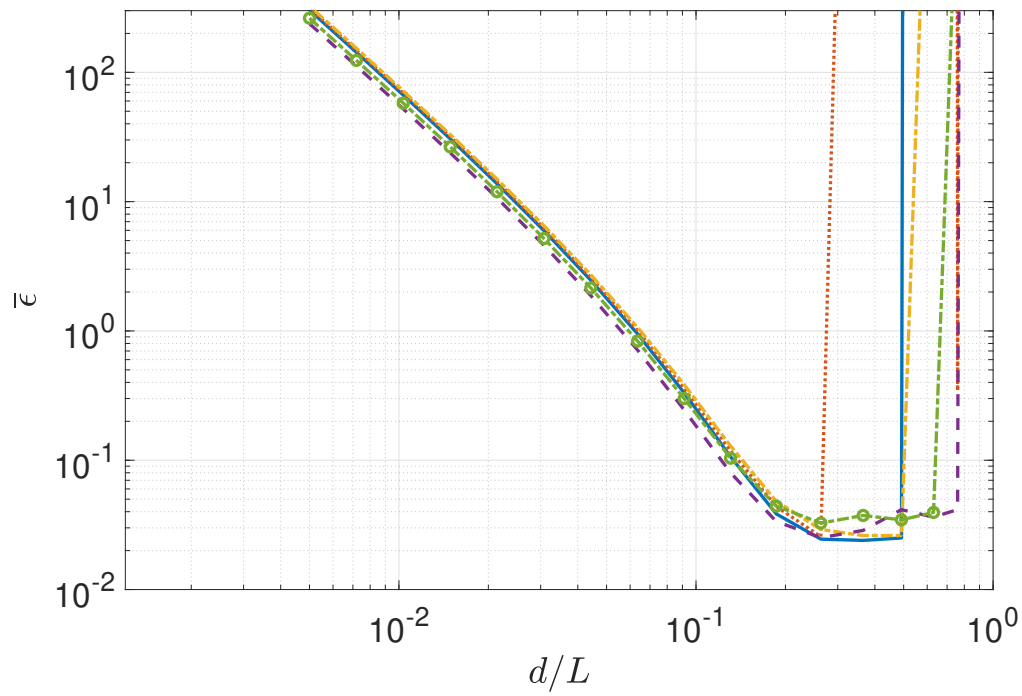
3.2. Stability conditions

The main issue of the Equivalent Source Method is its potential instability. To investigate this phenomenon, the signals emitted by one equivalent source in a stable and an unstable situation are shown in Fig. 4. They were obtained for $h_p = 274 \text{ mm}$, $\kappa = 4$, and respectively $d = 0.51 \text{ m}$ and $d = 1.05 \text{ m}$. The signal of the equivalent source is first explained for the stable case. The first dip and two peaks are the response of the source to the incident sound field. The ripples following the second peak then correspond to the source reacting to the sound field coming from other equivalent sources in the simulation. Two important differences can be observed in the unstable case. First, the amplitude of the ripples is much larger and even reaches values comparable to the first peaks and dip. Secondly, the first ripple seems to happen simultaneously with the second peak of the response to the incident sound. This indicates that the equivalent sources have a large influence on each other, leading to an unstable feedback loop process where the signal amplitudes keep growing with time.

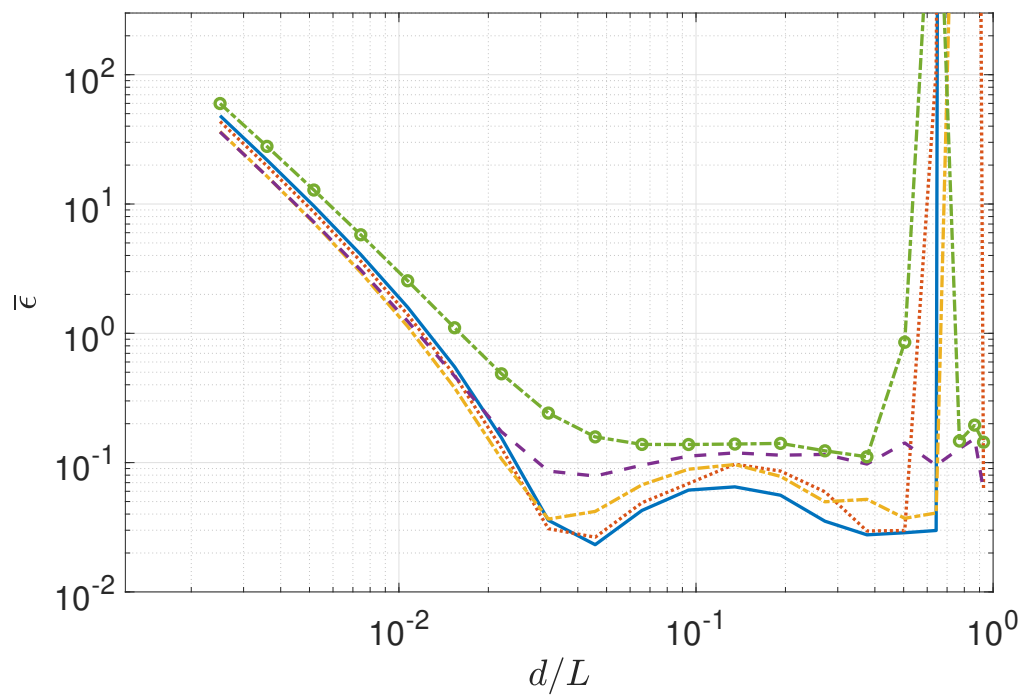
Stability therefore depends on how much influence each equivalent source has on its neighbours. This influence is assessed with the quantity d/L . If d and L have comparable values, the sound pressure from an equivalent source measured on its closest control points and on its neighbour's closest control points will be similar. On the contrary, if the ratio d/L takes a small value, the sound pressures on the source's and its neighbour's points will be well separated in time and amplitude. To investigate this, the global error $\bar{\epsilon}$ measured in the 15 simulations performed was plotted as a function of d/L . The results are shown in Fig.

5 with one plot for each value of κ . In this section the focus is put on the onset of instability, that is the points where the error curves show a sudden change. It can be seen that instability arises at similar values of d/L for the different simulation setups. The lowest value leading to instabilities was found to be $d/L = 0.37$. Thus, it is estimated that the Equivalent Source Method should produce stable simulations as long as $d/L < 1/3$. It can be expressed in terms of directly controllable parameters as

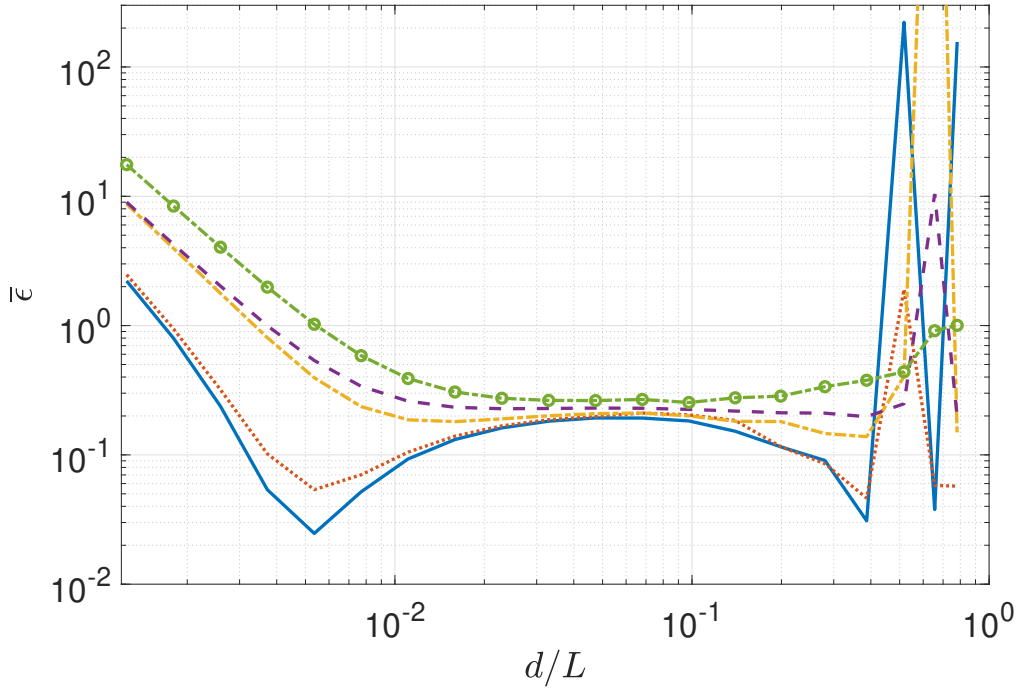
$$\frac{d}{\sqrt{d^2 + h_s^2}} < \frac{1}{3}. \quad (40)$$



(a) $\kappa = 2$.



(b) $\kappa = 4$.



(c) $\kappa = 8$.

Figure 5: Error measured in the ESM simulations. Solid blue line: $h_p = 53.6$ mm; Dotted red line: $h_p = 85.8$ mm; Dash-dotted yellow line: $h_p = 143$ mm; Dashed purple line: $h_p = 214$ mm; Circled green line: $h_p = 274$ mm.

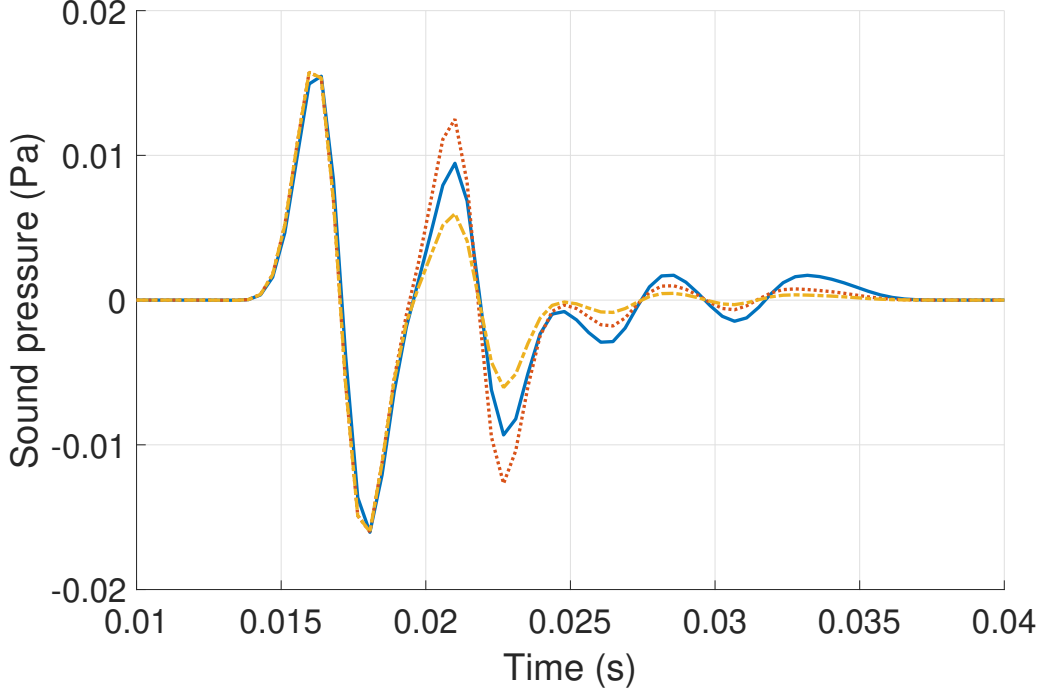


Figure 6: Sound pressure at a receiver point located at $(x, y, z) = (0.65 \text{ m}, 1.05 \text{ m}, -0.50 \text{ m})$ for $h_p = 143 \text{ mm}$ and $\kappa = 4$. Solid blue line: reference sound pressure; Dotted red line: ESM with $d/L = 0.022$; Dash-dotted yellow line: ESM with $d/L = 0.066$.

3.3. Accuracy of the results

As seen in Fig. 5b and Fig. 5c, the error $\bar{\epsilon}$ as a function of d/L can have two local minima. The sound pressure found in simulations on either side of the first local minimum with $h_p = 143 \text{ mm}$ and $\kappa = 4$ is shown in Fig. 6 for a receiver located at $(x, y, z) = (0.65 \text{ m}, 1.05 \text{ m}, -0.50 \text{ m})$. The results indicate that the Equivalent Source Method tends to overestimate the amplitude of the specular reflection for low values of d/L . The sound pressure amplitude then decreases when d/L increases, and the specular reflection is eventually underestimated until instability arises. This agrees with the expected influence of the scalar product described in section 2.4. The first local minimum then corresponds to the pivot point between overestimate and underestimate. However, the diffraction effect which are seen with an onset at 0.023 s are underestimated in both the curves presented. This shows that the accuracies of the specular reflection and of the diffraction effect depend on different parameters. Nevertheless, the global error appears to be dominated by the specular error. This error should therefore be minimized as the first priority.

It is desirable to know which parameter values can lead to the first local minimum as it is less likely to be affected by instability issues. Moreover, $\bar{\epsilon}$ exhibited little variation with respect to h_p as long as κ was kept constant. Consequently, the ratio $(d/L)_0$ yielding the first local minimum has been recorded together with the value $\bar{\epsilon}_0$ of the error at this point. This was done for 12 of the 15 simulations, as three cases with $\kappa = 8$ exhibited too large of an error to have a meaningful minimum. This can be explained by their large values of h_s , where equivalent sources are indeed more than 1 m apart from each other. It can be observed from Fig. 5 that the value of $(d/L)_0$ is roughly divided by 8 when κ is doubled. It suggests a relation $(d/L)_0 \propto \kappa^{-3}$, and applying regression analysis to the data with this assumption finds

$$(d/L)_0 = 3\kappa^{-3} \quad (41)$$

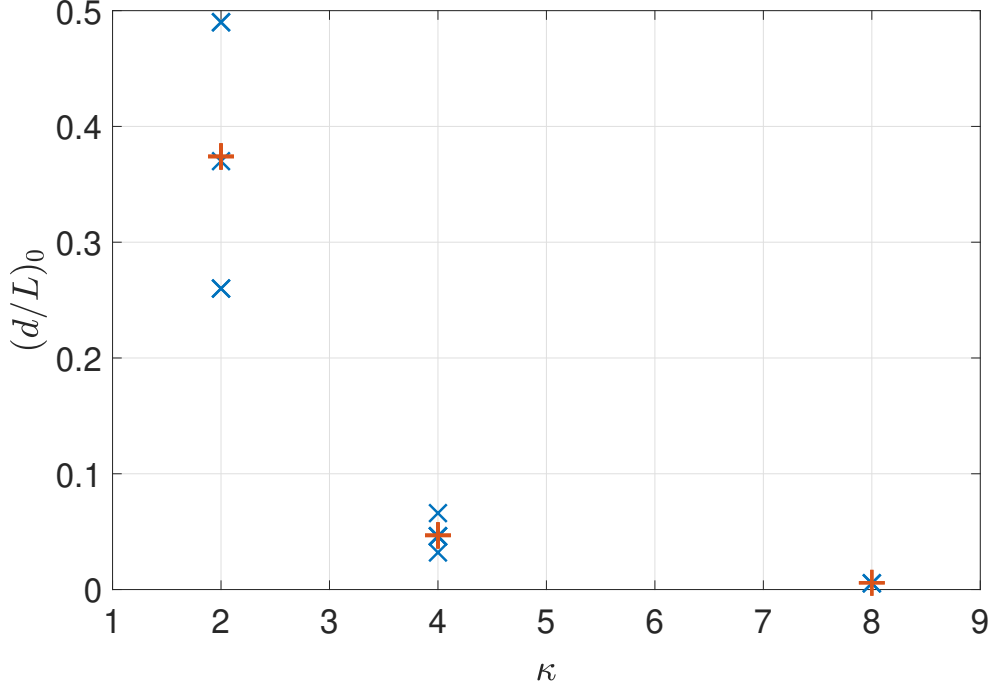


Figure 7: Parameter relation leading to highest accuracy in ESM simulations. Blue crosses: data from simulations; Red plus signs: regression from Eq. (41).

with an R^2 value of 0.86. The data and regression can be seen in Fig. 7. Rewriting Eq. (41) with directly controllable parameters gives

$$\frac{d_0}{\sqrt{d_0^2 + h_s^2}} = 3\kappa^{-3}. \quad (42)$$

In cases where $\kappa = 2$ Eq. (42) returns $d_0/\sqrt{d_0^2 + h_s^2} = 0.375$, a value slightly above the stability limit estimated in Eq. (40). Although the estimate is not a strict limit and local minima could still be found, it does indicate that simulations with $\kappa = 2$ have a high risk of being unstable if Eq. (42) is followed.

The data points $\bar{\epsilon}_0$ collected suggest that the minimal error depends on the spacing between equivalent sources h_s . This is a sensible result, as the density of sources impacts directly how well a wavefront can be reproduced. The relationship between these two quantities is plotted in Fig. 8. It is observed that the minimal error takes lowest values for $h_s < 0.5$ m, reaching a limit at $\bar{\epsilon}_0 = 2.5\%$. As discussed previously, the global error is dominated by the error on the specular reflection. Consequently, the minimal error $\bar{\epsilon}_0$ corresponds to the lowest specular error. It follows therefrom that the limit $\bar{\epsilon}_0 = 2.5\%$ represents the remaining diffraction error. When $h_s > 0.5$ m, the minimal error increases together with the spacing between equivalent sources. It is known that accuracy is linked to the number of sources per wavelength of the signal to be reproduced [22]. The present threshold corresponds to 1.6 equivalent sources per wavelength at the higher limit of the half-power bandwidth of the input signal. It can then be recommended for maximal accuracy to implement at least 2 equivalent sources per wavelength at the highest frequency desired.

When performing an acoustic simulation, the geometry parameters need to be fixed prior to the calculations. In the Equivalent Source Method, this concerns d and two of the three interdependent quantities h_p , h_s and κ . It has been shown that the spacing of the control points h_p influences neither the stability nor the accuracy of the simulation. It can therefore be left aside and determined by the values given to h_s and

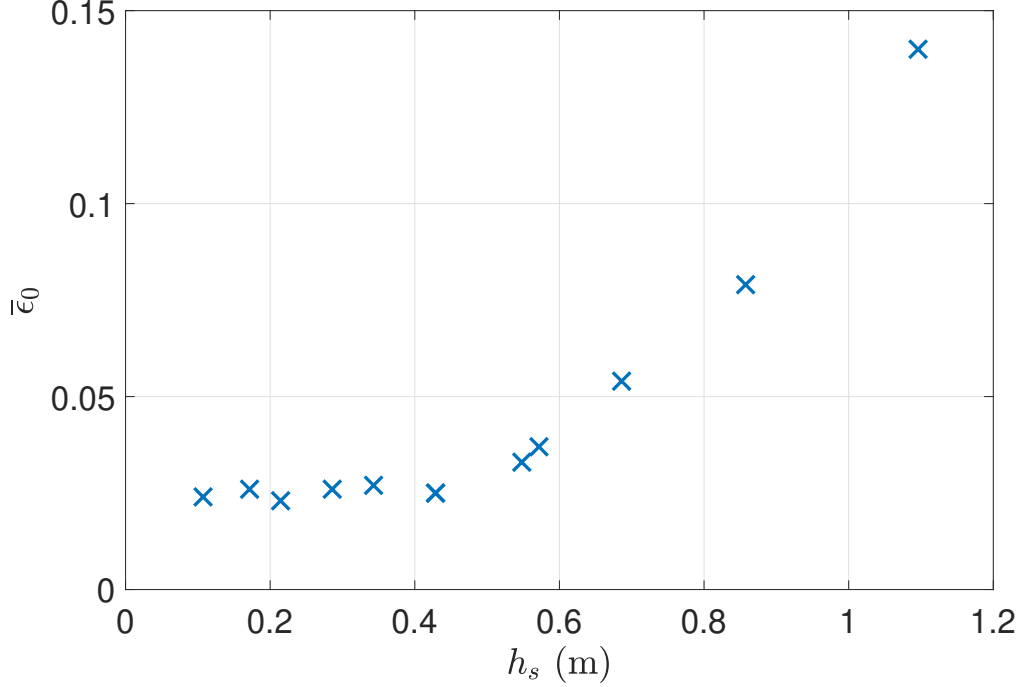


Figure 8: Relation between minimal error $\bar{\epsilon}_0$ and spacing of equivalent sources h_s .

κ . The spacing between equivalent sources h_s , however, determines the accuracy of the simulation. From the results presented its value should be set to respect 2 sources per wavelength at the highest frequency simulated. Although κ was not found to affect accuracy, it influences both the stability and the computation time of the simulation. For a given h_s , κ determines the spacing of control points. Therefore, it determines the number of control points in the simulation, and hence the number of equations in the system to be solved. For computation efficiency it is then desired to keep κ as low as possible. It was seen, however, that $\kappa = 2$ leads to a high risk of instability. Thus, it is recommended to set $\kappa = 4$. Finally, with h_s and κ fixed, the orthogonal distance d between the equivalent sources and the surface can be found according to Eq. (42) for best accuracy.

3.4. Effect of higher order time interpolation

The previous results were obtained by applying linear time interpolation to the boundary equation. It is however possible to use a higher order interpolation in an attempt to reach higher accuracy. This is verified here with quadratic time interpolation. The errors obtained from linear and quadratic interpolations are compared in Fig. 9 with the geometric parameters $h_p = 85.8$ mm and $\kappa = 4$. It is seen that the errors for the two interpolation cases are very similar for $d/L < 0.2$. The quadratic interpolation simulation however becomes unstable past this value, whereas the linear case remains stable until $d/L = 0.5$. Furthermore, the computation time with quadratic interpolation is about 50% larger due to an extra history term involved on the right-hand side of the equation. Hence, it is found that there is nothing to be gained from using higher order time interpolation in the Equivalent Source Method.

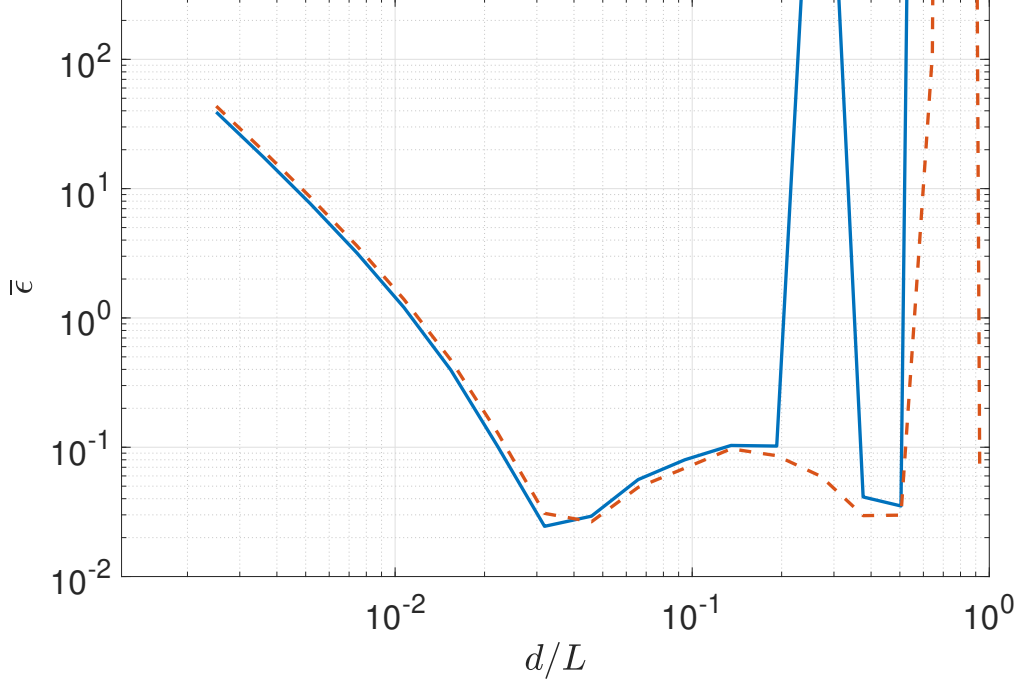


Figure 9: Error measured in the ESM simulations with $h_p = 85.8$ mm and $\kappa = 4$. Solid blue line: quadratic interpolation; Dashed red line: linear interpolation.

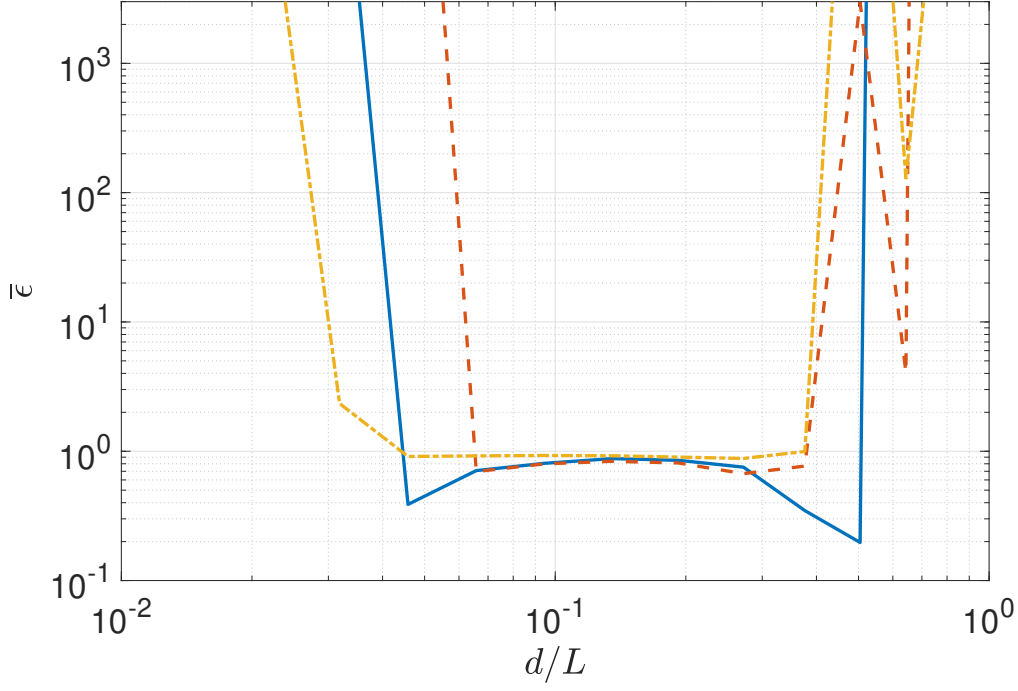
4. Solving an interior problem

The Equivalent Source Method in the time domain is now to be applied to an interior problem. The goal is to investigate whether the previous findings on stability and accuracy hold in such a situation. The simulation test case is a rectangular box with dimensions (6 m, 5 m, 2 m) centered on the origin. The source is located at $(-1 \text{ m}, 0 \text{ m}, -0.5 \text{ m})$ and the receivers are defined on a horizontal grid at $z = 0.5 \text{ m}$ with a spacing of 0.1 m covering the whole area. The impulse response is calculated until $t = 0.1 \text{ s}$. Two boundary conditions are considered: rigid walls and constant impedance. In the latter case, the surface impedance is set to $Z_a = 3\rho c$ uniformly over all surfaces; it is thus real-valued, frequency-independent and angle-independent. In the Image Source Method used as reference, the reflection coefficient is either set to $R = 1$ or $R = 0.5$, which respectively correspond to infinite surface impedance and $Z_a = 3\rho c$ when assuming normal incidence and surface dimensions much larger than the wavelength. The reflection coefficient $R = 0.5$ is approximated to be constant over all incidence angles, the reference simulation from the Image Source Method is therefore not an exact solution. However, given the conditions of the test case, it is estimated that this approximation does not critically affect the results [19]. Error plots are created again from the simulations for $\kappa = 4$ and $h_p = (85.8 \text{ mm}, 143 \text{ mm}, 214 \text{ mm})$, and they are shown in Fig. 10. The simulations performed with the two boundary conditions considered exhibit similar behaviours. It can be seen that the stability condition in Eq. (40) still has to be respected for an interior problem. The simulations are indeed stable up to $d/L = 0.50$ for $h_p = 85.8 \text{ mm}$ and $d/L = 0.38$ for $h_p = (143 \text{ mm}, 214 \text{ mm})$. However, a new instability arises for low ratios d/L . The onset of this instability corresponds to the value in Eq. (41) that lead to highest accuracy for the single-plane reflection. As already mentioned, this value corresponds to the pivot point between overestimating and underestimating the amplitude of the sound field. Consequently, when $d/L < 3\kappa^{-3}$, the sound pressure amplitude on the control points coming from the equivalent sources is

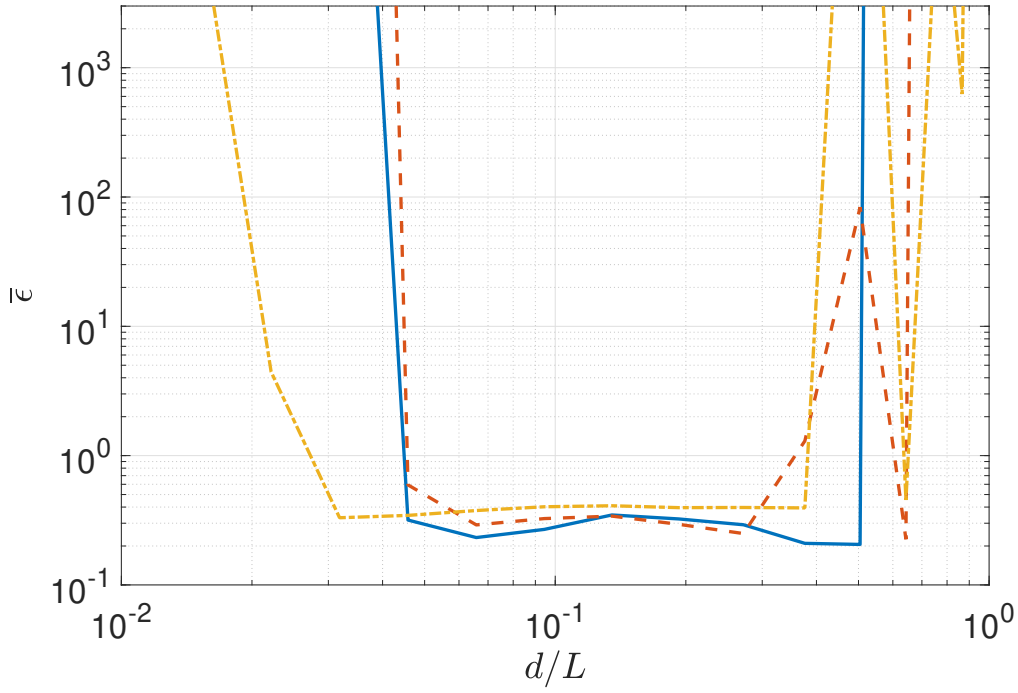
larger than should be. In return, the equivalent sources' reactions to this sound pressure are overestimated again. This process occurs at every new reflection and builds up to create the instability. Therefore, the stability condition of the Equivalent Source Method for an interior problem is approximately

$$3\kappa^{-3} < \frac{d}{L} < \frac{1}{3}. \quad (43)$$

It is also seen that simulations are more accurate when d/L approaches the instability thresholds. Nevertheless, even in the stability region, the error is found to be high with $\bar{\epsilon}$ between 70% and 90% for rigid walls and between 20% and 40% for the impedance boundary condition. An example of the sound pressure at one receiver located at $(x, y, z) = (0.65 \text{ m}, -1.45 \text{ m}, 0.50 \text{ m})$ for $h_p = 143 \text{ mm}$ and $d/L = 0.094$ is given in Fig. 11. It is observed that the sound pressure calculated with the Equivalent Source Method is largely attenuated compared to the reference with both boundary conditions. This is due to the fact that the stability region corresponds to values of d/L when the specular reflection amplitude is underestimated. Similarly to the overestimation leading to instability, the underestimation is amplified at every reflection and results in numerical damping. Because some damping is already present in the model when the surface impedance is finite, numerical damping is less important in the case where $Z_a = 3\rho c$ than with rigid walls.

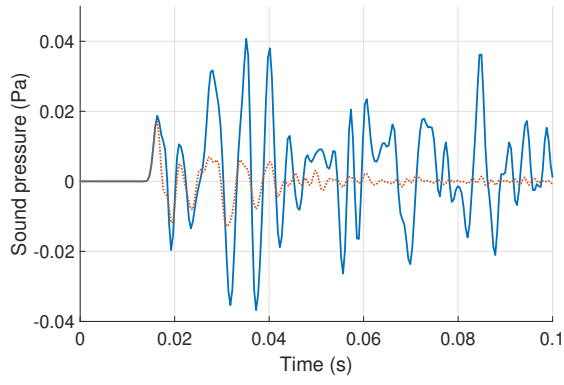


(a) Rigid walls.

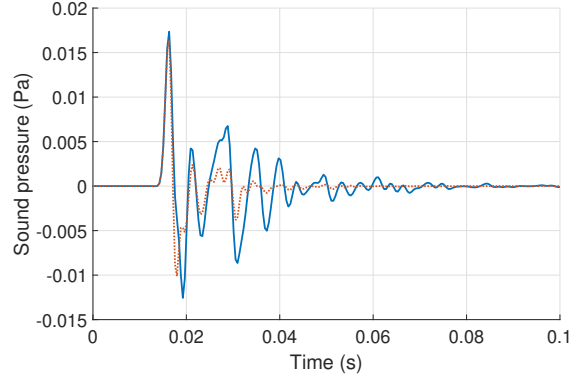


(b) Constant impedance.

Figure 10: Error measured in the ESM simulations.¹⁸ Solid blue line: $h_p = 85.8$ mm; Dashed red line: $h_p = 143$ mm; Dash-dotted yellow line: $h_p = 214$ mm.



(a) Rigid walls.



(b) Constant impedance.

Figure 11: Sound pressure at a receiver point located at $(x, y, z) = (0.65 \text{ m}, -1.45 \text{ m}, 0.50 \text{ m})$ for $h_p = 143 \text{ mm}$ and $d/L = 0.094$. Solid blue line: reference sound pressure; Dotted red line: Equivalent Source Method.

5. Discussion

In their study [12], Lee, Brentner and Morris tackled instability by truncating singular values in the matrix inversion operation. Such a procedure can lead to inaccuracies due to energy loss, which was addressed with a time-averaging scheme as a complement strategy. In the present study, the understanding of the mechanism leading to instability is furthered, allowing to ensure a stable simulation from the geometric setup stage. From two-dimensional scattering problems, they also suggested guidelines for result accuracy. They notably suggested that the number of equivalent sources should be a quarter of the number of control points. This is in agreement with the recommendation $\kappa = 4$ given in the present work from a three-dimensional problem, which corresponds to 16 control points per equivalent source. Another suggestion they made was to position equivalent sources on an 80% scale of the scattering object. This differs from the results found in this paper, where the orthogonal distance d between the equivalent sources and the surface is recommended to be set according to the spacing between sources h_s and the spacing ratio κ between control points and equivalent sources.

The study presented here is limited in a few aspects. Firstly, only flat surfaces have been considered. Although curved surfaces can be discretized into flat pieces, the difference in geometry could have an influence on how equivalent sources interact. Secondly, the equivalent sources were always centered between four control points in the simulations performed. The results obtained are expected to be different in other conditions, especially if sources are positioned in the center of nine control points. Investigation on the influences of the input signal and the sampling frequency were also overlooked by the focus of the study on geometric parameters. Finally, the error associated to the modelling of the diffraction effect has not been separated from the error on specular reflection. Additional guidelines for the accuracy of simulations could potentially be found by investigating the diffraction effect in more details.

Furthermore, computation efficiency has not been thoroughly investigated. The Equivalent Source Method has the advantage that only boundaries need to be discretized. Therefore, the computational load grows with the surface area of the domain and not its volume. Another advantage of the Equivalent Source Method in the time domain is that only one matrix inversion needs to be performed to solve the problem. The calculation occurring for a new time step then consists of a matrix multiplication. As a consequence, the computational load grows linearly with the length of the impulse response. In addition the matrix to be inverted is even sparse, making the inversion operation easy to handle. The construction of this matrix can nonetheless generate a significant number of lines containing only zeros when $\kappa > 2$. These unnecessary equations significantly increase the size of the system, which affects all the calculations. An important efficiency gain can thus be found.

Lastly, the numerical damping occurring with interior problems remains an unsolved issue. If the amount of underestimation for a single reflection can be predicted, numerical damping could then be compensated by correcting the source strengths when solving the system of equations at each time step. Another approach would be to combine equivalent sources with another simulation method. The second method could account for the main part of the sound field with specular reflections while the equivalent sources solve the remaining part with diffraction effects notably. The impact of numerical damping would thus be limited by the small amount of energy contained in the contributions from equivalent sources.

6. Conclusion

The present paper provides a better understanding of the Equivalent Source Method in the time domain. The formulation of the problem has been given for rigid and impedance boundary conditions, as well as for any time interpolation order. It has been showed that instability in simulations arises when the equivalent sources have too much influence on each other. This can be avoided by placing the sources close enough to the boundary, thus ensuring a stable simulation before calculations are performed. It was also observed that a higher time interpolation order does not improve accuracy and makes stability conditions stricter. Linear time interpolation is therefore sufficient for the method. Moreover, it has been found from the study of single-plane reflection that the Equivalent Source Method can overestimate or underestimate the reflected sound pressure depending on the geometric parameters. Following this, guidelines have been established to

setup simulations yielding accurate results. These findings have been further tested with an interior problem consisting of a rectangular box. It was observed that the overestimation and underestimation phenomena occurring for a single plate are replicated at every reflection on the domain boundary. As a result, the errors propagate in the simulation and lead to either instability or large numerical damping. A solution to the numerical damping would therefore be required in order to apply the Equivalent Source Method to room acoustics.

7. Appendix: General order time interpolation

Given an arbitrary function f evaluated on discrete steps x_j , Lagrange polynomials can be employed in order to interpolate its values [23]. The interpolation of f on the interval $\{x \in \mathbb{R} \mid x_0 \leq x \leq x_k\}$ is

$$L(x) = \sum_{j=0}^k f(x_j) l_j(x). \quad (44)$$

k is the order of the polynomial interpolation, and the Lagrange basis polynomials $l_j(x)$ are defined as

$$l_j(x) = \prod_{\substack{m=0 \\ m \neq j}}^k \frac{x - x_m}{x_j - x_m}. \quad (45)$$

In the case $k = 1$ this is equivalent to linear interpolation. The derivative of f can also be obtained by deriving the interpolated function $L(x)$:

$$\frac{\partial L}{\partial x}(x) = \sum_{j=0}^k f(x_j) \frac{\partial l_j}{\partial x}(x); \quad (46)$$

$$\frac{\partial l_j}{\partial x}(x) = l_j(x) \sum_{\substack{m=0 \\ m \neq j}}^k \frac{1}{x - x_m}. \quad (47)$$

Lagrange polynomial interpolation is applied to the equivalent source strength q_e by setting $x = (n - \nu_{be})\Delta t$ and $x_j = n_{be}^j \Delta t$, with n_{be}^j integer numbers. Moreover, in the present case it is considered that $n_{be}^{k-1} \leq n - \nu_{be} \leq n_{be}^k$. It is then possible to write

$$q_e((n - \nu_{be})\Delta t) = \sum_{j=0}^k q_e(n_{be}^j \Delta t) l_j((n - \nu_{be})\Delta t); \quad (48)$$

$$l_j((n - \nu_{be})\Delta t) = \prod_{\substack{m=0 \\ m \neq j}}^k \frac{(n - \nu_{be})\Delta t - n_{be}^m \Delta t}{n_{be}^j \Delta t - n_{be}^m \Delta t}. \quad (49)$$

As for the time derivative of the source strength:

$$\frac{\partial q_e}{\partial t}((n - \nu_{be})\Delta t) = \sum_{j=0}^k q_e(n_{be}^j \Delta t) \frac{\partial l_j}{\partial t}((n - \nu_{be})\Delta t); \quad (50)$$

$$\frac{\partial l_j}{\partial t}((n - \nu_{be})\Delta t) = l_j((n - \nu_{be})\Delta t) \sum_{\substack{m=0 \\ m \neq j}}^k \frac{1}{(n - \nu_{be})\Delta t - n_{be}^m \Delta t}. \quad (51)$$

The discrete time steps n_{be}^j around $n - \nu_{be}$ can be related to the current time step n by introducing their corresponding travel times: $n_{be}^j = n - \nu_{be}^j$, with ν_{be}^j integer numbers. It follows that $\nu_{be}^k \leq \nu_{be} \leq \nu_{be}^{k-1} \leq \dots \leq \nu_{be}^0$. This is illustrated in Fig. 12. Replacing the terms in Eq. (49) and (51) then produces

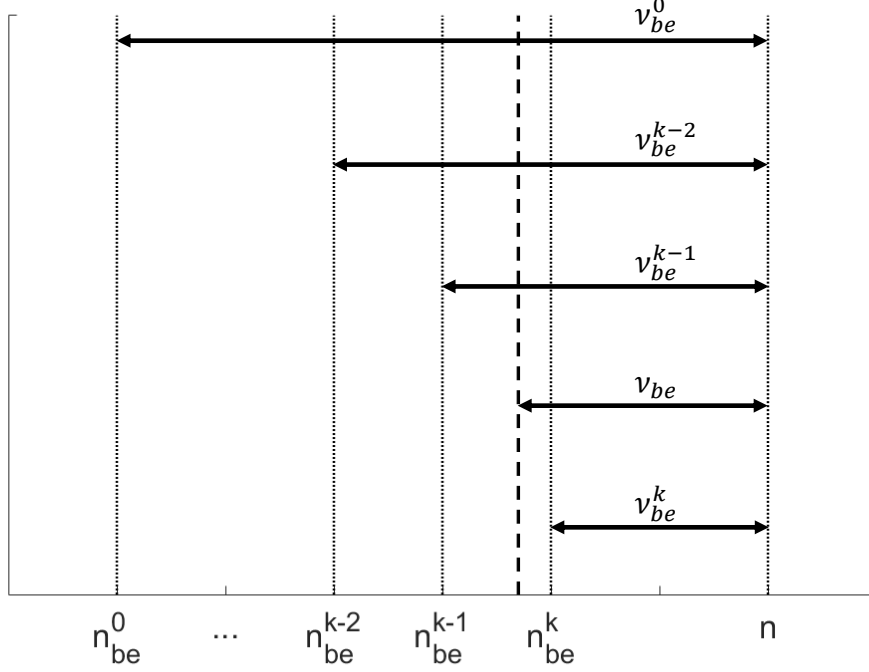


Figure 12: Time steps and travel times used in the Lagrange interpolation.

$$l_j((n - \nu_{be})\Delta t) = \prod_{\substack{m=0 \\ m \neq j}}^k \frac{\nu_{be}^m - \nu_{be}}{\nu_{be}^m - \nu_{be}^j}; \quad (52)$$

$$\frac{\partial l_j}{\partial t}((n - \nu_{be})\Delta t) = l_j((n - \nu_{be})\Delta t) \sum_{\substack{m=0 \\ m \neq j}}^k \frac{1}{(\nu_{be}^m - \nu_{be})\Delta t}. \quad (53)$$

It can be seen that the Lagrange basis polynomials only depend on the travel time ν_{be} from source e to point b , and not on the current time step n . The notation is then simplified to $l_j(\nu_{be})$ and $\frac{\partial l_j}{\partial t}(\nu_{be})$. From Eq. (48) and (50), the terms corresponding to the most advanced time step $n_{be}^k \Delta t$ can be isolated, resulting in

$$q_e((n - \nu_{be})\Delta t) = q_e(n_{be}^k \Delta t) l_k(\nu_{be}) + \sum_{j=0}^{k-1} q_e(n_{be}^j \Delta t) l_j(\nu_{be}); \quad (54)$$

$$\frac{\partial q_e}{\partial t}((n - \nu_{be})\Delta t) = q_e(n_{be}^k \Delta t) \frac{\partial l_k}{\partial t}(\nu_{be}) + \sum_{j=0}^{k-1} q_e(n_{be}^j \Delta t) \frac{\partial l_j}{\partial t}(\nu_{be}). \quad (55)$$

Lastly, Eq. (7) is rewritten with the expressions from Eq. (54) and (55):

$$\begin{aligned} \nabla p_{be}(n\Delta t) = \frac{1}{4\pi} \left(- \left(\frac{l_k(\nu_{be})}{r_{be}^2} + \frac{1}{cr_{be}} \frac{\partial l_k}{\partial t}(\nu_{be}) \right) q_e(n_{be}^k \Delta t) \right. \\ \left. - \sum_{j=0}^{k-1} \left(\frac{l_j(\nu_{be})}{r_{be}^2} + \frac{1}{cr_{be}} \frac{\partial l_j}{\partial t}(\nu_{be}) \right) q_e(n_{be}^j \Delta t) \right) \mathbf{u}_{be}. \end{aligned} \quad (56)$$

This equation can then be used instead of Eq. (15) to derive the matrix form of the problem.

References

- [1] I. Bork, Report on the 3rd round robin on room acoustical computer simulation – part ii: calculations, *Acta Acust.* United Ac. 91 (4) (2005) 753–763.
- [2] G. Marbjerg, J. Brunskog, C.-H. Jeong, The difficulties of simulating the acoustics of an empty rectangular room with an absorbing ceiling, *Appl. Acoust.* 141 (2018) 35–45.
- [3] N. Atalla, F. Sgard, *Finite element and boundary methods in structural acoustics and vibration*, CRC Press, Boca Raton, United States of America, 2017.
- [4] T. W. Wu, *Boundary element acoustics: Fundamentals and computer codes*, WIT Press, Southampton, United Kingdom, 2000.
- [5] R. J. LeVeque, *Finite difference methods for ordinary and partial differential equations: Steady-state and time-dependent problems*, SIAM, Philadelphia, United States of America, 2007.
- [6] M. Ochmann, The source simulation technique for acoustics radiation problems, *Acustica* 81 (6) (1995) 512–527.
- [7] M. E. Johnson, S. J. Elliott, K. H. Baek, J. G. Bonito, An equivalent source technique for calculating the sound field inside an enclosure containing scattering objects, *J. Acoust. Soc. Am.* 104 (3) (1998) 1221–1231.
- [8] M. Hornikx, J. Forssén, The 2.5-dimensional equivalent sources method for directly exposed and shielded urban canyons, *J. Acoust. Soc. Am.* 122 (5) (2007) 2532–2541.
- [9] R. Mehra, N. Raghunvanshi, L. Antani, A. Chandak, S. Curtis, D. Manocha, Wave-based sound propagation in large open scenes using an equivalent source formulation, *ACM Trans. Graph.* 32 (2) (2013) 1–13.
- [10] W. Kropp, P. U. Svensson, Application of the time domain formulation of the method of equivalent sources to radiation and scattering problems, *Acustica* 81 (1995) 528–543.
- [11] S. Lee, K. S. Brentner, P. J. Morris, Acoustic scattering in the time domain using an equivalent source method, *AIAA J.* 48 (12) (2010) 2772–2780.
- [12] S. Lee, K. S. Brentner, P. J. Morris, Assessment of time-domain equivalent source method for acoustic scattering, *AIAA J.* 49 (9) (2011) 1897–1906.
- [13] S. Lee, Review: The use of equivalent source method in computational acoustics, *J. Comput. Acoust.* 25 (1) (2017) 1630001 (19 pages).
- [14] D. G. Duffy, *Green’s functions with applications*, 1st Edition, CRC Press, Boca Raton, United States of America, 2001, Ch. 3.
- [15] R. N. Bracewell, *The Fourier transform and its applications*, 3rd Edition, McGraw-Hill, Singapore, 2000, Ch. 6, pp. 124–127.
- [16] U. P. Svensson, P. T. Calamia, S. Nakanishi, Frequency-domain edge diffraction for finite and infinite edges, *Acta Acust.* United Ac. 95 (3) (2009) 568–572.
- [17] U. P. Svensson, A. Asheim, Time-domain formulation of an edge source integral equation, *Proc. Mtgs. Acoust.* 19 (2013) 015103 (9 pages).
- [18] M. A. Biot, I. Tolstoy, Formulation of wave propagation in infinite media by normal coordinates with an application to diffraction, *J. Acoust. Soc. Am.* 29 (3) (1957) 381–391.
- [19] J. B. Allen, D. A. Berkley, Image method for efficiently simulating small-room acoustics, *Commun. Numer. Meth. Engng.* 65 (4) (1979) 943–950.
- [20] J. Borish, Extension of the image model to arbitrary polyhedra, *J. Acoust. Soc. Am.* 75 (6) (1984) 1827–1836.
- [21] S. Sorokin, S. T. Christensen, Low-frequency breakdown of boundary element formulation for closed cavities in excitation conditions with a ‘breathing’-type component, *Commun. Numer. Meth. Engng.* 16 (2000) 325–334.
- [22] S. Marburg, Six boundary elements per wavelength: Is that enough?, *J. Comp. Acoust.* 10 (1) (2002) 25–51.
- [23] H. Jeffreys, B. Jeffreys, *Methods of mathematical physics*, 3rd Edition, Cambridge University Press, Cambridge, United Kingdom, 1956, Ch. 9, p. 261.

APPENDIX D

A combination of image
and equivalent sources:
Developments on
“Parametric study of the
Equivalent Source Method
and interior domain
calculations”

A combination of image and equivalent sources: Developments on "Parametric study of the Equivalent Source Method and interior domain calculations"

Boris Mondet^{a,b,*}, Jonas Brunskog^b, Cheol-Ho Jeong^b, Claus Lyng Christensen^a, Jens Holger Rindel^a

^a*Odeon A/S, DTU Science Park, Denmark*

^b*Acoustic Technology, DTU Electrical Engineering, Technical University of Denmark, Denmark*

Keywords: Equivalent Source Method, Image sources, Time domain, Interior problem

1. Introduction

In a recent article [1], the present authors together with Svensson have presented an application of the Equivalent Source Method (ESM) in the time domain to interior problems. The stability region for the geometric parameters has notably been determined, but several issues that have been left unresolved are addressed here. Firstly, many unnecessary equations were included in the system of equations describing the problem, making the computation inefficient. This can be solved by an alternative discretization of the boundary with control points. Secondly, simulation results were hindered by numerical damping. In the present study, image sources are introduced in addition to the equivalent sources in an attempt to improve accuracy.

2. Alternative surface discretization for the Equivalent Source Method

Both equivalent sources and control points were distributed uniformly in [1] to discretize the surfaces in the domain. Their respective spacings are noted h_s and h_p , with the ratio $\kappa = h_s/h_p$. The equivalent sources were positioned to always be centrally located between four control points, thus binding the value of κ to a power of 2. Furthermore, the study recommends to set $\kappa = 4$ for simulations, leading to 16 control points per equivalent source as shown in Fig. 1a. Each control point in the simulation corresponds to one equation in the system to be solved. However, the control points that are not reached by any equivalent source within the shortest time interval yield lines containing only zeros in the matrix A_0 describing the system [1].

In order to avoid these unnecessary equations and reduce the size of the system, a non-uniform distribution of control points is introduced. For each equivalent source, a square of 4 control points is defined with side h_p and centered on the orthogonal projection of the source on the surface, as illustrated in Fig. 1b. An analogy can be seen with nonconforming linear elements in the Boundary Element Method [2]. This distribution can guarantee that every line of the matrix A_0 contains exactly one non-zero element. The ratio κ can also take any value desired while maintaining equivalent sources centrally located between control points, unlike the uniform distribution case. The results obtained with this alternative discretization are compared to those from [1] for the single reflection on a finite rigid plate. The error plots from both discretization techniques for $h_s = 343$ mm and $\kappa = 4$ are shown in Fig. 2. For the homogeneous discretization 12 control points were reached within the shortest time interval by each source, meaning that 1/4 of the lines in A_0 contained only zeros. The two error plots are seen to be highly similar, with the same tendencies

*Corresponding author

Email address: bojmo@elektro.dtu.dk (Boris Mondet)

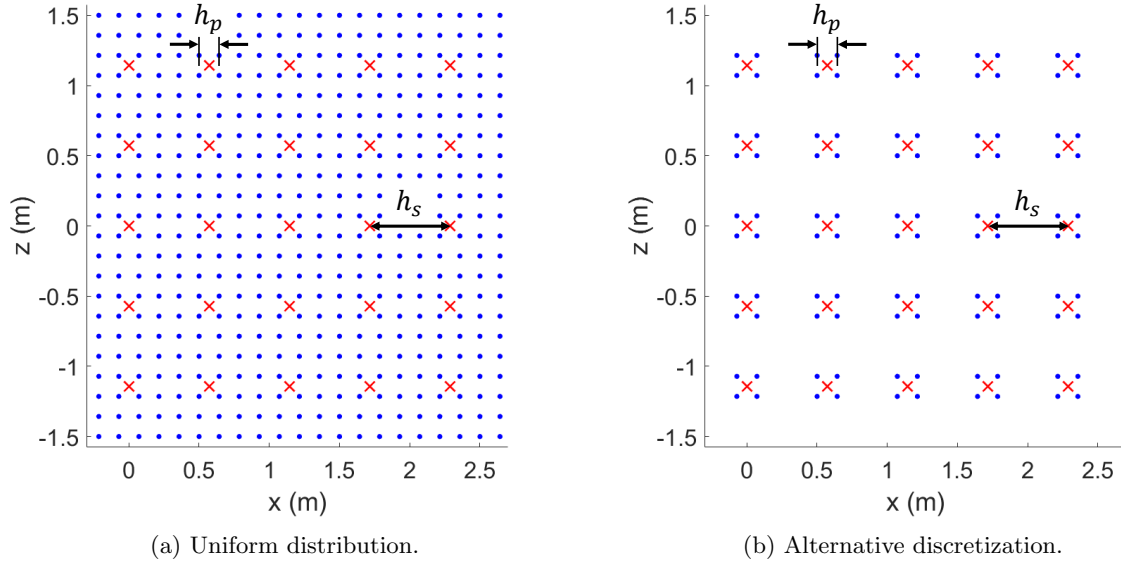


Figure 1: Close-up front view of the discretization of a surface. Blue dots: control points; Red crosses: equivalent sources.

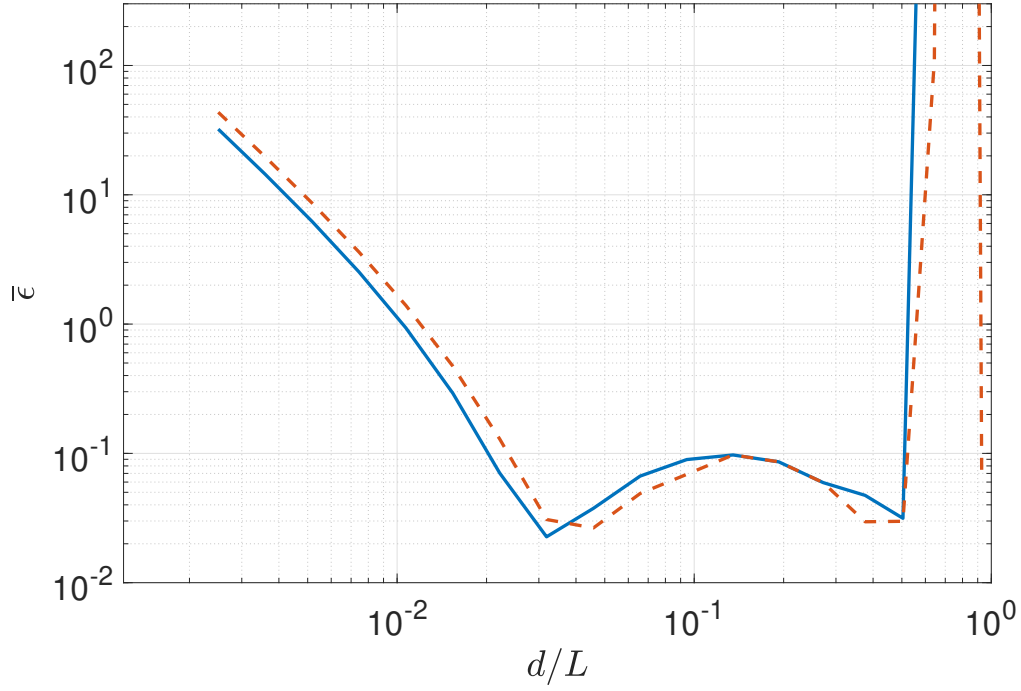


Figure 2: Error measured in the ESM simulations with $h_s = 343$ mm and $\kappa = 4$. Dashed red line: results from [1]; Solid blue line: alternative discretization.

regarding stability and accuracy. In terms of efficiency, the alternative discretization is found to save 45% of computation time for this test case. The distribution of control points described in the present paper thus appears to give a large gain of computation time without altering the accuracy of the simulations.

3. The Image-Equivalent Source Method

3.1. Theory

Image sources are very efficient to model early specular reflections [3, 4]. The main drawbacks of the Image Source Method are the lack of diffraction and the computational load that increases exponentially with the duration of the calculated impulse response. On the other hand, the Equivalent Source Method does not suffer from the duration of the response as computational load only grows linearly. However, the accuracy of the results for interior problems is hindered by numerical damping [1]. By incorporating low-order image sources in the equivalent source algorithm, the early part of the time response where most of the acoustic energy is present can be simulated accurately, while the late part and the diffraction effects are modelled with equivalent sources. Hence, the drawbacks aforementioned for both methods are mitigated.

Combining image and equivalent sources in one method is a rather easy process. The largest part of the algorithm remains identical to the Equivalent Source Method, and only the construction of the incident sound field is altered. In addition to the original sound source, image sources up to an arbitrary order are positioned in the domain. The incident sound pressure $p_i(t)$ then becomes the sum of the contributions from the original source and from the M image sources

$$p_i(t) = \sum_{m=0}^M p_m(t). \quad (1)$$

The strengths of the equivalent sources are then calculated from the boundary condition equation without any further change in the derivation of the system. The sound pressure equation for a boundary with finite impedance is

$$\frac{1}{\rho} \nabla p_r(t) \cdot \boldsymbol{\eta}_n + \frac{\partial p_r(t)}{\partial t} * y_a(t) = -\frac{1}{\rho} \nabla p_i(t) \cdot \boldsymbol{\eta}_n - \frac{\partial p_i(t)}{\partial t} * y_a(t), \quad (2)$$

with $p_r(t)$ the reflected sound pressure, $y_a(t)$ the surface admittance in the time domain, and $\boldsymbol{\eta}_n$ the normal unit vector to the surface. The rigid boundary condition can be obtained by setting $y_a(t) = 0$. The final matrix formulation of the problem is found in [1].

3.2. Simulation results

The Image-Equivalent Source Method (IESM) is applied to the rectangular box test case with uniform surface impedance $Z_a = 3\rho c$ from [1]. The box has the dimensions (6 m, 5 m, 2 m), and the image sources are set to account for reflections up to 0.01 s after the onset of the original source. The control points are distributed on the surfaces according to the discretization described in section 2. The sound pressure calculated at one receiver position is shown in Fig. 3 and compared with the reference and the results from the Equivalent Source Method. As expected, it is observed that the early reflections are simulated more accurately with the help of image sources in the IESM. After 0.03 s in the response, however, the numerical damping coming from the equivalent sources is seen to take effect as image sources do not contribute to the sound field anymore. The error plot of the Image-Equivalent Source Method is given in Fig. 4 for $\kappa = 4$ and three different values of h_s , with the same error estimate as defined in [1]. In the stable region, the global error of the simulations is comprised between 6% and 10%. It is a significant improvement compared to the error of the ESM ranging between 20% and 40% in the same conditions in [1]. The addition of image sources to the Equivalent Source Method can therefore be seen as an interesting solution to inaccuracy issues.

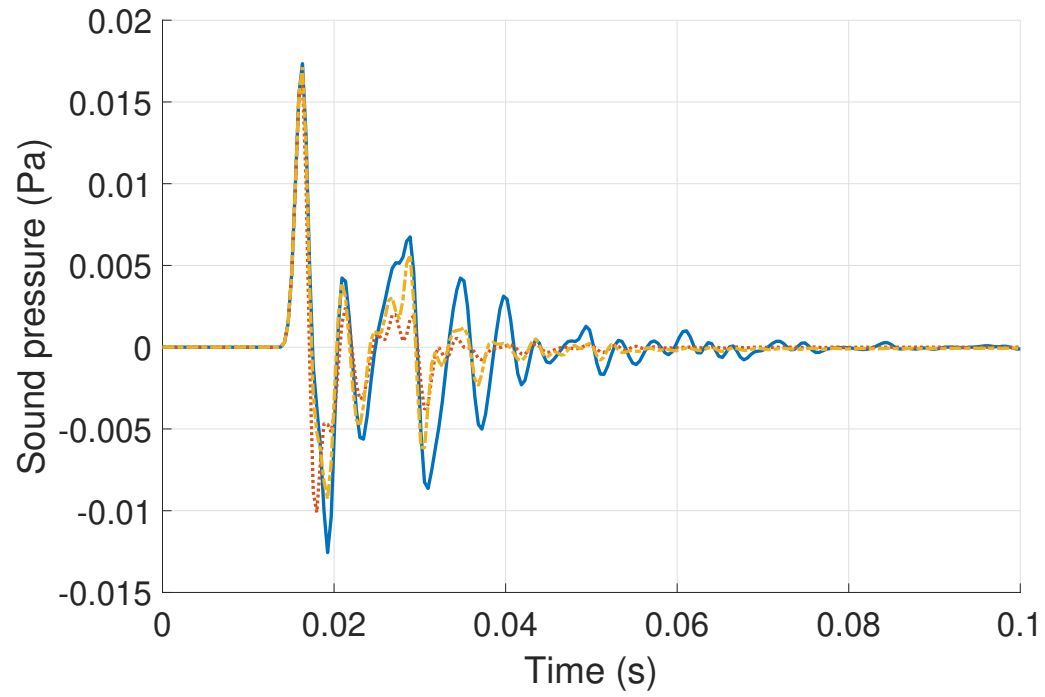


Figure 3: Sound pressure at a receiver point located at $(x, y, z) = (0.65 \text{ m}, -1.45 \text{ m}, 0.50 \text{ m})$ for $h_p = 143 \text{ mm}$ and $d/L = 0.094$. Solid blue line: reference sound pressure from [1]; Dotted red line: Equivalent Source Method from [1]; Dash-dotted yellow line: Image-Equivalent Source Method.

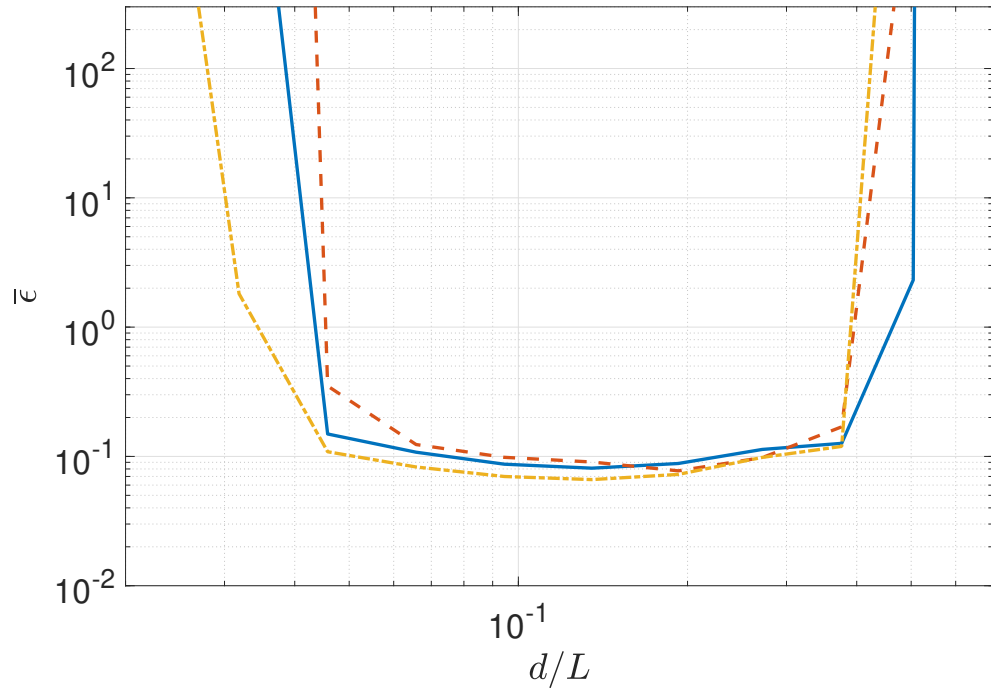


Figure 4: Error measured in the IESM simulations with $\kappa = 4$. Solid blue line: $h_s = 343$ mm; Dashed red line: $h_s = 572$ mm; Dash-dotted yellow line: $h_s = 856$ mm.

4. Discussion and conclusion

A rectangular box has been simulated in this study to allow the comparison with [1]. Yet, it is not an ideal test case to assess the Image-Equivalent Source Method. Diffraction indeed does not occur in such a space. Hence, an important argument for including equivalent sources in the method cannot be verified. Moreover, results from the Image Source Method were taken as reference simulations. Consequently, calculations with the IESM bear the reference solution of the sound field up to the time when equivalent sources take over. The error estimate is therefore biased. The work presented here should then be taken as a proof of concept for the combination of image and equivalent sources, and further validation of the method should be pursued.

The main challenge of the Image-Equivalent Source Method consists in setting the limit for maximum order of image sources. Because a high order leads to better accuracy at the cost of a large computational load, a compromise has to be found for application to room acoustic simulations. A potential solution could be to define a threshold for the energy emitted by a source. Image sources can then be implemented up to the order corresponding to that threshold or up to a predefined maximum order if the threshold is too low to reach within reason, a situation that can occur in the case of two low-absorbing parallel walls.

In addition, computation time of the Equivalent Source Method, and thereby the Image-Equivalent Source Method, can be greatly reduced thanks to a non-uniform distribution of control points on the boundary. It has indeed been found that implementing only four control points per equivalent source for $\kappa > 2$ does not compromise accuracy. When following recommendations from [1], the number of equations in the system is divided by four with this alternative discretization. Such a decrease in the size of the system therefore leads to a large efficiency gain.

References

- [1] B. Mondet, U. P. Svensson, J. Brunskog, C.-H. Jeong, C. L. Christensen, J. H. Rindel, Parametric study of the equivalent source method and interior domain calculations, to be submitted.
- [2] Y. Yasuda, T. Sakuma, Boundary element method, in: T. Sakuma, S. Sakamoto, T. Otsuru (Eds.), Computational simulation in architectural and environmental acoustics: Methods and applications of wave-based computation, Springer, Tokyo, Japan, 2014, Ch. 4, pp. 79–92.
- [3] J. B. Allen, D. A. Berkley, Image method for efficiently simulating small-room acoustics, *J. Acoust. Soc. Am.* 65 (4) (1979) 943–950.
- [4] J. Borish, Extension of the image model to arbitrary polyhedra, *J. Acoust. Soc. Am.* 75 (6) (1984) 1827–1836.

DTU Electrical Engineering
Department of Electrical Engineering
Technical University of Denmark

Ørsted's Plads
Building 348
DK-2800 Kgs. Lyngby
Denmark

Tel: (+45) 45 25 38 00

www.elektro.dtu.dk